Dissertation der
Graduate School of Systemic Neurosciences
der Ludwig-Maximilians-Universität München

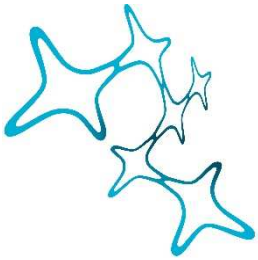

Graduate School of
Systemic Neurosciences
LMU Munich

Structural and functional alterations of cortical neurons in Alzheimer's disease transgenic mice assessed by two-photon *in vivo* imaging

submitted by

Sabine Liebscher

29th November 2016

1st reviewer:

Prof. Dr. Mark Hübener

2nd reviewer:

Prof. Dr. Dr. Christian Haass

Date of defense:

31.01.2017

Contents

Table of Figures

Abbreviations

AAV…….....	Adeno-associated virus
Aβ…….....	Amyloid-β peptide
AD……..……	Alzheimer's disease
AICD…..……	Amyloid intracellular domain
AMPA……	α-amino-3-hydroxy-5-methyl-4-isoxazolepropionic acid
ANOVA…..……	Analysis of variance
AOD…….....	Acousto - optical deflector
AP…….....	Action potential
APH…….……....	Anterior pharynx-defective
APP…….	Amyloid precursor protein
APP-CTF…….....	Amyloid precursor protein C-terminal fragment
APPPS1 or APP/PS1……..	Amyloid precursor protein/Presenilin 1 (used synonymously throughout the text)
AUC…….....	Area under the curve
BACE…….….....	Beta-site APP cleaving enzyme-1, β-secretase
CAA……	Cerebral amyloid angiopathy
CaMKII……...	Calcium/calmodulin-dependent protein kinase II
cAMP…..……	Cyclic Adenosin-Monophosphat
CNS……..……	Central nervous system
cpGFP…….	Circularly permuted green fluorescent protein
CREB…..……	Cyclic AMP response element binding protein
DMSO……	Dimethylsulfoxid
DSI…….	Direction selectivity index
EC_{50}……	Half maximal effective concentration
EDTA…..……	Ethylenediaminetetraacetic acid
ELISA…..……	Enzyme-linked Immunosorbent Assay
EphB2……	Ephrin type B receptor 2
ErbB4…..……	Erb-B2 receptor tyrosine kinase 4
FAD……..……..	Familial Alzheimer's disease
fl-APP..……..	Full length amyloid precursor protein
FRET…...……	Förster/Fluorescence resonance energy transfer
GABA……	Gamma-aminobutyric acid
GECI…..……	Genetically encoded calcium indicator
GFAP…..……	Glial fibrillary acidic protein
GFP……..……...	Green fluorescent protein
GSI……..……	γ-secretase inhibitor
GSK-3β..…….	Glycogen synthase kinase 3-beta
GWAS…….	Genome wide association study
HPLC…..……	High performance liquid chromatography
i.p. ……..……	Intraperitoneal
LGN……..……...	Lateral geniculate nucleus
LTD……..……..	Long-term depression
LTP……..……...	Long-term potentiation
MAPK……	Mitogen-activated protein kinase
MCI……..……	Mild cognitive impairment

NA……..……	Numerical aperture
NCT……..……...	Nicastrin
NMDA……..….....	N-methyl-D-aspartate
OGB-1……..…....	Oregon green bapta-1
OSI……..……..	Orientation selectivity index
PBS……..……..…....	Phosphate buffered saline
Pen-2…..……..	Presenilin enhancer 2
PMT……..…....	Photomultiplier tube
PrP……..……..…...	Prion Protein
PS1……..……..…....	Presenilin 1
PSD……..……..…....	Postsynaptic density
PV……..……..	Parvalbumin
RGC……..……...	Retinal ganglion cell
ROI……..……..…...	Region of interest
RT……..…...	Room temperature
SEM……..…....	Standard error of the mean
SF……..……..…...	Survival fraction
SOM……..…...	Somatostatin
TOR……..……..…...	Turnover rate
TPLSM……..…...	Two-photon laser scanning microscopy
TREM2……..…...	Triggering receptor expressed on myeloid cells 2
V1……..……..	Primary visual cortex
VIP…….	Vasoactive intestinal peptide
WT…….	Wild type

1 INTRODUCTION

More than 100 years ago Alois Alzheimer first described a case of what he considered a 'peculiar disease of the cerebral cortex' (Alzheimer, 1907; Strassnig and Ganguli, 2005). A women aged 51 years presented amongst others with delusions, rapid decline of memory function and disorientation (Alzheimer, 1907). After her death at the age of 55, histopathological examination of her brain revealed unprecedented neuropathological features, such as 'miliar foci' and 'peculiar changes of neurofibrils' (Alzheimer, 1907; Strassnig and Ganguli, 2005). This form of dementia was accordingly named after the person who first described it – Alzheimer's disease (AD). Ever since much research has been undertaken to elucidate genetic, molecular and cellular underpinnings of AD, but despite the huge progress that has been achieved within these past 100 years, still to date we haven't understood the pathogenesis in its entirety and as a result lack sufficient treatment capable of curing or halting the progression of this devastating ailment.

With this work I aimed at gaining further knowledge about the impact of one of the main peptides and its assemblies implicated in the disease, namely the amyloid-β peptide (Aβ) and amyloid plaques, on neuronal structure and function by employing state of the art *in vivo* imaging techniques in a transgenic mouse model of the disease.

In the first part of my thesis I employed the APP/PS1 (Amyloid Precursor Protein/Presenilin 1) mouse model to assess alterations of pre- and postsynaptic structures and the impact of plaques proximity on these changes. In addition, I addressed the question whether the plaque associated synaptic pathology can be halted by pharmacologically interfering with Aβ production. To this end I chronically administered a novel selective γ-secretase inhibitor and monitored synaptic structures together with amyloid plaques *in vivo* throughout the treatment period.

In the second part of my thesis I addressed the question whether the observed structural alterations observed in the APP/PS1 mouse model might be reflected in altered neuronal response properties. I thus characterized neuronal activity patterns in the primary visual cortex (V1) of AD transgenic mice by means of *in vivo* two photon calcium imaging in behaving mice.

1.1. Alzheimer's disease

1.1.1. Human neuropathology

Alzheimer's disease (AD) is characterized by a progressive decline in memory function and cognition that can be classified into three distinct yet continuous stages: preclinical AD, mild cognitive impairment (MCI) and dementia due to Alzheimer's disease (Albert et al., 2011; Jack et al., 2011; McKhann et al., 2011; Sperling et al., 2011). AD patients in stages II and III typically present with impairments in cognitive domains, such as memory (in particular episodic memory), executive function, attention, language or visuospatial skills, all of which can be assessed by a number of clinical tests (Albert et al., 2011). The inability to pursue common daily activities marks the conversion form MCI to dementia (McKhann et al., 2011). The terminal phase is characterized by a complete dependence on caregiving and eventual death occurring on average 4-8 years after diagnosis (Brookmeyer et al., 2002; Helzner et al., 2008; Larson et al., 2004), most commonly caused by pneumonia or dehydration (Ganguli et al., 2005). Conclusive diagnosis, however, can only be made upon neuropathological examination (Hyman, 1997; McKhann et al., 2011). Histopathology of AD comprises, in addition to neuronal loss, cortical atrophy and glial activation, two cardinal lesions: extracellular deposits of the amyloid-beta peptide, so-called amyloid plaques, as well as intracellular accumulations of the hyperphosphorylated microtubule-associated protein tau (Figure 1) (Alzheimer, 1907; Hyman, 1997; Mann, 1985; Perl, 2010; Schellenberg and Montine, 2012). Tau pathology can manifest within neuronal somata, referred to as tangles, or within neurites, called neuropil threads (Serrano-Pozo et al., 2011). Tangles emerge in a spatiotemporal manner, allowing for categorization into Braak stages (I-VI). Brain regions affected by the pathology are entorhinal cortex (Braak I-II), subsequently limbic regions (Braak III-IV) and eventually the remaining neocortex (Braak V-VI) (Braak and Braak, 1991).

Amyloid plaques can appear in two different forms: diffuse – or cotton wool plaques - and dense core plaques (D'Andrea and Nagele, 2010; Serrano-Pozo et al., 2011). Only the latter type possesses a high concentration of bundles of amyloid fibrils in the center and is associated with a number of cytopathological features, such as the accumulation of activated microglia and reactive astrocytes, dystrophic and curved neurites and synapse loss (Itagaki et al., 1989; Knowles et al., 1999; Serrano-Pozo et al., 2011). Aβ deposits can furthermore be observed within vessel walls of arteries, veins and capillaries, a phenomenon called cerebral amyloid angiopathy (CAA) (Attems et al., 2010; Joachim et al., 1988; Vinters, 1992). In comparison to tau

pathology, amyloid plaque pathology seems to follow a different and less strict distribution pattern during the course of the disease. Initial deposition is found in the basal neocortex (Braak A), subsequently infiltrating adjacent areas and the hippocampus (Braak B) and eventually affecting all cortical areas (Braak C) (Braak and Braak, 1997). The causal relevance of amyloid plaques to the cognitive decline, however, is subject of debate. On the one hand, cytopathological characteristics are clearly associated in a spatiotemporal manner with these deposits in humans and mice (Liebscher and Meyer-Luehmann, 2012; Schellenberg and Montine, 2012). On the other hand, the occurrence of plaques – in contrast to tangles – does not correlate well with disease severity (Giannakopoulos et al., 2009; Nelson et al., 2012), and recent evidence suggests that amyloid deposition can even occur decades before clinical symptoms arise (Gelosa and Brooks, 2012; Reiman et al., 2012). Amyloid pathogenesis is, hence, considered to initiate a set of downstream molecular and cellular events, thereby triggering synapse loss, tau pathology and eventual neuronal death (see section "Amyloid cascade hypothesis") (Haass and Selkoe, 2007; Hanger et al., 2009; Hardy et al., 1998; Hardy and Selkoe, 2002). Intriguingly, the best correlate of the cognitive decline is a loss of synapses in cortex and hippocampus, which already puts the spotlight on these neuron-neuron contact sites in AD research (Coleman et al., 2004; DeKosky et al., 1996; Masliah et al., 1991; Scheff and Price, 2006; Terry et al., 1991).

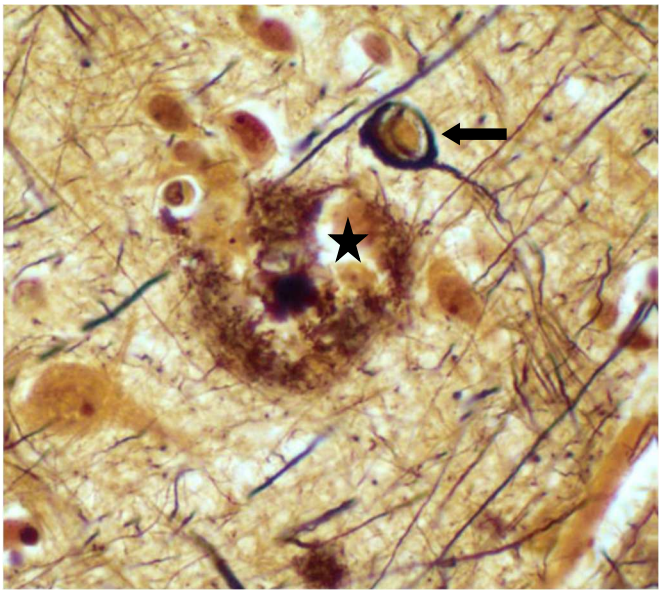

Figure 1: Hallmarks of AD pathology. *Photomicrograph depicting an amyloid plaque (star) and a neurofibrillary tangle (arrow). Neocortical section of an AD patient stained with modified Bielschowsky method. Reprinted from Acta Neuropathologica with permission from Springer (Schellenberg and Montine, 2012).*

1.1.2. Genetics of Alzheimer's disease

Most cases of AD occur sporadically (~95%) and present as a late-onset or senile form of AD (age of onset > 65 years). Only a minority of less than 5% of all cases represents familial Alzheimer's disease (FAD), attributable to autosomal dominant mutations within one of the 3 genes: Amyloid Precursor Protein (*APP*) (Figure 2) (Karran et al., 2011; Wilquet and De Strooper, 2004), Presenilin1 (*PSEN1*) or Presenilin2 (*PSEN2*), which present as early-onset or pre-senile AD (Brouwers et al., 2008; Cruts and Van Broeckhoven, 1998). Knowledge of FAD mutations gave rise to the generation of transgenic mouse models, by introducing the respective mutated genes into the mouse genome.

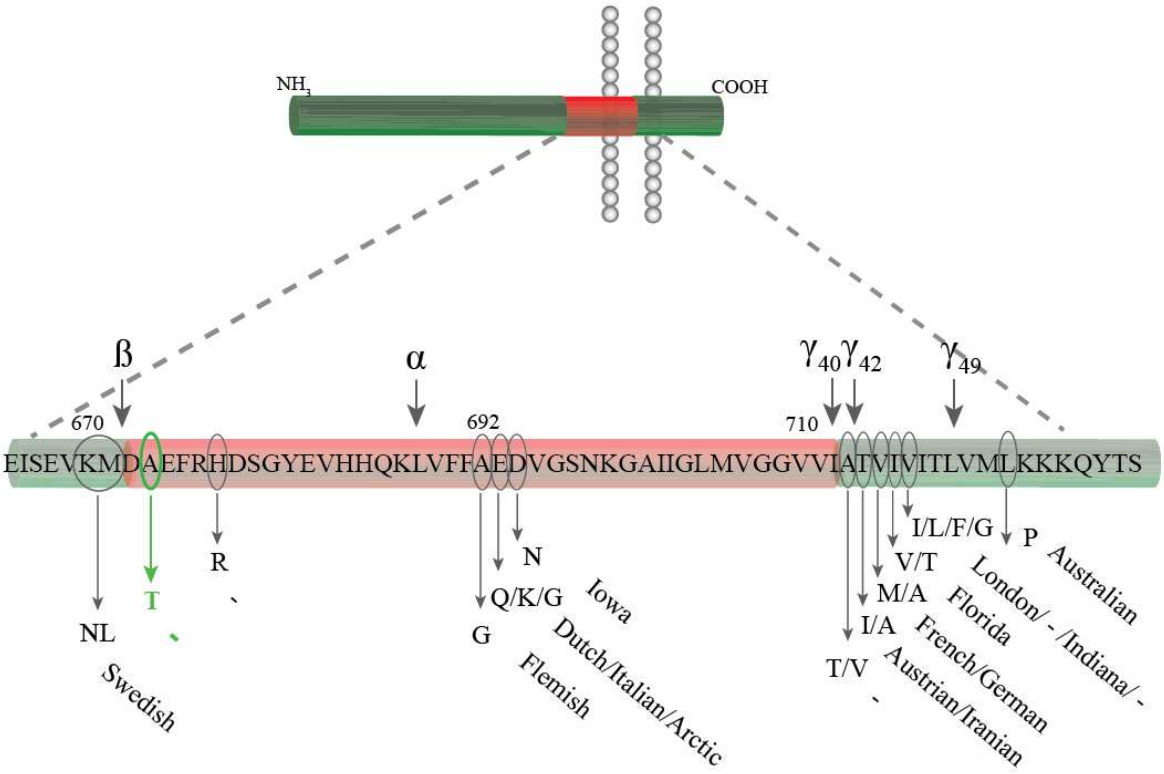

Figure 2: Familial AD mutations within the APP gene.
Known mutations of familial AD cases are marked along the amino acid sequence of Aβ (red), thereby revealing their intimate relationship to the cleavage sites of all 3 secretases. A protective mutation (A673T, known as Icelandic mutation) is denoted by a green ellipse at the β-secretase cleavage site.

The risk of late-onset AD is known to be increased by a number of susceptibility genes, such as *APOE4* (Apolipoprotein E allele ε4) (Corder et al., 1993; Mahley and Huang, 1999; Strittmatter et al., 1993) and *SORL1* (Sortilin Related Receptor 1) (Reitz et al., 2011; Rogaeva et al., 2007). Recent, large genome-wide association studies (GWAS) have unraveled even more genes implicated in late-onset AD, such as *PICALM* (Phosphatidylinositol Binding Clathrin Assembly Protein), *EPHA1* (Ephrin Type A Receptor 1), *ABCA7* (ATP Binding Cassette Subfamily A Member 7), *BIN1* (Bridging Integrator 1 or Amphiphysin), *CD33, CLU* (Clusterin), *CR1* (Complement Component 3b/4b Receptor 1), *CD2AP* (CD2-associated Protein), reviewed by (Schellenberg and Montine, 2012), *TREM2* (Triggering Receptor Expressed On Myeloid Cells 2) (Guerreiro et al., 2013; Jonsson et al., 2013), and in a large meta-analysis of previously published GWAS studies *HLA-DRB5* (Major Histocompatibility Complex, Class II, DR beta 5), *HLA-DRB1* (Major Histocompatibility Complex, Class II, DR beta 1), *PTK2B* (Protein Tyrosine Kinase 2 Beta), *SLC24A4* (Solute Carrier Family 24 Member 4), *RIN3* (Ras And Rab Interactor 3), *DSG2* (Desmoglein 2), *INPP5D* (Inositol Polyphosphate-5-Phosphatase D), *MEF2C* (Myocyte Enhancer Factor 2C), *NME8* (NME/NM23 Family Member 8 or Thioredoxin Domain Containing 3), *ZCWPW1* (Zinc Finger CW-Type And PWWP Domain Containing 1), *CELF1* (CUGBP (CUG Triplet Repeat, RNA Binding Protein 1), Elav-Like Family Member 1), *FERMT2* (Ferritin Family Member 2), *CASS4* (Cas Scaffolding Protein Family Member 4) (Lambert et al., 2013).

In contrast to loci that are associated with an increased risk for developing AD, a recent study also identified mutations within the *APP* gene (A673T, 'Icelandic mutation'), which seem to serve a protective role for cognition and to promote longevity (Jonsson et al., 2012). The described mutation resides close to the β-secretase cleavage site within the *APP* gene, thereby reducing the generation of Aβ (Benilova et al., 2014; Jonsson et al., 2012; Maloney et al., 2014) and thus adding further credence to the amyloid hypothesis (see below).

1.1.3. Amyloid cascade hypothesis

The prevailing tenet in AD research, the amyloid cascade hypothesis, was proposed after the successful sequencing of the amyloid-β peptide (Glenner et al., 1984) and the discovery that this very peptide represents the main component of amyloid plaques typical of AD (Masters et al., 1985). Subsequent cloning of APP allowed the elucidation of its role in Aβ generation. Further support for the amyloid hypothesis came from

the first identification of a mutation within the *APP* gene in autosomal dominant AD (Goate et al., 1991). In short, the amyloid hypothesis states that increased production and accumulation of predominantly the long form of Aβ (Aβ42) induces numerous molecular and cellular events, such as synaptic dysfunction, neuritic pathology, changes in neuronal ion homeostasis, glial activation, oxidative stress, altered kinase/phosphatase activation inducing tangle formation and eventually cell death (Hardy and Selkoe, 2002; Hardy and Higgins, 1992; Selkoe, 1991). Whereas the first incarnation of the amyloid hypothesis posited amyloid plaques as the central, disease-causing agent, research over the past two decades has identified a precursor of plaques, namely Aβ oligomers, as the toxic moiety (reviewed by (Haass and Selkoe, 2007; Hardy and Selkoe, 2002; Pimplikar, 2009)). The highest concentration of Aβ oligomers, however, is found within and surrounding amyloid plaques (Koffie et al., 2009), reconciling the two schools of thought to some degree. Plaques were thus suggested to present a reservoir of Aβ oligomers with insoluble fibrils being in equilibrium with circumjacent oligomers and protofibrils, respectively (Haass and Selkoe, 2007; Koffie et al., 2009; Mucke and Selkoe, 2012; Shankar et al., 2008). These findings underscore the causal relevance of both Aβ oligomers and plaques to AD pathology.

1.1.4. Amyloid - β generation

The key molecule in AD, the amyloid beta- peptide (Aβ), is a hydrophobic peptide with a molecular weight of 4kDa, which is derived upon sequential cleavage of a larger type I transmembrane protein, the amyloid precursor protein (APP) via a process termed regulated intramembrane proteolysis (RIP) (Haass, 2004; Haass and Selkoe, 2007; Lichtenthaler et al., 2011). In the amyloidogenic pathway, the first cleavage of APP is performed by the β - secretase (also known as beta-site APP cleaving enzyme 1, or BACE1) preferentially within early endosomes (Haass, 2004; LaFerla et al., 2007) (Figure 3). The resulting C-terminal fragment (APP-CTF) is further cleaved intramembranously by the γ-secretase, thereby deliberating the Aβ peptide into vesicles or the extracellular space, and releasing the amyloid intracellular domain (AICD) into the cytosol (Haass and Selkoe, 2007; Steiner et al., 2008).

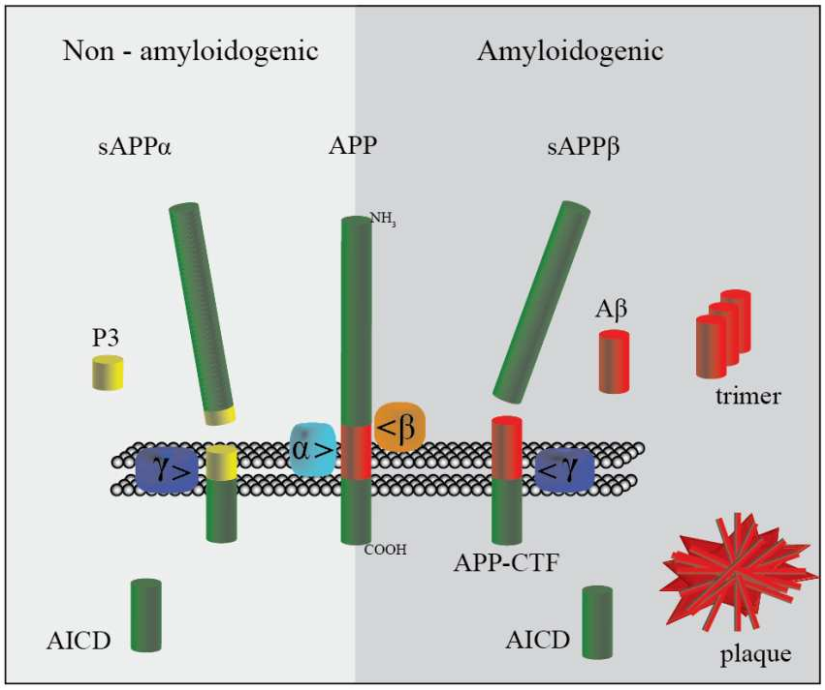

Figure 3: APP processing by secretases.
APP is first shedded at its ectodomain either by the β-secretase (orange) or the α-secretase (light blue) releasing a soluble APPβ or APPα fragment, respectively. The remaining APP C-terminal fragment within the membrane (APP-CTF) is further cleaved by the γ-secretase (dark blue) via regulated intramembrane proteolysis, releasing Aβ (or a P3 fragment (yellow) in case of preceding α-secretase cleavage) and an APP intracellular domain (AICD). Aβ monomers oligomerize, thereby forming higher molecular weight species, which are eventually deposited as amyloid plaques within the parenchyma.

The γ-secretase constitutes a tetrameric complex consisting of presenilin 1 or 2 (the catalytic subunit), nicastrin (NCT), anterior pharynx-defective 1 (APH-1) and presenilin enhancer 2 (PEN-2) (Fraering et al., 2004; Kimberly et al., 2003; Steiner, 2008). Depending on the exact γ-secretase cleavage site, the released Aβ peptide can be of different length, with longer Aβ peptides being more prone to aggregation (Bitan et al., 2003; Burdick et al., 1992; Jarrett et al., 1993; Yan and Wang, 2006). In this regard, several known familial AD mutations reside either within the APP or the presenilin genes, thereby affecting APP cleavage and shifting the ratio between Aβ42/Aβ40 towards the longer and hence more amyloidogenic Aβ42 peptide (Chartier-Harlin et al., 1991; Goate et al., 1991; Haass and Selkoe, 2007; Murrell et al., 1991; Murrell et al., 2000). For instance, most of the FAD mutations within the APP gene cluster around the secretase cleavage sites (Figure 2), thereby altering Aβ generation in a quantitative and qualitative manner (Karran et al., 2011; Wilquet and De Strooper, 2004). Upon secretion, Aβ aggregation is thought to follow a nucleation-dependent polymerization process, in which Aβ monomers form higher molecular weight oligomers and protofibrils, before eventual aggregation into insoluble amyloid plaques (Harper and Lansbury, 1997).

APP can furthermore be processed in a non-amyloidogenic manner (Figure 3), in which case APP is initially cleaved by the α–secretase within the Aβ domain, releasing the soluble APPα fragment (sAPPα) and

hence preventing Aβ generation (Lichtenthaler, 2011, 2012). Subsequent γ-cleavage releases a P3 peptide and the AICD (Lichtenthaler, 2012; Postina, 2012). As AD is believed to represent a disease of synaptic failure (Koffie et al., 2011; Selkoe, 2002) I will focus in the following paragraph on the effects of Aβ on synapses.

1.1.5. Molecular and cellular effects of Aβ – the basis of synaptotoxicity

Aβ is thought to serve both a physiological as well as pathological role. It co-localizes with postsynaptic structures, potentially binding to molecular components of the postsynapse, such as NMDA-, EphB receptors or PrP (Cisse et al., 2011; Lacor et al., 2007). Under physiological conditions Aβ release is regulated by neuronal activity (Bero et al., 2011; Cirrito et al., 2005) and is assumed to provide a negative feedback signal in order to prevent excitotoxicity (Kamenetz et al., 2003; Parihar and Brewer, 2010; Pearson and Peers, 2006). Aβ has furthermore been proposed to play a role in learning and memory in young WT mice (Morley et al., 2010) and to facilitate neuronal growth and survival (Bishop and Robinson, 2004). On the other hand, a large body of literature of both *in vitro* and *in vivo* studies provides evidence for a synaptotoxic effect of particularly Aβ42 (reviewed by (Hardy and Selkoe, 2002; Koffie et al., 2011; Mucke and Selkoe, 2012; Palop and Mucke, 2010)). More specifically, Aβ is assumed to dampen synaptic efficacy eventually resulting in a loss of synapses (Koffie et al., 2011; Mucke and Selkoe, 2012). In this respect, Aβ has been shown to impair the induction of long-term potentiation (LTP) (Danysz and Parsons, 2012; Li et al., 2011a; Shankar et al., 2008; Walsh et al., 2002) and to facilitate long-term depression (LTD) (Hsieh et al., 2006; Kim et al., 2001; Li et al., 2009), by triggering NMDA and AMPA receptor internalization or desensitization (Hsieh et al., 2006; Snyder et al., 2005) and activating extrasynaptic NMDA as well as 7α – nicotinic acetylcholine receptors (Hsieh et al., 2006; Li et al., 2009; Li et al., 2011b; Shankar et al., 2007; Wang et al., 2000). Several molecular pathways are either involved in or modulated by Aβ induced changes in synaptic receptor composition and efficacy, such as calcineurin, glycogen synthase kinase 3-beta (GSK-3β), p38 mitogen-activated protein kinase (MAPK), calcium/calmodulin-dependent protein kinase II (CaMKII) or cyclic AMP response element binding protein (CREB) signaling pathways (Koffie et al., 2011; Shankar et al., 2007; Tackenberg et al., 2009). Ultimately, all these alterations are thought to result in synapse shrinkage and finally in complete synapse loss (Koffie et al., 2011). In addition to those direct Aβ - mediated effects on neurons, the deposition of plaques triggers an immunresponse apparent by the activation of microglia and astrocytes, which accumulate around plaques (Itagaki et al., 1989; Nagele et al., 2004). Their role in AD pathophysiology, however, is controversially

discussed as both a protective and a detrimental role have been demonstrated (Johnston et al., 2011; Koistinaho et al., 2002; Morgan et al., 2005; Pihlaja et al., 2008).

Interestingly, at the level of neuronal circuits the accumulation of Aβ was shown to induce aberrant patterns of neuronal activity, seen in a higher fraction of hypo – and hyperactive cells resulting in network hypersynchrony and -excitability that give rise to spontaneous epileptiform discharges (Busche et al., 2008; Mucke and Selkoe, 2012; Palop et al., 2007; Palop and Mucke, 2010). This phenomenon has been recently linked to impaired function of particularly parvalbumin (PV) - positive inhibitory interneurons in an AD transgenic mouse model (Verret et al., 2012). Probing synaptic and network function is preferably done in a chronic fashion over extended periods of time and in a living animal, for which *in vivo* two-photon microscopy is ideally suited.

1.2. *In vivo* two - photon imaging

1.2.1. Two - photon laser scanning microscopy

The advent of two - photon laser scanning microscopy (TPLSM) (Denk et al., 1990) in conjunction with the development of genetically encoded probes has facilitated the longitudinal monitoring of structure and function of cells and subcellular compartments in living animals. The method is based on the excitation of a fluorophore by the simultaneous absorption of two photons. This principle has two major advantages compared to single photon microscopy: (A) the utilization of longer excitation wavelengths (near infrared), thereby allowing for deeper tissue penetration and (B) focal excitation, which in turn reduces photobleaching and -toxicity (Denk et al., 1990; Svoboda and Yasuda, 2006). The light source of a TPLSM setup is typically a solid-state pumped laser (often a Ti:sapphire laser), producing short laser pulses (fs to ps pulse width) at high frequencies (MHz). Via appropriate deflection mirrors and lenses a collimated laser beam enters the objective's back aperture and is focused onto the specimen. In order to scan over the sample the focus spot of the beam is shifted by the scanning unit, which commonly comprises a set of two galvanometric mirrors deflecting the beam in the x - and y-axis (De Paola et al., 2006). Image acquisition speed is hence limited by the velocity of those galvanometric mirrors. Faster scanning is achieved by a resonant mirror, that oscillates at its resonant frequency (used in the second part of this thesis) or acousto-optical deflectors (AODs), which

employ acoustic waves passing through a transparent crystal to rapidly modify its diffraction pattern thereby varying the deflection of the laser beam (Chen et al., 2012b; De Paola et al., 2006).

Only within the focus is the photon density sufficiently high to allow for simultaneous absorption of two photons by the fluorophore and subsequent emission of a single photon, now endowed with a wavelength, which is slightly longer than half of the excitation wavelength. Emitted photons enter the objective and are eventually collected by photomultiplier tubes (PMT). PMTs rely on the photoelectric effect, such that incoming photons impinge on a photocathode and release an electron, which is amplified via a set of dynodes. Eventually electrons will reach the anode and each incoming photon is converted into a current pulse.

Chronic two-photon imaging of neuronal structures in the living mouse to date is only feasible after the creation of optical access to the brain. To this end a so-called cranial window is implemented, using either the open skull or closed skull preparation technique. The open skull preparation (technique of choice in this thesis) entails a circular craniotomy after which the exposed cortex is covered by a glass coverslip and the window is sealed with dental acrylic (Holtmaat et al., 2009). The closed skull preparation is carried out by thinning the skull above the cortical region of interest (Yang et al., 2010). Both techniques have their advantages and drawbacks. The area of the cortex accessible to imaging is very small with cranial thinning, and thinning needs to be executed several times when long imaging intervals shall be achieved, as bone grows back over time. Re-thinning is time – consuming, requires additional anesthesia and the resulting bone layer might vary in thickness, thereby altering window quality. In contrast, open skull preparations allow longitudinal imaging (typically) without further intervention. A major concern regarding the open skull preparation, however, is the induction of an inflammatory response. Immunohistochemical analysis at varying time points post window implantation revealed an initial increase in the number of glial fibrillary acidic protein (GFAP) positive cells, representing activated astrocytes, within the window region, which was normalized 30 days after implantation (Holtmaat et al., 2009). In this thesis I employed the open skull preparation and implemented a four week recovery period before imaging commenced to address these concerns.

The TPSLM approach has found broad applications in transgenic mouse models of AD, the main findings of which have been summarized in a review as part of my PhD (Liebscher and Meyer-Luehmann, 2012) and shall be briefly laid out in the following sections.

1.2.2. Structural *in vivo* imaging

1.2.2.1. Dendritic spines

As pointed out above, AD is considered a disease of synaptic failure (Selkoe, 2002) and the loss of synapses in cortex and hippocampus is a strong histological correlate of the cognitive decline (DeKosky et al., 1996; Masliah et al., 1991; Terry et al., 1991). Consequently, the study of synaptic structures should allow for crucial insights into disease pathology. To this end, we analysed dendritic spines, which represent structural correlates of the main sites of excitatory synaptic input onto pyramidal neurons ((Gray, 1959), reviewed by (Yuste, 2011)). Spines are small dendritic protrusions that were first described by Santiago Ramón y Cajal in 1888 (Cajal, 1888; Garcia-Lopez et al., 2007) and are still to date subject of extensive research. They can be classified into thin, mushroom, stubby and branched subtypes according to their shape and size (Harris et al., 1992). Although dendritic spines strikingly differ in size, shape and subcellular composition, some general features are observed in the vast majority of these structures, such as a spine neck and - head (Harris et al., 1992; Peters and Kaiserman-Abramof, 1970; Tashiro and Yuste, 2003), a feature that allows for electrical and biochemical compartmentalization of the spine from the parent dendrite and facilitates a high degree of neuronal connectivity (reviewed by (Bosch and Hayashi, 2012; Yuste, 2011)).

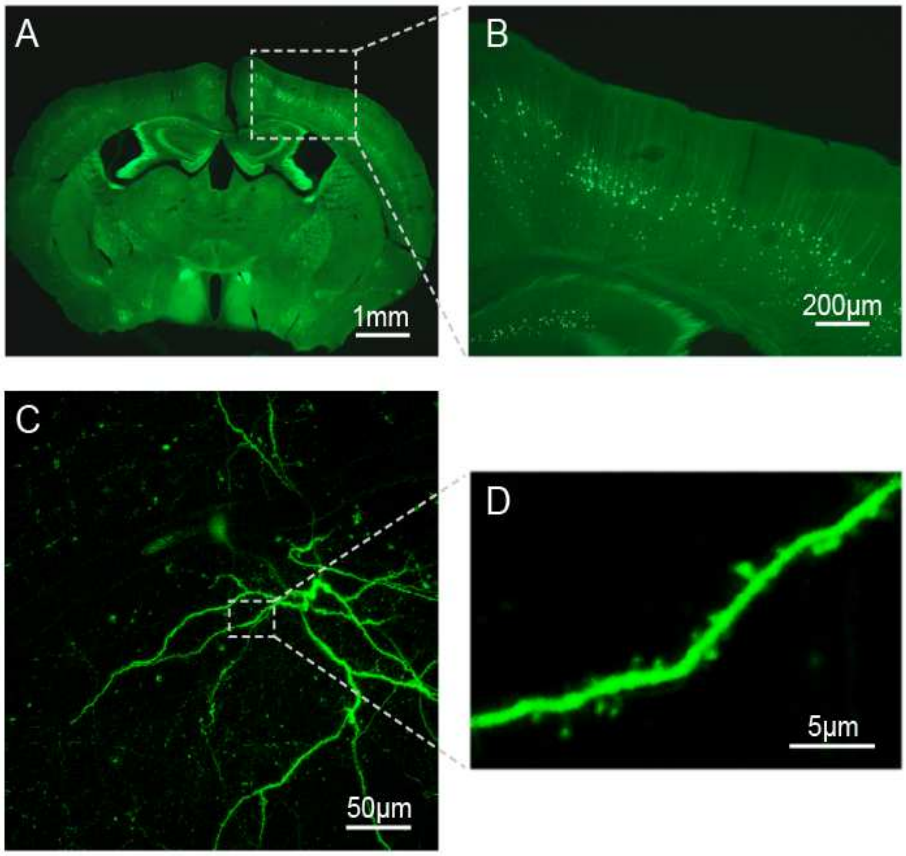

Figure 4: Sparse labeling of cortical neurons in the GFP-M mouse line.
(A) Coronal brain section of a GFP-M mouse (1.3mm posterior from Bregma) at low magnification. (B) Higher magnification of somato-sensory cortex demonstrating GFP expression in a subset of layer V pyramidal neurons. (C) Maximum intensity projection of an in vivo stack over ~ 450 µm depicting a pyramidal neuron with its apical dendrites and distal tufts. (D) High magnification of a dendritic tuft with its spines imaged in vivo.

Dendritic spines, the structural correlates of excitatory postsynapses are endowed with a varying set of neurotransmitter receptors and ion channels that are embedded in the membrane and tethered to the postsynaptic density (PSD), a protein rich structure connected to the postsynaptic membrane, which in addition bears scaffolding proteins, adhesion molecules and signaling proteins, e.g. kinases and phosphatases, as well as cytoskeletal elements (Dosemeci et al., 2007; Keith and El-Husseini, 2008; Sheng and Kim, 2011). In particular large, mature, mushroom like spines are furthermore equipped with a spine apparatus, a specialization of the smooth endoplasmatic reticulum (ER) extending from the dendrite into the spine (Cooney et al., 2002; Gray, 1959; Segal et al., 2010), and polyribosomes, allowing for local protein synthesis (Steward and Schuman, 2001). Spine size positively correlates with the size of the PSD and the number of glutamate receptors, supporting the notion that bigger spines correspond to stronger synapses (Kasai et al., 2003). Although the presence of a spine does not *a priori* indicate the existence of a functional synapse, the fraction of non-synaptic spines in cortex seems rather low (~4%) (Arellano et al., 2007).

Importantly, spines are suggested to embody the structural basis of information storage (Bhatt et al., 2009; Caroni et al., 2012; Yuste, 2011; Yuste and Bonhoeffer, 2004). Despite the large proportion of highly stable cortical spines that are assumed to persist for even as long as a whole lifetime (Grutzendler et al., 2002; Yang et al., 2009), constant remodeling of synaptic networks occurs to allow for the adaptation of the organism to environmental changes. This remodeling not only takes place at the molecular level, but in addition involves structural reorganization (reviewed by (Bailey and Kandel, 1993; Caroni et al., 2012)). Recent advances in imaging techniques have shed light on the underlying kinetics of this structural rearrangement. Intriguingly, spines are flexible and motile structures, and a certain fraction is lost and gained even under baseline conditions (Bosch and Hayashi, 2012; Holtmaat et al., 2009; Holtmaat et al., 2005; Segal, 2005; Trachtenberg et al., 2002; Yuste and Bonhoeffer, 2004). LTP induction *in vitro* (De Roo et al., 2008a; Engert and Bonhoeffer, 1999; Maletic-Savatic et al., 1999; Toni et al., 1999) or the application of a sensory deprivation – or learning paradigm *in vivo* further increase spine turnover and a proportion of new spines persists over a long period, forming a potential correlate of functional and behavioural changes (Fu et al., 2012; Hofer et al., 2009; Holtmaat et al., 2006; Keck et al., 2008; Xu et al., 2009; Yang et al., 2009). These data strongly argue in favor of spines acting as a physical correlate of learning, memory formation and -maintenance and hence, underscore the relevance of altered synaptic function to the cognitive decline typical of AD (see section 1.1.5. Molecular and cellular effects of Aβ**).** Given that the entire brain is densely packed with synapses, it is difficult to study single synaptic structures longitudinally *in vivo*. A sparse labeling of defined neuronal populations therefore represents a pre-requisite to chronically monitor single dendritic spines in the brain. I thus took advantage of a transgenic mouse line (GFP-M), that expresses GFP under the neuronal promoter Thy-1, which in cortex results in a sparse, golgi-like staining of predominantly layer V pyramidal neurons ((Feng et al., 2000), Figure 4).

1.2.2.2. Axonal boutons

The presynaptic structural counterparts of spines are axonal boutons. Excitatory synapses are formed either on en passant (bulbous distensions of the axonal backbone) or terminaux boutons (short branches bearing a bulbous structure, resembling dendritic spines) (Anderson and Martin, 2001; De Paola et al., 2006). Boutons typically contain a number of neurotransmitter filled vesicles and an active zone, the vesicle docking and release site. The active zone is an electron dense area close to the membrane comprised of e.g. scaffolding -, vesicle docking and priming - , cytoskeletal proteins and voltage-dependent Ca^{2+} channels, which is

connected to cell adhesion molecules. Boutons, similar to spines, are dynamic structures, although much less is known about the former *in vivo*. Average stoichiometry between boutons and spines in hippocampus is assumed to be 1:1 (Kuwajima et al., 2012; Popov and Stewart, 2009; Shepherd and Harris, 1998). Nonetheless, about 3.5% of mushroom spines in the dentate gyrus form multiple synaptic contacts onto more than 2 axons (Popov and Stewart, 2009) and about 20% of boutons on CA3 originating axons contact 2-4 postsynaptic densities (PSD) (Shepherd and Harris, 1998; Sorra and Harris, 1993). Similar results were also found in the barrel cortex (Knott et al., 2006), suggesting that the number of multisynaptic boutons is higher than that of multisynaptic spines. Further credence to that notion is added by the fact that spine growth precedes synapse formation and newly formed spines preferentially target multisynaptic boutons (Knott et al., 2006). In addition, *in vivo* two-photon imaging studies indicate that boutons are more stable than spines, demonstrated by a higher bouton survival fraction (SF) of thalamocortical and intracortical projection neurons (SF: thalamocortical ~85% and intracortical ~75% over 24 days) than apical tuft spines of layer Vb pyramidal neurons (SF: ~60-70% over 24 days) (De Paola et al., 2006; Holtmaat et al., 2009; Holtmaat et al., 2005).

1.2.3. Structural *in vivo* imaging in AD transgenic mouse models

In vivo two-photon microscopy of APP transgenic mice has been employed to elucidate the kinetics and temporal sequence of amyloid pathology and the associated structural and functional alterations (see review (Dong et al., 2010; Liebscher and Meyer-Luehmann, 2012)). Structural imaging has been performed to analyse the formation and growth of amyloid plaques within the parenchyma (Bolmont et al., 2008; Burgold et al., 2011; Christie et al., 2001; Hefendehl et al., 2011; Meyer-Luehmann et al., 2008; Yan et al., 2009) and blood vessel walls (cerebral amyloid angiopathy, CAA) (Garcia-Alloza et al., 2006b; Prada et al., 2007), neurofibrillary tangles (de Calignon et al., 2010; de Calignon et al., 2009; Spires-Jones et al., 2008), neurites (Meyer-Luehmann et al., 2008; Tsai et al., 2004), dendritic spines (Bittner et al., 2010; Jung et al., 2011; Spires-Jones et al., 2007; Spires et al., 2005; Tsai et al., 2004) and microglia (Bolmont et al., 2008; Fuhrmann et al., 2010; Koenigsknecht-Talboo et al., 2008; Liu et al., 2010). These studies have shown that plaques grow slowly but steadily over weeks and months (Burgold et al., 2011; Hefendehl et al., 2011; Yan et al., 2009). Neurites in close proximity to plaques exhibit characteristic alterations, such as curved trajectories, dystrophic distensions and even breakage (Garcia-Alloza et al., 2010; Garcia-Alloza et al., 2006a; Tsai et al., 2004). Spines

near plaques possess a high turnover rate and a lower density compared to WT mice and to dendrites further away from plaques (Bittner et al., 2012; Liebscher et al., 2014; Tsai et al., 2004). Moreover, amyloid plaques attract immune cells. As such microglia have been shown to migrate by extending the majority of their processes towards the plaque (Bolmont et al., 2008). Once they have reached the plaque microglial cell bodies become stationary but their processes continuously sample the environment (Bolmont et al., 2008). These plaque-associated structural alterations follow with a delay of days – weeks upon plaque formation.

1.2.4. Functional *in vivo* imaging

1.2.4.1. Calcium indicators

Structural changes of a neuron and its processes are believed to result in functional changes, thereby modifying activity levels and response properties of affected neurons. Traditionally neuronal activity has been studied by means of electrophysiology at the level of cell populations/cell ensembles (electro-encephalography, local field potential recordings) or single neurons (patch clamp, extracellular recordings), essentially detecting changes in membrane potential or current flow. These techniques are either limited in spatial resolution and/or don't allow for monitoring of multiple identified cells simultaneously and repeatedly over periods of weeks and months. Microscopic imaging techniques on the other hand provide single cell resolution of up to hundreds of cells at a time, which can be followed over long intervals. In order to convert neurons' electrical signals into a change in fluorescence indicators that faithfully detect changes in ion concentrations, such as calcium, or membrane potential are needed.

Calcium acts as a universal second messenger regulating signaling events in many cells and cell compartments (Berridge et al., 2000). Synaptic inputs and action potentials increase intraneuronal calcium concentrations facilitated by the opening of voltage-sensitive calcium channels, release form internal stores or influx via glutamate receptors (reviewed by (Higley and Sabatini, 2008)). In contrast to earlier synthetic calcium dyes (OGB-1, Fura-2, Fluo-4) genetically encoded calcium indicators (GECIs) allow for cell type - specific targeting, labeling of subcellular compartments and chronic expression (Hendel et al., 2008; Knopfel et al., 2006; Tian et al., 2012b). GECIs are comprised of a calcium binding domain, such as calmodulin or troponin C, and one or two fluorescent proteins (Griesbeck, 2004; Looger and Griesbeck, 2012; Mank et al., 2008; Tian et al., 2012b). Calcium indicators bearing two fluorophores rely on fluorescence resonance energy

transfer (FRET) (e.g. Twitch, TN-XXL, YC3.60, D3cpV), where upon calcium binding the conformational change of the calcium binding protein brings the two fluorescent proteins in close proximity, causing a change in FRET and a corresponding change in the ratio of the two emitted wavelengths (Knopfel, 2012; Looger and Griesbeck, 2012; Tian et al., 2012a). Single fluorescent protein indicators are based on circularly permuted GFP (cpGFP) coupled to calmodulin and the M13 peptide (GCaMP) (Nakai et al., 2001; Ohkura et al., 2012; Tian et al., 2009). Upon calcium binding calmodulin and M13 undergo a conformational change, which shields the fluorophore from solvent quenching (Akerboom et al., 2009; Nakai et al., 2001), in turn causing a change in fluorescence.

In this thesis I employed one of the latest GCaMP versions (GCaMP6m) available at the time the experiments were conducted. GCaMP6m is characterized by an increased sensitivity, dynamic range and an excellent signal-to-noise ratio compared to previous GCaMP generations (Chen et al., 2013). Disadvantages of GCaMP6m (like most other GECIs) are its nonlinear relationship between spike rate (i.e. the frequency of action potentials (AP)) and the fluorescence signal, resulting in a supralinear increase of peak fluorescence with increasing spike rates and a low signal-to-noise ratio in lower AP ranges, as well as the slow kinetics (decay time upon stimulation with 1 AP in V1 *in vivo* ~270 ms), properties that allow for a detection rate of 94% of single APs (Chen et al., 2013). Despite the given limitations of GCaMP6m, this indicator should nonetheless allow capturing almost all visually driven responses, as the median peak instantaneous firing rate in V1 layer II/III cells is about 12Hz (Niell and Stryker, 2008). GECIs are commonly delivered via viral transduction employing adeno-associated viruses (AAVs), but more recently also Cre-dependent GCaMP reporter mice (Zariwala et al., 2012) as well as *Thy1*-GCaMP3 (Chen et al., 2012a) and *Thy1*-GCaMP6 mice were generated (Dana et al., 2014), allowing for stable and long term gene expression and targeting of specific neuronal subpopulations. We here used a virally mediated expression employing an AAV2/1-hsyn-GCaMP6m construct.

1.2.4.2. Mouse primary visual cortex

Aβ and amyloid plaques are associated with structural und functional neuronal alterations. To investigate the impact of amyloid deposition on neuronal response properties, we chose the mouse primary visual cortex (V1) as a model area.

At first glance the mouse indeed doesn't seem to be ideally suited to study the function of the visual system: mice have 100 times lower spatial acuity, 10 times lower contrast sensitivity and 5 times lower temporal resolution compared with humans (Gao et al., 2010). But despite a number of differences between the visual system of the mouse and higher mammals - most prominently the lack of an orderly arrangement of neurons with comparable response properties, such as orientation or ocular dominance maps (Hubener, 2003) – the general structure and basic neuronal response properties are very similar (Chalupa and Williams, 2008; Niell and Stryker, 2008). Furthermore, the advent of a broad spectrum of mouse specific molecular markers and genetic tools has enabled the study of neuronal development, anatomy, connectivity and function at the cellular and subcellular level. The function of the mouse visual system can be readily tested behaviourally and the underlying circuitry is considered to be based on common principles and rules of neuronal computation, which renders the mouse visual cortex an ideal model to study neuronal function.

The visual pathway, in short, involves the following stages: Light enters the eye and hyperpolarizes photoreceptor cells, which converge onto bipolar cells that in turn transmit the signal to a number of different retinal ganglion cell types (RGCs) (Wassle, 2004; Zhang et al., 2012). Within the optic nerve most of the retinal ganglion cells terminate within the lateral geniculate nucleus (LGN) of the thalamus and a smaller fraction projects directly to the superior colliculus (Erskine and Herrera, 2014), where they are thought to be involved in the control of eye movements. Less than 10% of RGCs project ipsilaterally (Figure 5, red), whereas the majority of RGC axons cross to the other hemisphere (Figure 5, blue) (Drager and Olsen, 1980; Erskine and Herrera, 2014; Grafstein, 1971). In the LGN, the inputs from the retina are retinotopically organized.

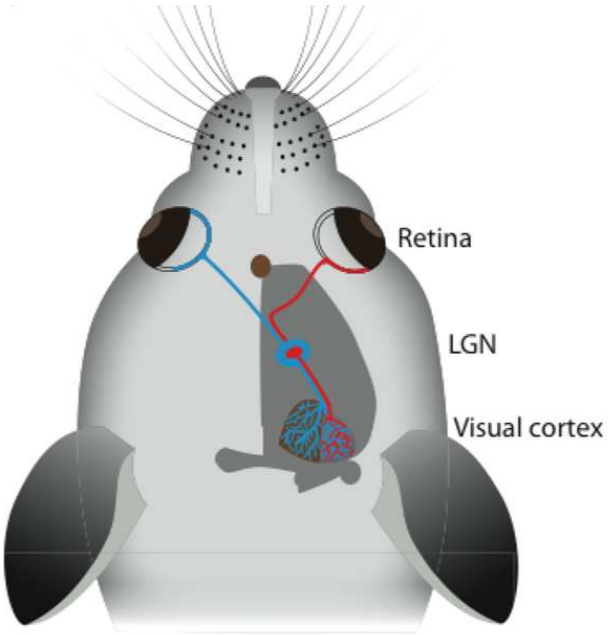

Figure 5: Visual system of the mouse.
Retinal ganglion cells from the ipsilateral (shown in red) and from the contralateral eye (shown in blue) project to the lateral geniculate nucleus (LGN) of the thalamus. LGN neurons relay information mainly to neurons in layer IV of the primary visual cortex (reprinted from Annual Review of Neuroscience with permission from Annual Reviews (Levelt and Hubener, 2012)).

Neurons of the LGN project to primary visual cortex synapsing mainly on layer IV neurons with the retinotopic organization being preserved (Hubener, 2003). The medial part of V1 (about 2/3 of V1) receives contralateral input only, whereas lateral V1 in addition receives ipsilateral input, too (binocular V1, see Figure 5) (Levelt and Hubener, 2012). Within V1 information flow occurs between excitatory neurons in a canonical microcircuit between layers II-VI, a common feature in many cortical areas (Douglas and Martin, 2004; Gilbert, 1983; Gilbert and Wiesel, 1983). In a highly simplified scheme, spiny stellate cells in layer IV drive pyramidal neurons in layer II/III, which synapse onto layer V pyramidal cells, that in turn project to layer VI neurons, which then project back to layer IV (Binzegger et al., 2004; Douglas and Martin, 2004, 2007; Kerlin et al., 2010). In addition, neurons receive further lateral input from their direct neighbours, as well as long-ranging feedforward and feedback input from many connected brain areas (Douglas and Martin, 2007; Ko et al., 2011). In addition, the activity of excitatory neurons is shaped by an intricate network of different types of inhibitory neurons (Atallah et al., 2012; Binzegger et al., 2004; Bock et al., 2011; Douglas and Martin, 2007; Hofer et al., 2011; Kerlin et al., 2010).

Much of our current understanding of neuronal function in V1 dates back to a set of pioneering experiments conducted by Hubel and Wiesel (Hubel and Wiesel, 1959, 1962, 1963). They were the first to reveal cardinal features of V1 neurons, such as receptive fields with elongated ON/OFF regions, hence primarily detecting edges and bars rather than circular shapes. This property allows for determining the orientation and the movement direction of visual stimuli. Further, most of the visually responsive cells can be classified as simple or complex cells by virtue of their receptive field composition and based on their linear or nonlinear spatial summation response properties (Hubel and Wiesel, 1962; Skottun et al., 1991). A significant proportion of neurons in rodent V1 can be driven to spike (Akerboom et al., 2012; Niell and Stryker, 2008; Ohki et al., 2005; Zariwala et al., 2012). Depending on the method used, the fraction of visually responsive cells ranges from 87% as measured with electrical recordings (Niell and Stryker, 2008) – a method that is restricted to the analysis of active neurons - , ~ 40 - 60% using the synthetic calcium indicator Oregon green bapta-1 (OGB-1) (Akerboom et al., 2012; Bock et al., 2011; Chen et al., 2013; Kerlin et al., 2010; Zariwala et al., 2012), and about 10-60% employing genetically encoded calcium indicators (Akerboom et al., 2012; Chen et al., 2013; Zariwala et al., 2012). Neurons in V1 are typically studied using well defined visual stimuli, such as moving gratings or bars of varying orientations and directions, either in a full field configuration or as local smaller patches, which also allow for the assessment of the retinotopic organization. Subsequently, indices reflecting the response selectivity to a given orientation or direction of visually responsive cells can be computed.

Most studies conducted over the past decade and hence much of our insight into V1 computation stems from experiments performed in anesthetized animals. Only very recently researchers have begun studying neuronal function in awake and behaving animals (Greenberg et al., 2008; Keller et al., 2012; Niell and Stryker, 2010; Sawinski et al., 2009). These studies revealed a second major component, in addition to visual input, modifying the responsiveness of cells in V1, namely motor activity (Keller et al., 2012; Niell and Stryker, 2010). Not only has motor activity been shown to potentiate visually driven responses to moving gratings (Lee et al., 2014; Niell and Stryker, 2010; Polack et al., 2013; Saleem et al., 2013), but also to drive neuronal activity in primary visual cortex, even in the complete absence of visual input (Fu et al., 2014; Keller et al., 2012; Lee et al., 2014).

Intriguingly, in a closed loop configuration in which the mouse's locomotion is directly coupled to the visual flow it perceives during most of the time (visual feedback), experimenter introduced mismatches between the expected and the actual visual flow, which gave rise to strong neuronal responses in the visual cortex (Keller et al., 2012). The underlying circuitry, however, remains elusive to date. These data indicate that already primary sensory cortices can be involved in presumed higher cortical functions, such as feedback mismatch detection. Moreover, many of these studies emphasize the fact that neuronal activity in the awake animal cannot be directly inferred from responses observed during anesthetized states (Greenberg et al., 2008; Haider et al., 2013). These sets of well-characterized neuronal response properties being based on – presumably – very different neuronal circuits make the primary visual cortex of mice an ideal area to study the impact of plaque pathology on neuronal circuit function.

1.2.5. Functional *in vivo* imaging in AD transgenic mouse models

Plaque deposition is accompanied by structural alterations that conceivably result in changes of neuronal functional, as they weaken synaptic efficacy and disrupt neuronal connectivity. To probe for changes in neuronal function, calcium imaging, employing synthetic calcium indicators, has been previously performed in AD transgenic mice (Figure 6).

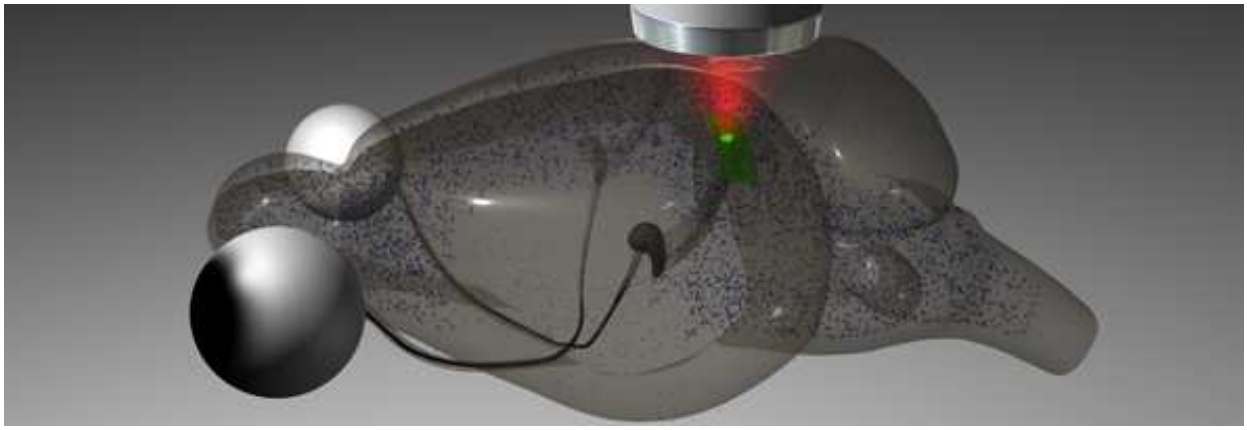

Figure 6: Schematic of the experimental approach.
Neuronal activity was assessed by two-photon imaging (indicated by the red laser beam) of fluorescence signals elicited by genetically encoded calcium indicators expressed in neurons of the visual cortex (green structures) in APP/PS1 transgenic mice. Globally deposited amyloid plaques are denoted by blue puncta. Visual pathways including the optic nerve originating within the eye, the lateral geniculate nucleus (LGN, dark grey bean-shaped structures) and the LGN projections to primary visual cortex are depicted.

APP/PS1 mice have been shown to exhibit altered baseline neuronal activity patterns, such as hypo- and hyperactivity, which in some studies was spatially confined to amyloid plaques (Busche et al., 2012; Busche et al., 2008; Grienberger et al., 2012). In the cortex, the emergence of hypo- and hyperactive cells coincided with the deposition of plaques. Notably, only hyperactive cells in V1 exhibited impaired function, as their visually evoked responses were less tuned (Grienberger et al., 2012). In hippocampus, however, hyperactivity is observed prior to plaque deposition. With the advent of plaque formation, neuronal hyperactivity is constrained to the plaque vicinity in hippocampus, too (Busche et al., 2012). These data point towards a critical role of soluble Aβ oligomers, which are prior to plaque deposition believed to be more or less evenly distributed within the parenchyma and to concentrate within and in the immediate surrounding of amyloid plaques, once these aggregates are formed. The mentioned studies were conducted in anesthetized mice. As during wakefulness the inhibitory drive in cortex is much higher compared to anesthetized conditions (Haider et al., 2013), it remains unclear, whether these disturbed neuronal activity patterns still persist during wakefulness and to what extent they affect neuronal response properties under these conditions.

2 OBJECTIVES

With this work I aimed at investigating cellular and subcellular mechanisms that underlie impaired information processing in AD. The thesis is divided into 2 main parts, in which I addressed the following key questions:

Project 1) Structural alterations of pre- and postsynaptic compartments in APP/PS1 transgenic mice:

Are dendritic spine/axonal bouton density and dynamics altered in APP/PS1 mice?

Are these alterations dependent on plaque proximity?

Can plaque-associated effects on structural compartments be halted/reversed by pharmacological interference with Aβ generation?

Project 2) Functional alterations of neurons in primary visual cortex of APP/PS1 transgenic mice:

Are response properties of neurons in V1 altered in APP/PS1 mice?

Is there evidence for aberrant neuronal activity in awake APP/PS1 mice?

Are potential functional changes cell type - specific?

In the following sections 3.1.-3.3. (page 32 – 61) I will outline the Methods and Results of the first project ("Structural alterations of pre- and postsynaptic compartments in APP/PS1 transgenic mice"), followed by the description of the Methods and Results of the second project ("Functional alterations of neurons in primary visual cortex of APP/PS1 transgenic mice") in sections 4.1.-4.3. (page 62 - 87). Both projects represent already published work (see (Liebscher et al., 2016; Liebscher et al., 2014)). A combined discussion of both projects will subsequently follow in section 5 (page 88 - 102).

3 PROJECT 1

Structural alterations of pre- and postsynaptic compartments in APP/PS1 transgenic mice

3.1. Abstract

Alzheimer's disease is believed to represent a disease of the synapse. The spatiotemporal dynamics of disease-associated synaptic alterations are not fully understood to date. In this study, I monitored dendritic spines, structural correlates of postsynapses, and axonal boutons, correlates of presynapses, over four weeks in the cortex of APP/PS1 transgenic mice using *in vivo* two - photon imaging. I differentiated between two populations of synaptic structures, those being in close proximity (50 μm) of amyloid plaques, the major hallmark of AD pathology, and those being further away and compared those to synaptic structures in non-transgenic siblings (WT mice). These experiments revealed a striking amyloid plaque- associated instability of synaptic structures that strongly outreached the area affected by spine loss. Treatment of transgenic animals with a novel selective γ-secretase inhibiter resulted in a slowing down of the growth of newly deposited amyloid plaques and normalized spine instability, without overt toxic effects on synaptic structures in WT mice. These data mark synaptic instability as a prominent and widespread feature of AD pathology and serve as a proof of principle for the efficacy of selective pharmacologic interference with Aβ generation.

3.2. Material & Methods

The following sections 3.2. and 3.3 (page 34 – 61) are taken from (Liebscher et al., 2014).

3.2.1. Animals

For chronic *in vivo* imaging experiments, APPPS1$^{+/-}$ transgenic mice (co-expressing APP containing the Swedish double mutation KM670/671NL and PS1 containing the L166P mutation under the Thy-1 promoter) (Radde et al., 2006) were crossbred with GFP-M$^{+/+}$ transgenic mice (expressing eGFP under the Thy-1 promoter, causing sparse labeling of mainly cortical layer V pyramidal neurons) (Feng et al., 2000). Animals were kept under a 12/12 hours light-dark cycle with food and water ad libitum and housed individually on standard cage bedding, without additional nesting material. All animal procedures followed a protocol approved by the local authorities (Regierung von Oberbayern). For imaging experiments, only male mice were used.

3.2.2. Drug administration

Male mice were treated with ELN594 (Elan Pharmaceuticals, South San Francisco, California, USA (see synthesis approach (Truong et al., 2009))) at the age of 3-4 months. The drug, dissolved in 2% methyl cellulose and 0.5% Tween20, was administered daily for four subsequent weeks via oral gavage at 30 mg/kg. All control mice received vehicle solution (2% methyl cellulose and 0.5% Tween20) only. Treatment started immediately after the first imaging session.

3.2.3. Characterization of ELN594 in cell based and cell free γ-secretase in vitro assays

The potency of ELN594 (Elan Pharmaceuticals, South San Francisco, California, USA) to reduce Aβ generation was evaluated in a cell assay as described previously (Basi et al., 2010). Briefly, CHO cells were stably transfected to express APPswe. ELN594 was added in fresh media over a range of concentrations for 4 h and subsequently Aβ levels in the media were determined by ELISA. To determine the potency of ELN594 in a cell-free system, our previously described γ-secretase in vitro assay was used (Winkler et al., 2009). In brief, γ-secretase was purified from HEK293 cells by our previously outlined procedure up to the lectin-affinity

chromatography step and then reconstituted into phosphatidylcholine vesicles (Winkler et al., 2009). Following addition of purified APP-based C-terminally hexahistidine-tagged γ-secretase substrate (C100-His_6) (Edbauer et al., 2003) as well as ELN594 at the indicated concentrations, assay samples were incubated at 37°C overnight. Thereafter, the generation of Aβ was analysed by immunoblotting (using antibody 6E10 (Signet Laboratories)).

3.2.4. Assessment of pharmacokinetics of the GSI ELN594 by liquid chromatography – mass spectrometry

Pharmacokinetic studies were conducted by Elan Pharmaceuticals (South San Francisco, California, USA) in accordance with the National Institutes of Health, Guide for the Care and Use of Laboratory Animals, and Institutional Animal Care and Use Committee. ELN594 was administered by a single oral gavage to nine week-old female FVB mice (Taconic, Germantown NY). ELN594 was formulated in 0.5% Tween 80 and 2% methyl cellulose in sterile water and administered at 30 mg/kg. Plasma (K_3-EDTA) and brain samples were collected from each mouse by destructive sampling at multiple time points post administration.

Plasma and brain concentrations of ELN594 were measured using a LC-MS/MS assay. Briefly, brain samples were homogenized (50 mM ammonium acetate, pH 7.4, 1:5 tissue to buffer) and subsequently plasma as well as brain homogenates were extracted using protein precipitation with acetonitrile containing an internal standard followed by centrifugation. The resulting supernatants were analysed by mass-spectrometry (PE-Sciex API-5500 Q-Trap mass spectrometer (AB Sciex, Foster City, CA), interfaced with an Agilent 1290 HPLC pump (Agilent, Santa Clara, CA) and a CTC-Pal autosampler (Zwingen, Switzerland)). Chromatography was facilitated with an ACE 3 C18 AR column (20 × 2 mm, 3 µm, Phenomenex) and eluted with a ballistic gradient of acetonitrile and 0.1% formic acid at 600 µl/min. ELN594 was detected by a multi-reaction-monitoring experiment in the positive ion mode with a TurboIon Spray interface. Results were calculated using peak area ratios of the analyte to the internal standard, and calibration curves were generated using weighted linear least-squares regression (1/X). Noncompartmental pharmacokinetic parameters were calculated using Phoenix™ WinNonlin® (Version 6.1, Pharsight Corporation, Mountain View, CA). Pharmacokinetic parameters, including maximal concentration (C_{max}), time of maximal concentration (t_{max}), area under the plasma concentration – time curve from time zero to infinity ($AUC_{(0-\infty)}$), half-life ($t_{1/2}$), clearance (CL), and volume of distribution (Vdss) were calculated as described previously (Gibaldi, 1982).

The absolute bioavailability (%F) was calculated as the ratio of the mean oral $AUC_{(0-\infty)}$ treatment divided by the mean IV reference $AUC_{(0-\infty)}$. Brain penetration (Kp) was assessed from the ratio of brain exposure to plasma exposure.

3.2.5. Western blot analysis of APP-CTFs and ELISA detection of Aβ1-x in APPPS1 mouse brains

In order to demonstrate the efficacy of the GSI ELN594 in the APPPS1 mouse model we administered a single dose of the drug at a concentration of 30 mg/kg via oral gavage to male APPPS1 mice (age 4-5 months). Animals were sacrificed 24 hours post GSI administration, brains removed and snap frozen on dry ice. Following homogenization of half brains in 1 ml carbonate buffer (100 mM Na_2CO_3, 50 mM NaCl, pH 11.5, protease inhibitors), aliquots of the homogenates were analysed for APP and APP C-terminal fragments (APP-CTFs) by direct immunoblotting, using polyclonal antibody 6687 against the APP C-terminus (Steiner et al., 2000). Aβ was detected by ELISA. Briefly, brain homogenates were subjected to centrifugation (20,000 × g, 30 min, 4°C). Soluble Aβ was extracted from the supernatant with an equal volume of guanidinium buffer 1 (8.2 M guanidinium HCl, 82 mM Tris HCl) and insoluble Aβ by extraction of the pellet for 3 h at RT with 1 ml of guanidinium buffer 2 (5 M guanidinium HCl, 50 mM Tris HCl). Following centrifugation (20,000 × g, 30 min, 4°C), supernatants were diluted 1:1000 in block buffer (1% BSA, 0.1% Tween in PBS) and soluble Aβ species were quantified by a sandwich immunoassay using an ECL detection system (Meso Scale Discovery, MSD). Samples and Aβ peptide standards (MSD) were added together with ruthenylated 6E10 detection antibody (1 μg/ml) in 96-well Multi-SPOT plates, pre-coated with anti-Aβ40 or anti-Aβ42 antibodies and incubated for 2 hours. The light emission at 620 nm after electrochemical stimulation was measured using the MSD Sector Imager 2400 reader, and the corresponding concentrations of Aβ peptides were calculated using the MSD Discovery Workbench software (Page et al., 2010).

3.2.6. Cranial window surgery

Male $APPPS1^{+/-}$- $GFP^{+/-}$ mice (referred to as APPPS1) and non APPPS1 transgenic - $GFP^{+/-}$ littermates (referred to as wild-type here, WT) were implanted with a cranial window at the age of 2-3 months, as previously described (Holtmaat et al., 2009; Spires et al., 2005), above the parietal cortex (coordinates of craniotomy: Bregma +1.5 – -3.5 mm, 3 mm lateral from midline on each side; position of imaging regions

within cranial window are shown in Figure 23) under combined Midazolam (0.05 mg/kg Dormicum, Roche), Fentanyl (5.0 mg/kg Hexal), Medetomidin (0.5 mg/kg Dormitor, Orion Pharma) anesthesia. Briefly, a circular craniotomy (coordinates: Bregma +1.5 – -3.5 mm, 3 mm lateral from midline on each side) was performed, and a round glass coverslip (8 mm diameter) was placed on top of it and fixed with gel glue in order to close the craniotomy. A small metal head bar was glued next to the coverslip to allow repositioning of the mouse during subsequent imaging sessions. Further stabilization of the window was achieved by adding dental acrylic (Paladur, Heraeus Kulzer GmbH). In all mice, irrespective of treatment group assignment, imaging only started four weeks post window implantation to allow for stabilization of the preparation (Holtmaat et al., 2009).

3.2.7. *In vivo* two - photon microscopy

Mice were imaged once a week for four consecutive weeks under Midazolam/Fentanyl/Medetomidin anesthesia using a custom-built two-photon microscope with a mode-locked Ti:sapphire laser (Mai Tai, Spectra-Physics), equipped with a 40× water immersion objective (0.8 NA, Olympus). To label plaques, animals were injected intraperitoneally (i.p.) with Methoxy-XO4 (Neuroptix Corporation) at a concentration of 3.33 mg/kg (3.3% vol of 10 mg/ml stock solution in DMSO (light shielded), 6.66% vol Cremophore EL (Sigma Aldrich) in 90% vol PBS (Klunk et al., 2002)) 24 hours prior to each imaging session. GFP and Methoxy-XO4 were simultaneously excited at either 830 nm (overview stacks) or 880 nm (high resolution stacks). A 480 nm dichroic mirror (480 DCXR, AHF Analysentechnik) was used to separate emission from both fluorophores. Care was taken to not exceed 50 mW maximum power delivered to the brain. The overview z-stacks used to assess the deposition of new plaques were 350×350×300 µm (xyz) in size with 5 µm z-increments and 512×512 pixel resolution, whereas the high resolution z-stacks used for spine and bouton analysis measured 130×130×30-100 µm (xyz) with z-increments of 0.5 µm and 1024×1024 pixel resolution. Image acquisition was based on custom software programmed in Labview (National Instruments). The first imaging session was carried out immediately before GSI treatment commenced.

3.2.8. Image processing and data analysis

Analysis of images was performed using ImageJ software (http://rsbweb.nih.gov/ij/) in raw z-stacks by manually scrolling through respective frames and marking counted structures (e.g. newly deposited plaques,

dendritic spines, or axonal boutons). The emergence of new plaques was analysed in the blue fluorescence channel corresponding to the Methoxy-XO4 signal, in a standardized region of interest (ROI) of 350×350×285 µm.

Size (area in µm²) of newly deposited plaques was measured in maximum projections of all frames bearing the new plaque. Maximum projections were background subtracted and the detection stringency was set to the mean + 1.5× standard deviation of the background. Dendritic spines and axonal boutons were scored and counted in the green fluorescence channel. Apical dendritic tufts of pyramidal neurons in layer V and axonal stretches of putative layer II/III/V neurons were imaged within layer I (10-100 µm below the dura). Dendritic and axonal segments were of 30-150 µm length. In some imaging regions, more than one dendritic stretch per neuron was analysed. To ascertain that stretches from the same cell could be treated as independent samples, we computed the correlations between stretches from one neuron and those originating from different neurons within the same animal for the parameters spine density, survival fraction and turnover rate, and found no significant differences (Table 1).

	APPPS1			**WT**		
parameter	**intraneuronal r^2**	**interneuronal r^2**	***P***	**intraneuronal r^2**	**interneuronal r^2**	***P***
spine density	0.3 ± 0.06	0.37 ± 0.03	0.12	0.34 ± 0.13	0.26 ± 0.04	0.61
survival fraction	0.81 ± 0.03	0.82 ± 0.02	0.83	0.91 ± 0.02	0.89 ± 0.01	0.81
turnover rate	0.3 ± 0.06	0.33 ± 0.03	0.17	0.41 ± 0.16	0.33 ± 0.05	0.44

Table 1: Intraneuronal correlations are not different from interneuronal correlations.
Coefficients of determination (r2) between dendritic stretches belonging to the same neuron were compared to the coefficients of determination of dendrites belonging to different neurons for the parameters spine density, survival fraction and turnover rate. Both in APPPS1 and in WT mice intraneuronal and interneuronal correlations do not significantly differ from one another. Values are mean ± SEM and P values were derived from Mann-Whitney tests. Reprint from Molecular Psychiatry with permission from Nature Publishing Group (Liebscher et al., 2014).

Dendritic spines were counted if clearly emanating laterally from the dendrite. Spines projecting in z-direction were excluded from the analysis. Detection stringency for axonal boutons was set to a fluorescence intensity of at least three times than that of the axonal backbone (De Paola et al., 2006). A bouton crossing this threshold was deemed lost or gained.

Spine and bouton parameters were computed as follows: the survival fraction (SF) corresponds to the fraction of still-existing spines/boutons at each imaging time point with respect to the initial time point: SF (t) = n (t)/n_0, with n_0 being the number of spines/boutons at time point 0 and n(t) the number of spines/boutons of the initial population (time point 0) still present at time point (t). Turnover rate (TOR) measures the appearance and disappearance of spines/boutons between two subsequent time points and is calculated as: TOR (t_1, t_2) = (n_{gain}+n_{loss})/(n(t_1)+ n(t_2)), with n(t_1) and n(t_2) being the number of structures present at time point 1 and 2, respectively (Holtmaat et al., 2009). Presented here is the mean TOR over all time points.

Spines and boutons were further divided into categories referring to their lifetime: persistent spines/boutons (ps/pb) were present at every time point; persistent spines/boutons lost (psl/pbl) were present at least during the first three imaging sessions and lost afterwards; persistent spines/boutons gained (psg/pbg) were not present at the initial imaging time point, but were at least present during the last 3 imaging sessions, and transient spines/boutons (ts/tb) were not present at the first and last imaging time point, but appeared and subsequently disappeared during the course of the experiment. Note that this categorization does not sum up to one, as a fraction of spines was not assigned to any of the above-mentioned subgroups. In APPPS1 mice, spine and bouton analyses were performed separately on two groups of stretches of neurites: dendrites or axons located further than 50 µm away from the next plaque (usually situated in a "plaque free" region; referred to as "distant"), and dendrites or axons passing by a plaque (having a minimal diameter of 10 µm) with the shortest distance between neurite and plaque below 20 µm (referred to as "near"). In the latter category, spines and boutons were analysed within a radius of 50 µm to the plaque border. Plaque detection stringency was set to mean + 3 x standard deviation of the image.

For determination of plaque distance-dependent spine density and turnover rate, dendrites were subdivided into almost equally long parts (each ~17µm length), starting from the closest segment to the plaque. The distance to the plaque border of each segment represents the average distance of both segment endpoints. Inter-bouton distance reflects the distance along the axon between 2 neighbouring boutons. The distance of the corresponding axonal stretch to the plaque is set as the average of the distances of both boutons and the center of the axonal stretch between them to the respective plaque.

Integrated spine brightness was used as a measure for spine volume: In the best focal section, after subtraction of the background (measured next to the spine in an area devoid of any fluorescence signal), pixel intensities of all pixels comprising the spine were summed up and this integral divided by the average pixel intensity of

the neighbouring dendritic shaft (Hofer et al., 2009; Holtmaat et al., 2005). Only spines clearly emanating laterally at all time points were included into this analyses.

Altogether, we analysed 16 dendrites with a total length of 1279 µm in 4 WT vehicle treated mice, 19 dendrites (total length 1601 µm) in 7 WT GSI treated mice, 21 dendrites distant from plaques (total length 1713 µm) and 12 dendrites near plaques (total length 759 µm) in 5 APPPS1 vehicle treated mice as well as 32 dendrites distant from plaques (total length 2711 µm) and 15 dendrites near plaques (total length 1111 µm) in 7 APPPS1 GSI treated mice. In total, 12423 spines were counted, including those lost and gained. Numbers of analysed axonal stretches were as follows: 17 axons (total length 1393 µm) in 4 WT vehicle treated mice, 13 axons (total length 1029 µm) in 5 WT GSI treated mice, 14 axons distant from plaques (total length 806 µm) and 13 axons near plaques (total length 721 µm) in 4 APPPS1 vehicle treated mice as well as 18 axons distant from plaques (total length 1053 µm) and 30 axons near plaques (total length 2069 µm) in 7 APPPS1 GSI treated mice. Altogether 4063 boutons were counted.
Image acquisition and analysis was conducted in a blinded manner.

3.2.9. Statistics

Statistical analyses were performed using GraphPad Prism (GraphPad Software, Inc) and Matlab (Mathworks, Inc.). Normally distributed data was tested either by student's t-test, one-way ANOVA or repeated measures ANOVA. Unless stated otherwise Tukey-Kramer tests were deployed for post-hoc comparisons. Non-normally distributed data were tested either by Mann-Whitney, Kruskal-Wallis or Friedman's test. Post-hoc comparisons were done using Dunn's post-hoc test. Reported values are means ± SEM. Significance level α was set to 0.05.

3.3. Results

In order to characterize the impact of amyloid plaque pathology on the dynamics of synaptic structures *in vivo,* we performed longitudinal *in vivo* two-photon imaging in male WT and APPPS1 mice (Figure 7). We then assessed whether pharmacological interference with Aβ generation exerts beneficial effects on plaque-associated synaptic pathology in APPPS1 mice. To this end, we administered the selective GSI, ELN594, daily (30 mg/kg), for four consecutive weeks to WT and APPPS1 mice at the age of 3-4 months and monitored amyloid pathology, dendritic spines and axonal boutons *in vivo* throughout the treatment period.

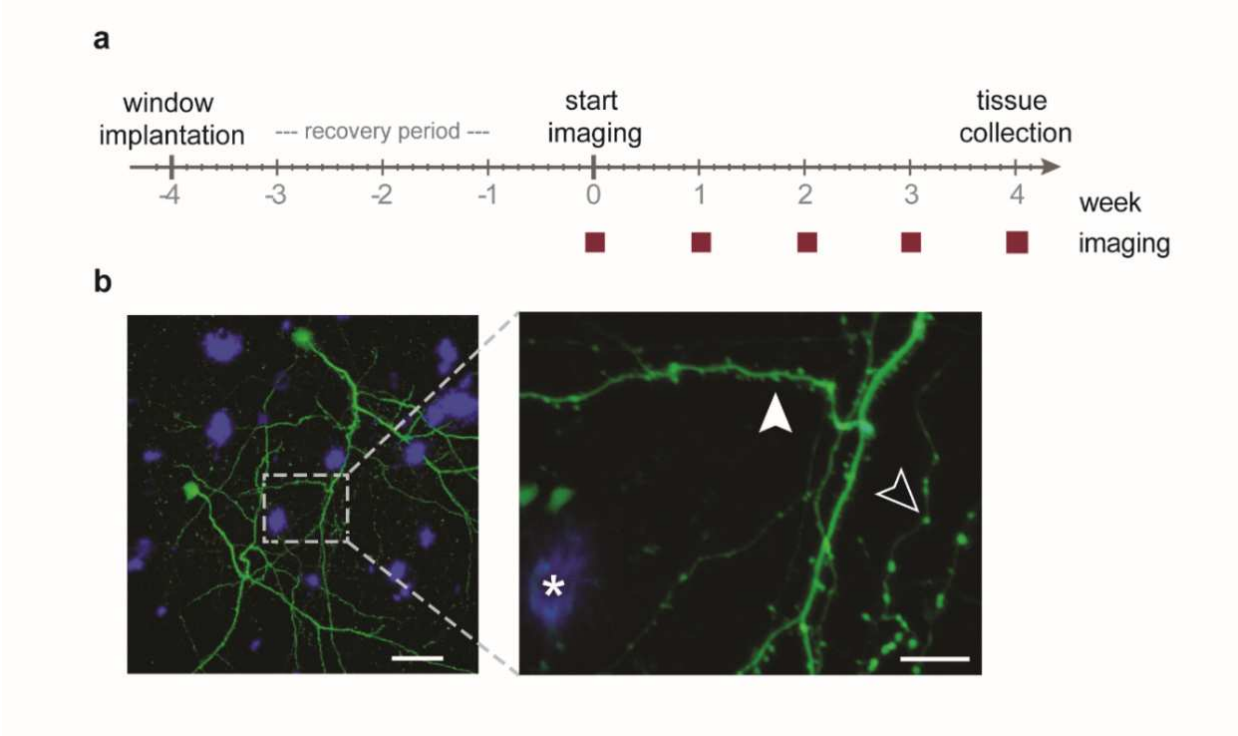

Figure 7: Chronic in vivo imaging of neurites and amyloid plaques.
(a) Time course; note that imaging only started four weeks post-implantation. (b) Representative example of an overview stack, shown as a maximum projection of 90 optical sections, spaced by 5 µm (450 µm in total). The insert depicts examples of structures analysed, such as amyloid plaques (asterisk), dendritic spines (filled arrowhead) and axonal boutons (open arrowhead) at a higher magnification. Scale bars 50 µm (a), 10 µm (b). Reprint from Molecular Psychiatry with permission from Nature Publishing Group (Liebscher et al., 2014).

3.3.1. Amyloid plaque - associated spine pathology

Since there is accumulating evidence that plaques cause neuritic and spine pathology predominantly within 50 µm distance to plaques (Bittner et al., 2012; Grutzendler et al., 2007; Kuchibhotla et al., 2008; Meyer-Luehmann et al., 2008; Spires-Jones et al., 2007; Tsai et al., 2004), we analysed dendritic spines on apical tufts of layer V pyramidal neurons in WT (Figure 8a) and APPPS1 mice in the immediate vicinity of plaques (< 50 µm, "near"; Figure 8b) and further away (> 50 µm, "distant").

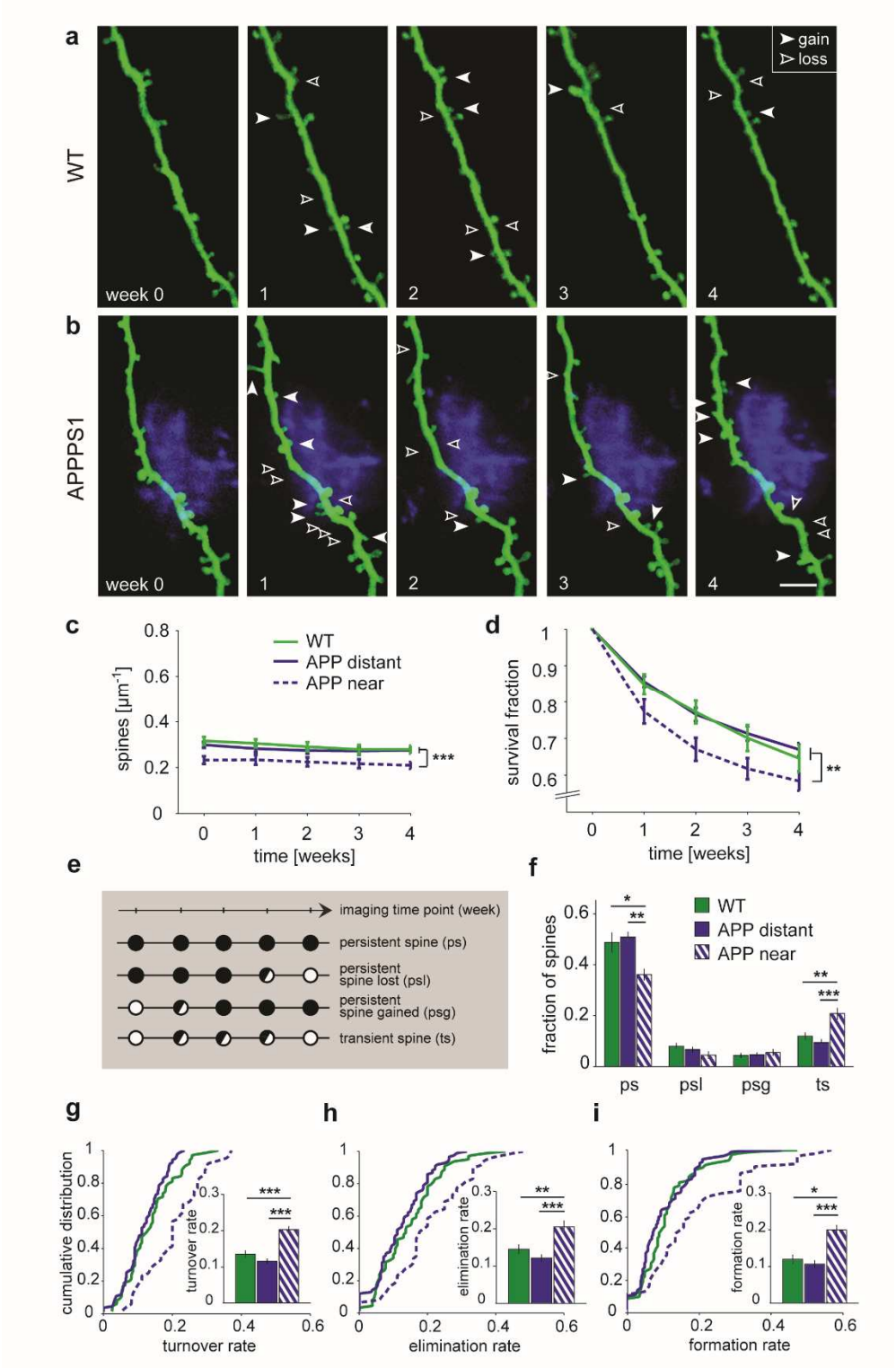

Figure 8.
Figure legend see next page.

Figure 8: Amyloid plaque-associated dendritic spine alterations.
*(a,b) Representative examples of apical dendritic stretches of layer V pyramidal neurons repeatedly imaged within layer I over the course of four weeks in WT and APPPS1 mice (shown are maximum projections). Note that the actual position of the dendritic stretch in (b) is just above the plaque, with the dendrite not passing through it. (c) Spine density is significantly lower in the vicinity of plaques in APPPS1 mice, compared with dendrites further away from plaques and WT mice, respectively (repeated measures ANOVA; $P < 0.001$ and $P < 0.001$). (d) Survival fraction of spines near plaques is significantly decreased (repeated measures ANOVA, $P < 0.001$). (e) Classification of spines with respect to their life time. Filled circles denote the presence of a spine at the respective time point, open circles correspond to the absence of a spine and half-filled circles denote a spine being either present or absent at the respective time point. (f) Dendrites near plaques have fewer persistent (one-way ANOVA, $P < 0.01$ and $P < 0.05$) and more transient spines compared with spines distant from plaques and in WT mice (one-way ANOVA, $P < 0.001$ and $P < 0.01$). (g) Spine turnover rates near plaques are significantly elevated compared with spines further away from plaques and WT mice, respectively (one-way ANOVA, $P < 0.001$). (h, i) Increased turnover results from higher (h) elimination - (one-way ANOVA, $P < 0.001$ and $P < 0.01$) and (i) formation rates (Kruskal-Wallis, $P < 0.001$ and $P < 0.05$). Data in (g-i) are average values over all imaging time points. WT: n = 16 dendrites (4 mice); APP distant: n = 21 dendrites (5 mice); APP near: n = 12 dendrites (5 mice). Values are mean ± SEM, Scale bar 5 µm (b), * $P < 0.05$, ** $P < 0.01$, *** $P < 0.001$. Reprint from Molecular Psychiatry with permission from Nature Publishing Group (Liebscher et al., 2014).*

As described before (Bittner et al., 2012; Spires et al., 2005; Tsai et al., 2004) (for review see (Liebscher and Meyer-Luehmann, 2012)), we found that dendritic stretches within the immediate vicinity of amyloid plaques exhibited a lower spine density (average over all time points 0.22 ± 0.017 μm^{-1}) compared with stretches further away from plaques in APPPS1 (0.28 ± 0.013 μm^{-1}) and WT mice (0.29 ± 0.017 μm^{-1}, Figure 8c). A more detailed analysis revealed that spine density was significantly reduced up to 15µm from the plaque border compared with the spine density of WT vehicle treated mice (Spires et al., 2005; Tsai et al., 2004) (Figure 9a) and that spine density was positively correlated with plaque distance up to 50µm away from the plaque border (Pearson's correlation coefficient r = 0.23, $P = 0.01$).

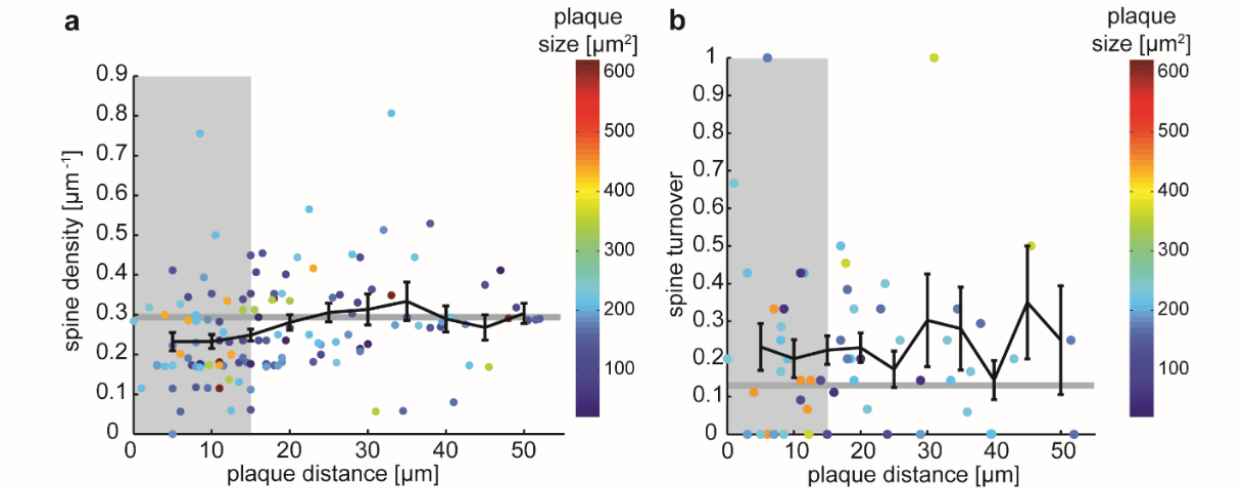

Figure 9: Effect of plaque distance and size on dendritic spines.
(a) In order to yield a higher resolution of the effect of plaque distance, dendritic stretches were subdivided into equally long segments, and the respective average distance of the segment to the plaque was measured. Spine density is significantly reduced (light grey box, P < 0.05) compared with stretches from WT vehicle treated mice (0.29 ± 0.017µm^{-1}, mean is denoted as dark grey line) up to 15µm away from the plaque border (0-5µm: P = 0.02; 5-10µm: P = 0.03; 10-15µm: P = 0.009; Mann-Whitney test). Presented is the spine density at the first imaging time point (pre-treatment) of both the vehicle and the GSI treated group as a function of distance to the plaque border. Spine density is positively correlated with plaque distance between 0-50 µm away from the plaque border (r = 0.23, P = 0.01). Spine density is not correlated with the size of the respective plaque (shown in color-code, r = - 0.05, P = 0.56). The black line denotes a sliding average encompassing a 10µm window with 5µm increments (values are mean ± SEM). (b) Increased spine turnover near plaques is independent of distance within 0-50 µm from the plaque border (r = 0.04, P = 0.79) and plaque size (r = -0.09, P = 0.51). Data presents turnover between week 0 and 1 of vehicle treated APPPS1 mice and is referenced to the average turnover observed in WT mice (0.13 ± 0.016, mean is denoted as dark grey line). Grey region indicates the plaque distance, where a significant reduction of spine density was observed (see panel (a)). Spine density: in total 136 segments combining data from APP near vehicle: 61 segments (12 dendrites, 5 mice) and APP near GSI: 75 segments (15 dendrites, 7 mice). Turnover rate: APP near vehicle: 61 segments (12 dendrites, 5 mice). Reprint from Molecular Psychiatry with permission from Nature Publishing Group (Liebscher et al., 2014).

The drop in spine density near plaques did not depend on plaque size (r = - 0.05, P = 0.56; Figure 9a). Determining spine density alone is insufficient to capture all aspects of potential (pathological) spine alterations, as they are dynamic structures, which are lost and gained at a certain rate, even under baseline conditions (Hofer et al., 2009; Holtmaat et al., 2005; Pan et al., 2010; Trachtenberg et al., 2002). We hence determined the spine survival fraction and turnover rate and classified spines, according to their lifetime, as persistent or transient (Figure 8e). Spines close to plaques are less stable, which is reflected in a lower survival fraction (Figure 8d), a lower fraction of persistent spines compared with spines distant from plaques and in WT mice (Figure 8f) and, accordingly, a higher fraction of transient spines (Figure 8f). The high turnover rate

of spines near plaques (Figure 8g) resulted from both an increased elimination - (Figure 8h) and formation rate (Figure 8i). The elevated spine turnover did neither depend on plaque proximity within a 0-50 µm radius to the plaque border (r = 0.04, P = 0.79) nor on plaque size (r = -0.09, P = 0.51, Figure 9b).

There was no significant difference between spines in WT mice and spines further away from plaques in APPPS1 mice for any of the spine parameters analysed. A more detailed analysis, however, revealed a negative correlation between turnover rate and spine density in WT mice, in line with a previous publication (Holtmaat et al., 2005). Interestingly, this correlation was inverted (i.e. positive) for dendrites further away from plaques in APPPS1 mice (WT: r = -0.52, P = 0.039; APPPS1: r = 0.47, P = 0.025; Figure 10a). This difference was largely due to dendritic stretches with a low spine density (0.15 – 0.26/µm), which exhibited a significantly lower spine turnover rate in APPPS1 mice (Figure 10b). The absolute density of gained spines was independent of the total spine density in WT mice (r = 0.-011, P = 0.97, Figure 10c). In contrast, in APPPS1 mice, dendrites distant from plaques exhibited a significant positive correlation between the density of gained spines and total spine density (r = 0.73, P < 0.001, Figure 10c). Again, low density dendrites (<= 0.26/µm) in APPPS1 mice had a significantly lower density of newly formed spines in comparison to WT mice (Figure 10d). These data indicate a plaque-independent effect on spine dynamics in APPPS1 transgenic mice, which mainly affects dendritic stretches with a low spine density. We did not observe a significant correlation between spine density and turnover rate for spines close to plaques (r = -0.47, P = 0.12).

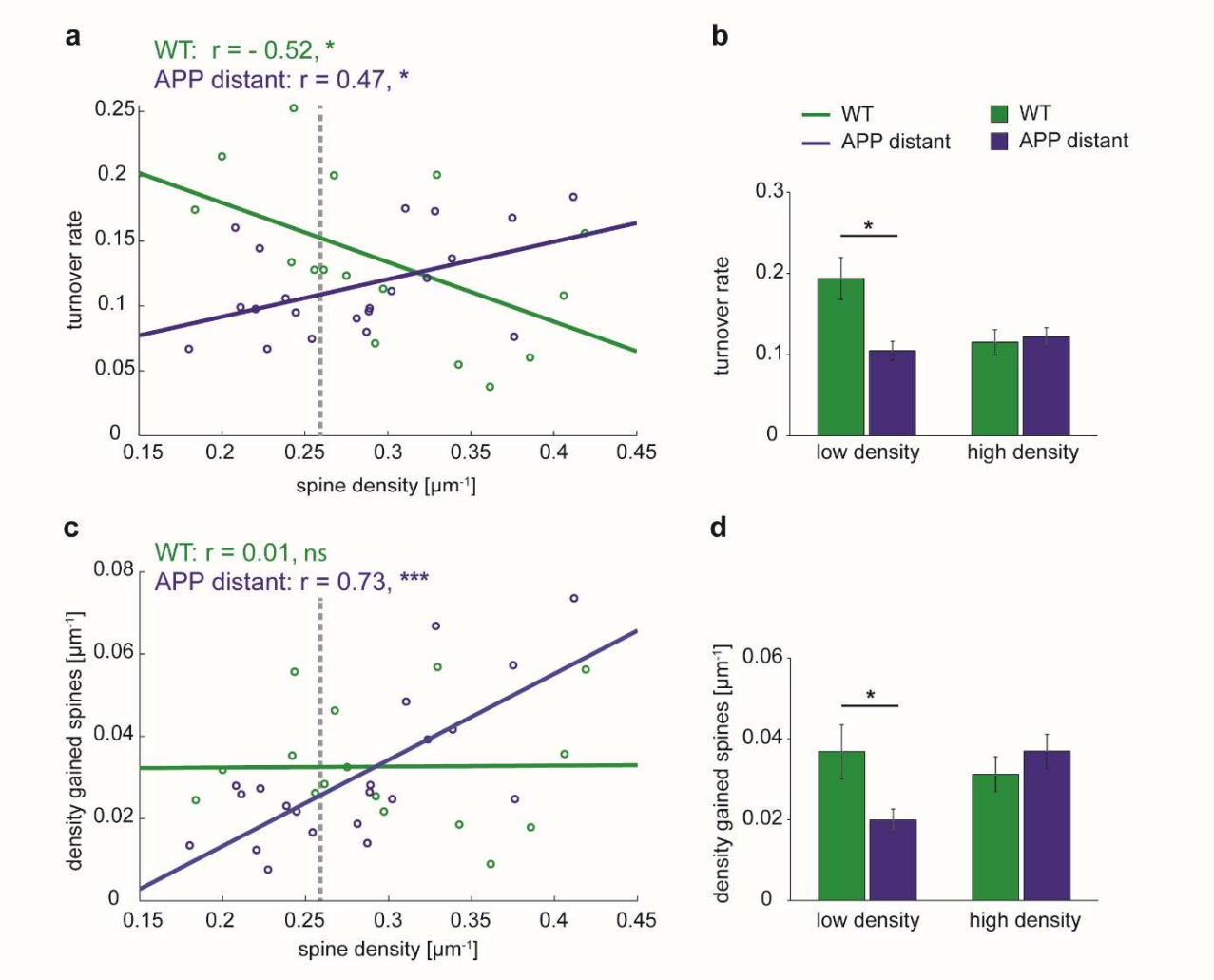

Figure 10: Amyloid plaque - independent effects on dendritic spines.

*(a) Spine density is negatively correlated with turnover rate in WT mice (linear fit f(x) = -0.46x + 0.27, r = -0.52, P = 0.039). For spines distant from plaques in APPPS1 mice this correlation is reversed (f(x) = 0.29x + 0.034, r = 0.47, P = 0.025). (b) Separate analysis of low (<= 0.26/µm, denoted by dashed grey line in Figure 3a) and high spine density stretches (> 0.26/µm) reveals a significant reduction of turnover rate on low density dendrites in APPPS1 compared with WT mice (Mann-Whitney test, P = 0.012). (c) The density of gained spines is independent of total spine density in WT mice (f(x) = -0.002x + 0.03, r = 0.-011, P = 0.97). In APPPS1 mice the density of newly formed spines is positively correlated with total spine density (f(x) = 0.21x – 0.029, r = 0.73, P < 0.001). (d) Comparison of average density of gained spines shows a significant difference between WT and APPPS1 mice only for low density stretches (Mann-Whitney test, P = 0.019). WT: n = 16 dendrites (4 mice); APP distant: n = 21 dendrites (5 mice); Values are mean ± SEM. * P < 0.05, *** P < 0.001. Reprint from Molecular Psychiatry with permission from Nature Publishing Group (Liebscher et al., 2014).*

3.3.2. Amyloid plaque - associated axonal bouton pathology

Not much is known about the dynamics of plaque-associated presynaptic structures. We therefore analysed axonal boutons located within the same imaged volumes as the above described dendrites. We took advantage of the fact that bouton dynamics were described in detail for the GFP-M mouse line in a recent publication (De Paola et al., 2006). Based on this study and judged by bouton size as well as the number and length of axonal branches, the majority of axons investigated are putatively originating from layer II/III/V cells (Figure 12a,b). In addition to en passant boutons, which represented the majority of boutons, terminaux boutons were included in the analyses, as their fraction was low and did not differ significantly between groups (fraction terminaux boutons: WT 0.04 ± 0.065, APP distant 0.09 ± 0.12, APP near 0.076 ± 0.1, Kruskal-Wallis, $P = 0.45$).

We did not find a significant difference in bouton density between WT and APPPS1 mice (WT 0.12 ± 0.01/µm, APP distant 0.12 ± 0.01/µm, APP near 0.13 ± 0.013/µm, Figure 12c). Furthermore, on axonal stretches close to plaques the inter-bouton distance did also not depend on plaque proximity (Figure 11).

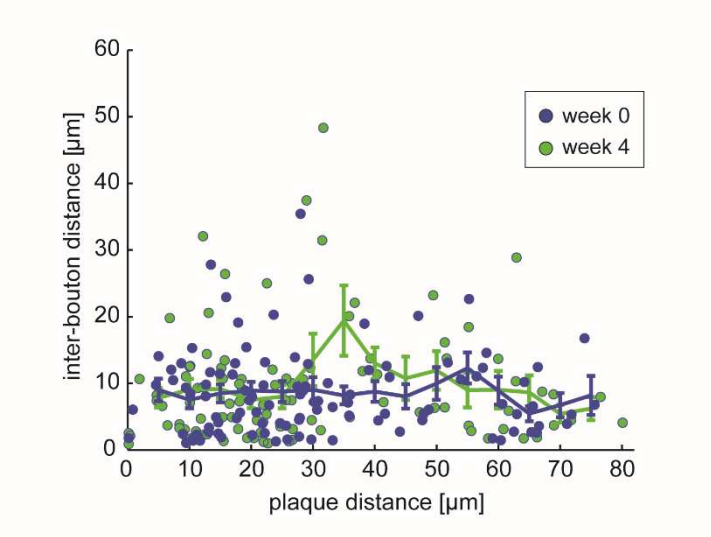

Figure 11: Inter-bouton distance close to plaques.
Inter-bouton distance as a function of distance to the plaque border at the first (blue circles) and last imaging time point (green circles) of vehicle treated APP mice. Lines are sliding averages encompassing a 10µm window moving in 5µm steps. Inter-bouton distance does not correlate with plaque distance (week 0: 104 boutons, r = 0.004, P = 0.97; week 4: 99 boutons, r = 0.048, P = 0.63; Values are mean ± SEM).

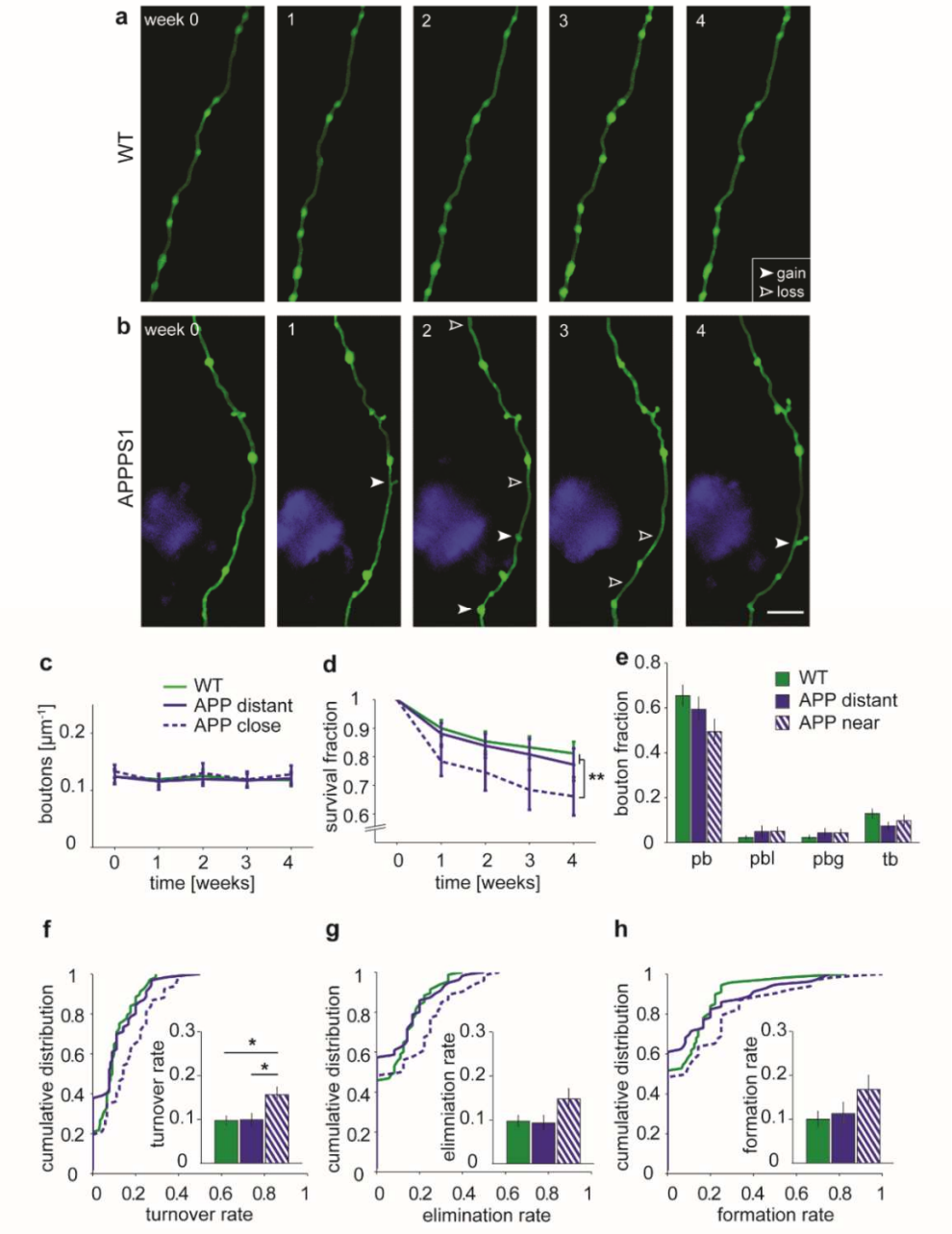

Figure 12: Bouton dynamics in WT and APPPS1 mice.

*(a) Examples of axonal stretches in (a) WT and (b) APPPS1 mice over the four-week imaging period are shown as maximum projections. Boutons lost from one time point to the next are marked with open arrowheads, boutons gained with filled arrowheads. (c) Bouton density is not different between axons near plaques, further away from plaques or in WT mice (repeated measures ANOVA, P = 0.93). (d) Boutons near plaques exhibit a lower survival fraction (repeated measures ANOVA, P < 0.01). (e) Bouton life time categories (see Figure 7e) do not differ significantly among groups (fraction persistent boutons: one-way ANOVA, P = 0.12, fraction transient: Kruskal - Wallis P = 0.31, fraction persistent lost: Kruskal - Wallis P = 0.63, fraction persistent gained: Kruskal - Wallis P = 0.61). (f) Turnover rate is increased on boutons close to plaques (Kruskal - Wallis, P < 0.05). Separate analysis of (g) elimination - and (h) formation rate showed the same trend, but did not reach significance (Kruskal -Wallis, P = 0.23 and P = 0.24). WT: n = 17 axons (4 mice); APP distant: n = 14 axons (4 mice); APP near: n = 13 axons (4 mice). Values are mean ± SEM, Scale bar 10 µm (b), * P < 0.05, ** P < 0.01. Reprint from Molecular Psychiatry with permission from Nature Publishing Group (Liebscher et al., 2014).*

However, similar to our data on dendritic spines near plaques, the survival fraction of boutons near plaques was decreased compared with boutons further away from plaques and in WT mice (Figure 12d). Analysis of boutons with different lifetimes did not yield a significant difference between axons in APPPS1 and WT mice (Figure 12e). Yet, boutons near plaques exhibited a higher turnover rate compared with boutons further away from plaques and boutons in WT mice (Figure 12f). Separate analyses of elimination and formation rate showed the same trend, but did not reach significance (Figure 12g,h). Overall, boutons appeared less dynamic than spines on apical tufts of layer V neurons, corroborating earlier reports (De Paola et al., 2006; Holtmaat et al., 2005). Newly formed spines have been shown to preferentially target large multisynaptic boutons (Knott et al., 2006), which could account for the observed difference.

Apart from the above mentioned changes in bouton dynamics, we occasionally observed the emergence of axonal dystrophies, axonal breakage and axonal sprouting within the peri-plaque region (Figure 13). These structural alterations occurred only rarely in APPPS1-GFP mice, probably attributable to the young age of 3-4 months and the sparse labeling of neurons in the GFP-M mouse line.

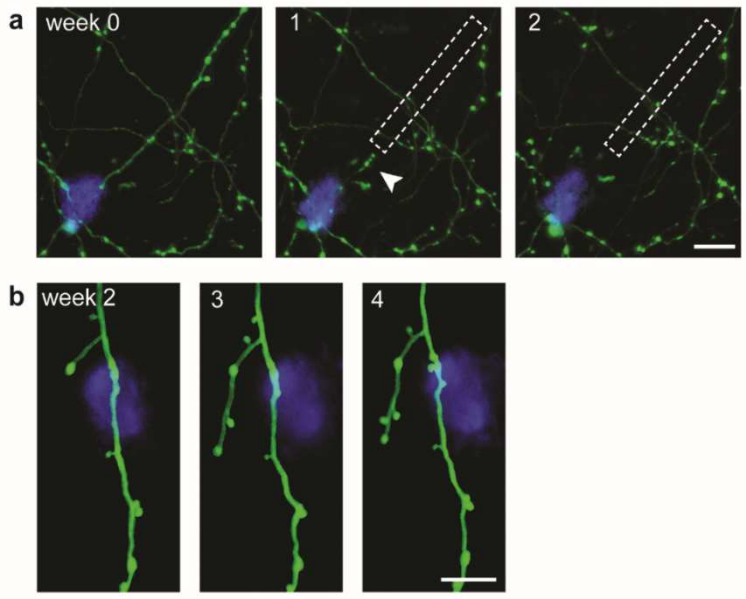

Figure 13: Amyloid plaque-associated axonal pathologies.
(a) Example of plaque-associated axonal breakage. Dashed box denotes the previous position of the axon distal to the plaque. Breakage progressed in a stepwise fashion, such that after the first week breakage occurred about 20 µm away from the plaque border, leaving an axonal stub (marked by white arrowhead). At the consecutive imaging time point this stub was further shortened, thereby ending within the amyloid plaque. (b) Example of axonal sprouting. A branch of a putative thalamocortical axon exhibits a strong elongation. Note that the axon is situated right above the amyloid plaque and is not passing through it. Scale bar (a) 20 µm and (b) 10 µm. Reprint from Molecular Psychiatry with permission from Nature Publishing Group (Liebscher et al., 2014)

3.3.3. Initial reduction of *de novo* plaque deposition by GSI treatment

We investigated whether the enhanced dynamics of synaptic structures near amyloid plaques can be halted by Aβ-targeting treatment. For this purpose, we tested the sulfonamide type γ-secretase inhibitor ELN594 both in WT and APPPS1 mice. ELN594, a sulfonamide type γ-secretase inhibitor, inhibits 50% of the APP cleavage (EC_{50}) at an effective concentration of 0.51 nM in a cell based assay and of 9.4 nM in a cell free assay (Figure 14a). Pharmacokinetic analysis of ELN594 in FVB wild-type mice suggested low systemic clearance (1.62 l/h/kg), moderate volume of distribution (2.29 l/kg), good oral bioavailability (45%) and CNS penetration (Davies and Morris, 1993). ELN594 was rapidly absorbed in FVB mice following oral administration of 30 mg/kg with a t_{max} of 0.5 hour and a brain to plasma partition (Kp) ratio of 1.2 (Figure 14b). Plasma and brain concentration - time profiles demonstrated that the remaining total drug concentrations 24 hours following single administration of ELN594 at 30 mg/kg were well above the EC_{50} for APP cleavage (0.51 nM) (Figure 14c).

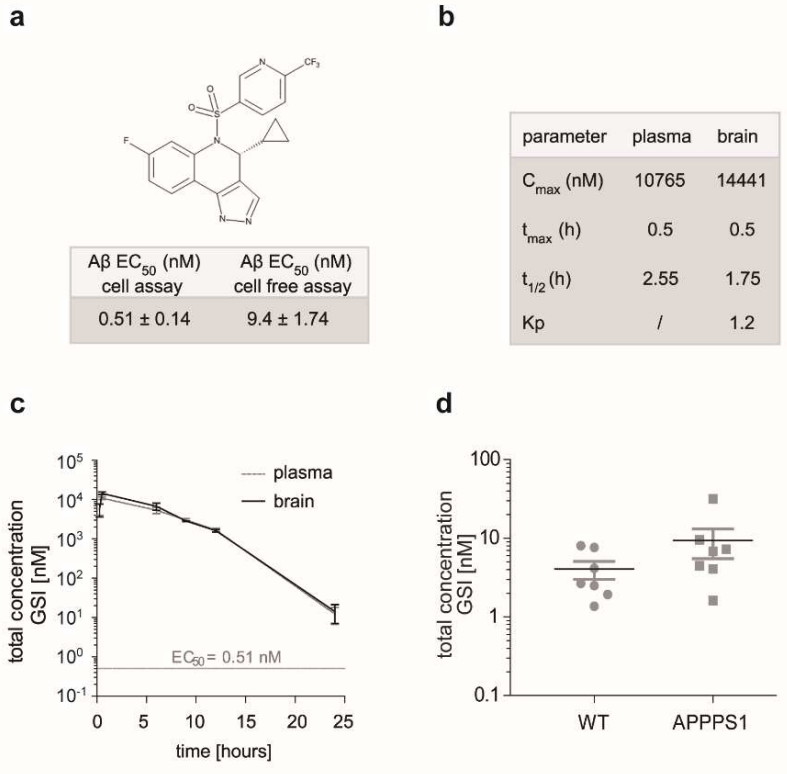

Figure 14: Pharmacodynamic - and pharmacokinetic properties of ELN594.

(a) Structural formula of ELN594 and EC_{50} values for Aβ generation obtained in a cell based - and in a cell free assay. (b) Pharmacokinetic properties of ELN594 assessed in FVB mice in plasma and brain samples after a single oral administration of ELN594 at 30 mg/kg (n=33 mice). (c) Time – concentration profile of ELN594 in plasma and brain of FVB mice after a single oral dose (30 mg/kg), referenced with EC_{50} for Aβ generation. 24 hours after administration the total drug concentration in plasma and brain was well above the EC_{50}. (d) Total ELN594 concentration in brains of WT and APPPS1 mice does not differ 24 hours after last drug administration upon 4 weeks of daily treatment. Abbreviations: C_{max} = maximal concentration; EC_{50} = half maximal effective concentration; Kp = partition coefficient, reflecting brain to plasma concentration ratio; t_{max} = time of maximal concentration. Reprint from Molecular Psychiatry with permission from Nature Publishing Group (Liebscher et al., 2014).

Since PS1 mutations of familial AD, such as the aggressive PS1 L166P mutation (Moehlmann et al., 2002) present in the mouse model used here, are known to be less sensitive to GSIs (Czirr et al., 2007), we first tested the effect of a single dose of ELN594 (30 mg/kg) on APP C-terminal fragments (APP-CTFs) as well as Aβ40 and Aβ42 levels in brains of APPPS1-GFP mice 24 hours after drug application. The GSI efficiently inhibited γ-secretase as shown by the pronounced accumulation of APP-CTFs in Western blot analysis (219 % compared with vehicle treated animals, Figure 15a,b).

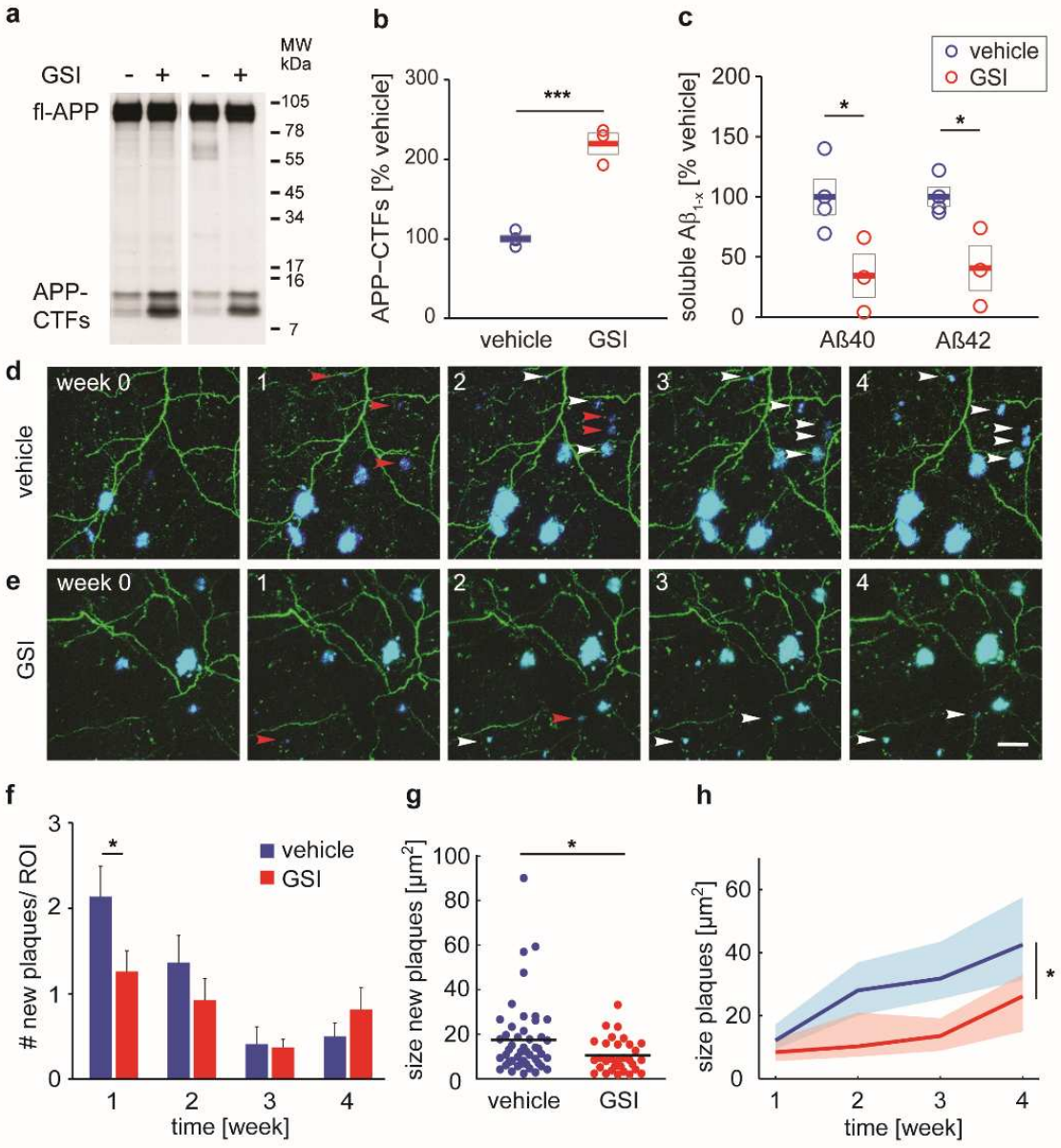

Figure 15. Figure legend see next page.

Figure 15: GSI treatment reduces Aß generation in vivo and attenuates the deposition and growth of new plaques in APPPS1 mice.

*(a) Representative Western blot analysis of the effect of GSI application on fl-APP and APP-CTF levels in APPPS1 brain homogenates (blots of two different experiments are shown). (b) Quantification of GSI effect on APP-CTFs normalized to fl-APP as measured in Western blot (t-test, P = 0.0002). (c) Quantification of ELISA analysis of soluble Aβ species (Aβ40 decreased by 66 %, t-test, P = 0.036 and Aβ42 decreased by 59 %, t-test, P = 0.023, vehicle n = 4, GSI n = 3 mice); open circles represent single data points, horizontal bars denote the mean and grey boxes the SEM. Values are mean ± SEM. (d,e) Examples of in vivo two-photon images in APPPS1 mice treated daily with vehicle (d) and 30 mg/kg GSI (e), respectively. Images are maximum projections of 50 optical sections (z-spacing 5 µm) over a depth of 250 µm. Red arrowheads indicate newly formed plaques, which are marked with white arrowheads at consecutive imaging time points. (f) Number of newly emerged plaques per standard ROI (350×350×285 µm) are lower in GSI treated mice after the first week: one-sided Mann-Whitney test, P = 0.027, values are mean ± SEM. (g) Plaques newly formed within the first week of treatment are significantly smaller in GSI treated mice (one-sided Mann-Whitney test, P = 0.014); black lines denote the mean. (h) Newly formed plaques grow significantly slower in GSI compared with vehicle treated mice; values are median ± 95% confidence interval of the median (repeated measures ANOVA, P = 0.014; APP vehicle: 22 ROIs (5 mice), 45 new plaques after first week; APP GSI: 27 ROIs (7 mice), 31 new plaques after first week). Scale bar 20 µm, * P < 0.05, *** P < 0.001. Abbreviations: fl-APP = full length APP; APP-CTF = APP C-terminal fragments. Reprint from Molecular Psychiatry with permission from Nature Publishing Group (Liebscher et al., 2014).*

In accordance with the observed increase in APP-CTF levels, we found that soluble Aβ40 and Aβ42 levels were significantly decreased by 66 % and 59 %, respectively, upon GSI application, indicating that GSI treatment efficiently lowers Aβ levels in the APPPS1 mouse model (Figure 15c). We next analysed the GSI's potential to interfere with *de novo* deposition of plaques using repeated two-photon imaging (Figure 15d,e). We found that ELN594 affected plaque formation, manifested as a drop in the number and size of newly deposited plaques in GSI treated APPPS1 mice compared with vehicle treated mice after the first week of GSI treatment (Figure 15f,g). The observed decrease in newly formed plaques after 1 week of treatment ceased over the course of the experiment, and a general decline in the occurrence of new plaques was seen in both GSI treated and control mice, which might reflect the age-dependency of plaque deposition (Figure 15f). However, plaques newly formed within the first week of treatment grew significantly slower in GSI compared with vehicle treated mice, indicating a sustained effect of the GSI throughout the treatment period (Figure 15h). Biochemical analysis of brain samples taken 24 hours following the last daily administration of ELN594 at 30 mg/kg for 4 weeks to APPPS1 and GFP wild-type mice demonstrated similar drug exposures for both groups (total brain drug concentration mean ± SEM: 4.05 ± 1.04 nM and 9.36 ± 3.85 nM for GFP wild-type and APPPS1, respectively, $P = 0.26$; Mann-Whitney-U test, Figure 14d). Values were consistent with nadir

exposures in FVB mice at the same dose analysed 24 hours after single administration (14.13 ± 7.11 nM; Kruskal-Wallis test between all 3 groups, $P = 0.13$, Figure 14c,d). The agreement between trough levels from the current repeat dose study and the single dose study suggests negligible accumulation of compound levels or induction of drug metabolizing enzymes. Good CNS penetration was also demonstrated in the APPPS1 and WT mice with brain to plasma concentration ratios (Kp) of 0.87 ± 0.2 and 1.28 ± 0.14, respectively, which is consistent with the CNS penetration in FVB mice following a single administration of ELN594 at 30 mg/kg (Kp 1.2, Figure 14b).

3.3.4. Effect of GSI treatment on plaque - associated spine and bouton alterations

We applied the GSI to APPPS1 mice daily for four consecutive weeks. WT mice were treated in addition in order to test for potential adverse effects of the treatment that have been described in a previous publication for unselective GSIs of a different structural class (Bittner et al., 2009).

GSI treatment had neither an effect on spine density in APPPS1 (Figure 16a,b) nor on those in WT mice (Figure 17a) over the course of the four-week treatment period. Importantly, GSI treatment counteracted the plaque-associated changes in spine dynamics. More specifically, in GSI treated mice we found a higher spine survival fraction near plaques (Figure 16c), a higher fraction of persistent spines (Figure 16d) and accordingly a lower fraction of transient spines (Figure 16d) compared with spines near plaques in vehicle treated mice. The pathologically enhanced elimination - and formation rates of spines near plaques in vehicle-treated mice were reduced by the GSI to levels found on dendrites further away from plaques (Figure 16e-g).

Note, presented here are average values over all time points, as spine dynamics were consistently elevated throughout the treatment period (see Figure 18a-c).

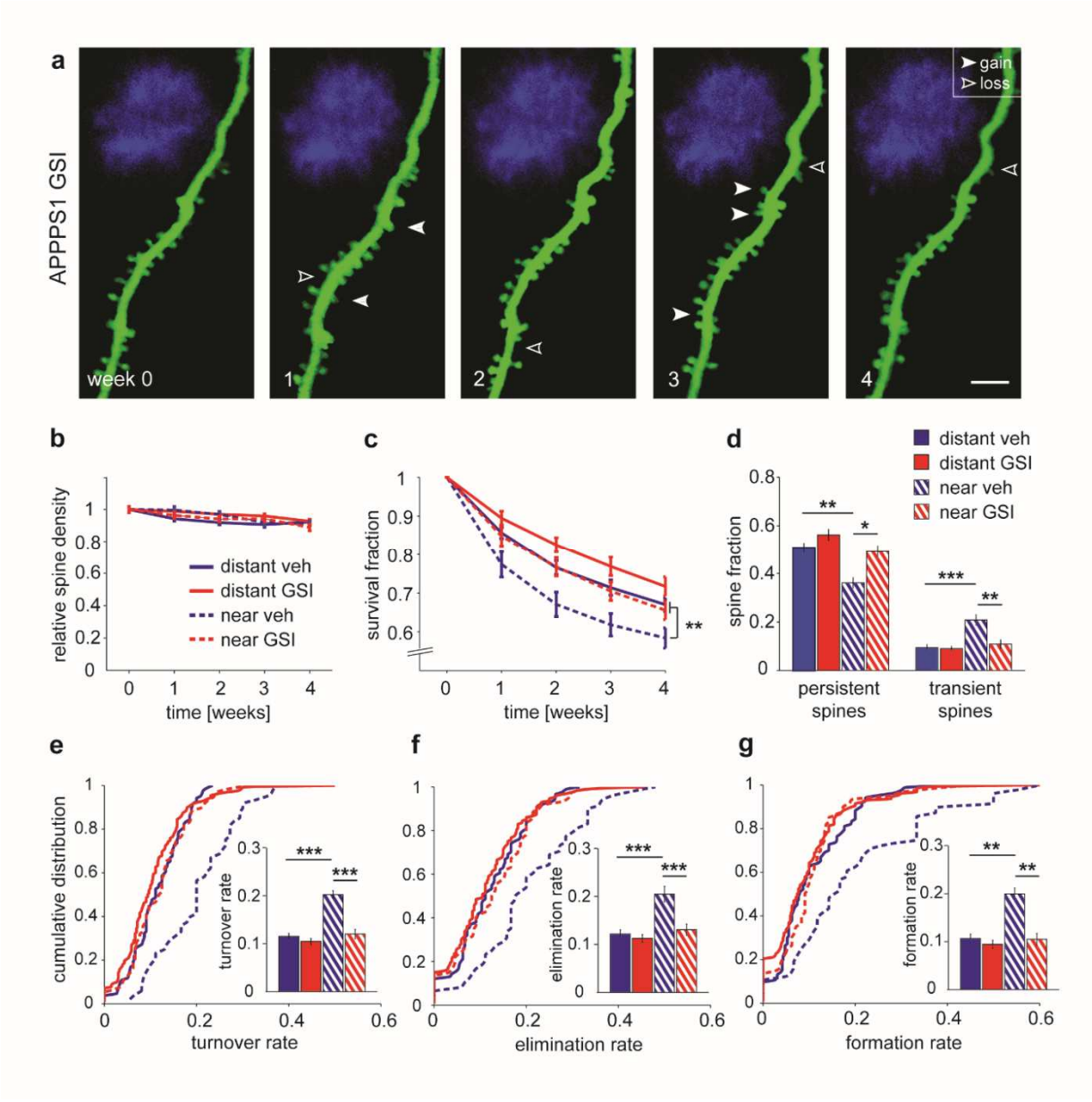

Figure 16: Effect of GSI treatment on dendritic spines in APPPS1 mice.

*(a) Example of dendritic spines in a GSI treated APPPS1 mouse in the vicinity (< 50 µm) of a plaque. The first imaging session was performed prior to the start of treatment. Images are maximum projections. (b) Spine density is not affected by GSI treatment in APPPS1 mice (repeated measures ANOVA, P = 0.72). (c) The lower survival fraction (SF) of spines in the vicinity of plaques is normalized by GSI treatment, thereby equaling the SF of spines distant from plaques in vehicle treated mice (repeated measures ANOVA, P < 0.01). (d) GSI treatment increases the fraction of persistent spines near plaques (one-way ANOVA, P < 0.05). Accordingly, the high fraction of transient spines near plaques is reduced upon GSI treatment (one-way ANOVA, P < 0.01). (e) Increased turnover of spines near plaques is reduced by the GSI (one-way ANOVA, P < 0.001). The effect is based on normalized (f) elimination - (one-way ANOVA, P < 0.001) and (g) formation rates (Kruskal-Wallis, P < 0.01). APP distant veh: n = 21 dendrites (5 mice); APP near veh: n = 12 dendrites (5 mice); APP distant GSI: n = 32 dendrites (7 mice); APP near GSI: n = 15 dendrites (7 mice). Values are mean ± SEM. Scale bar 5 µm, * P < 0.05, ** P < 0.01, *** P < 0.001. Reprint from Molecular Psychiatry with permission from Nature Publishing Group (Liebscher et al., 2014).*

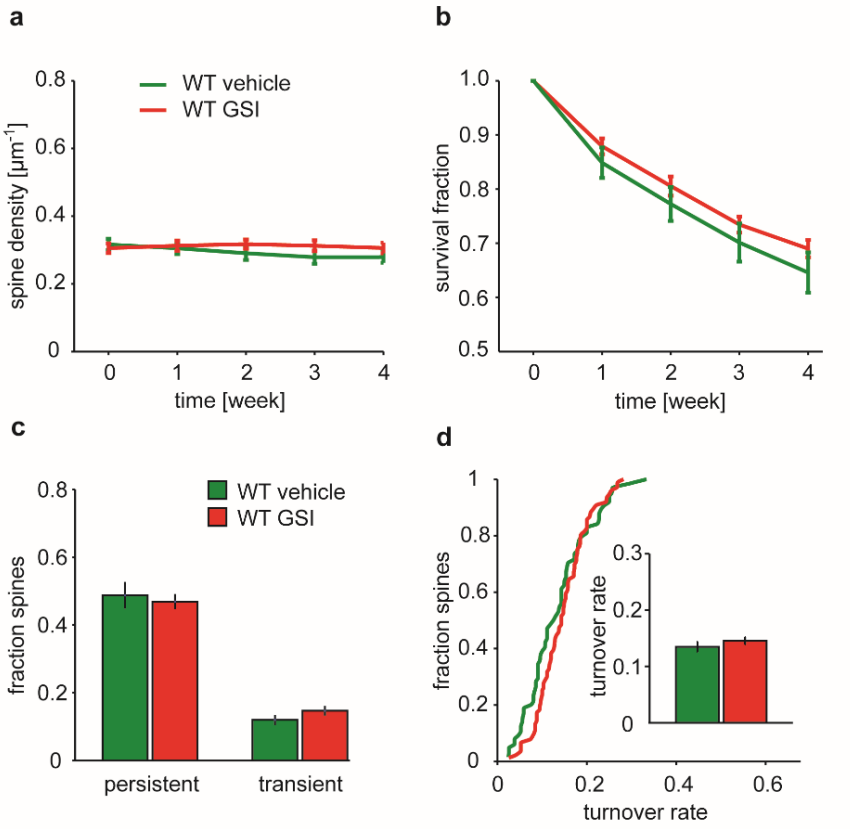

Figure 17: Lack of GSI effects on dendritic spines in WT mice.
(a) GSI treatment neither affect spine density (repeated measures ANOVA, P = 0.45) nor (b) survival fraction (repeated measures ANOVA, P = 0.28), nor (c) the fraction of persistent (t-test, P = 0.67) and transient spines (t-test, P = 0.2) in WT mice. (d) Spine dynamics are not altered upon GSI treatment: Turnover rate (averaged over all time points) does not differ significantly between treatment groups (t-test, P = 0.55). Values are mean ± SEM. WT vehicle: n = 16 dendrites (4 mice), WT vehicle: n = 19 dendrites (7 mice). Reprint from Molecular Psychiatry with permission from Nature Publishing Group (Liebscher et al., 2014).

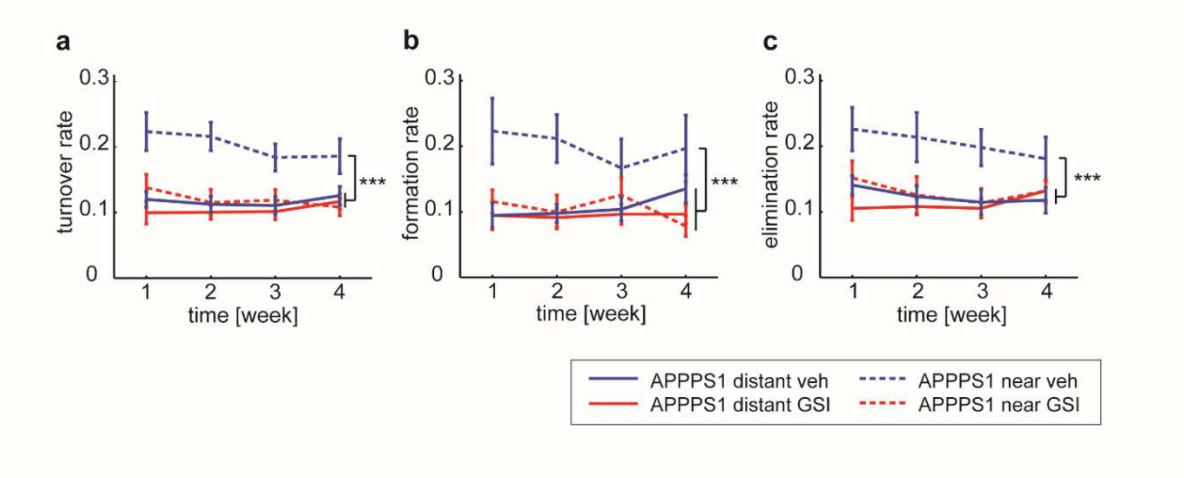

Figure 18: Temporal aspect of altered spine dynamics.
*(a) The spine turnover rate of spines near plaques in vehicle treated mice is significantly increased throughout the whole experiment (P < 0.001, APP near veh vs. either one of the other groups). (b) Spines close to plaques in vehicle treated mice exhibit an increased formation rate at all imaging time points (P < 0.001 APP near veh vs. either one of the other groups). (c) The spine elimination rate of spines near plaques in vehicle treated mice is increased at all imaging time points (P < 0.001, APP near veh vs. either one of the other groups). APP distant veh: n = 21 dendrites (5 mice); APP near veh: n = 12 dendrites (5 mice); APP distant GSI: n = 32 dendrites (7 mice); APP near GSI: n = 15 dendrites (7 mice). Data are mean ± SEM, *** P < 0.001.*

As the density of spines within a radius of 50 µm to the plaque edge correlates well with the effective plaque distance (Figure 9a), we investigated whether GSI treatment affects spines in a distance-dependent manner. While the GSI had no effect on spine density near plaques at any given distance between 0-50µm, the turnover rate was significantly reduced for spines that were more than 15 µm (yet < 50µm) away from the plaque border (Figure 19a-d).

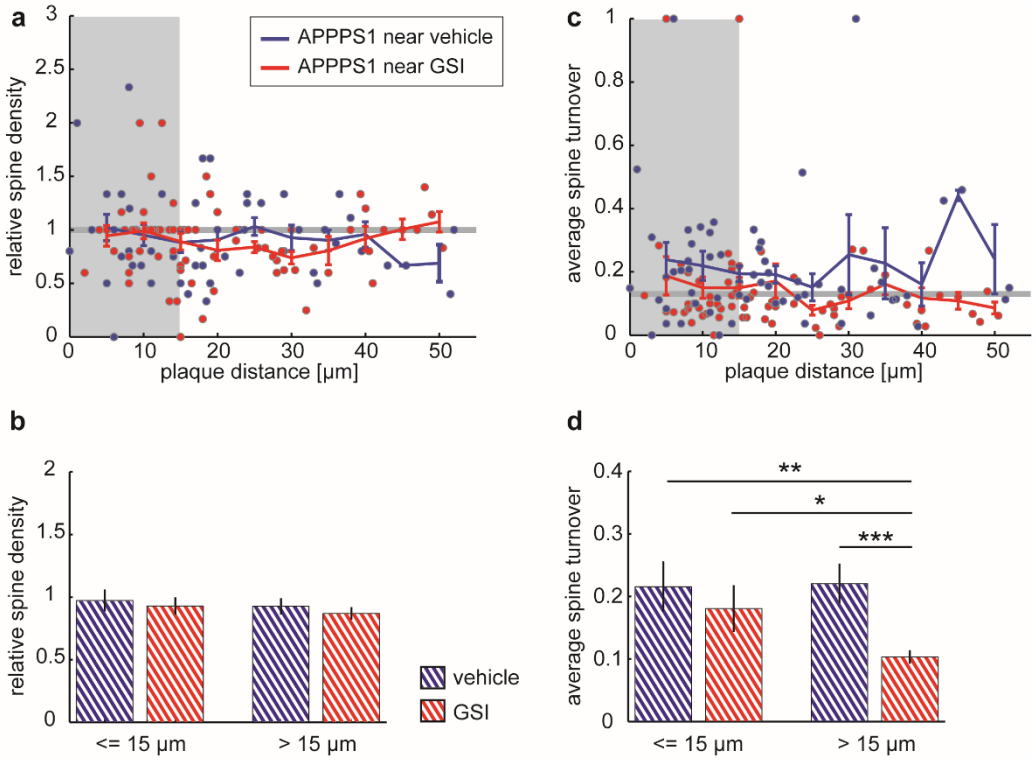

Figure 19: Plaque distance - dependent GSI effect on dendritic spines. *(a) Spine density is not affected by GSI treatment in a distance - dependent manner. Data points represent relative spine densities at the last imaging time point as a function of plaque distance. Solid lines are sliding averages over a 10 µm window with 5 µm increments. Grey line depicts relative density of 1, indicating no change in density. Grey regions indicate the plaque distances (<= 15 µm) where absolute spine density of APPPS1 mice was significantly reduced compared with spines in WT vehicle mice (see Supplementary Figure S2a). (b) Spine density below and above 15 µm plaque distance does not differ between treatment conditions (Kruskal - Wallis test, P = 0.89). (c) GSI effect on the average spine turnover rate is dependent on the distance to the plaque border. As in (a), the grey region denotes the plaque distance in which absolute spine density is significantly reduced compared with spines in WT vehicle mice. Data is referenced to the average spine turnover rate in WT vehicle mice (0.13 ± 0.016, mean depicted as dark grey line). (d) Turnover rate of spines within 15 µm does not differ between treatment conditions. In contrast, GSI treatment leads to a significant reduction of the turnover of spines > 15 µm (yet < 50µm) away from the plaque border compared with spines in vehicle treated mice at that distance and also to spines located less than 15 µm away from the plaque border in both vehicle and GSI treated mice (Kruskal - Wallis test, '>15µm vehicle' vs. '>15µm GSI' P < 0.0001, '<=15µm GSI' vs. '>15µm GSI' P = 0.034, '<=15µm vehicle' vs. '>15µm GSI' P = 0.005, post-hoc comparisons Mann - Whitney tests). APP near vehicle: 61 segments (12 dendrites, 5 mice) and APP near GSI: 75 segments (15 dendrites, 7 mice). Data are mean ± SEM. Reprint from Molecular Psychiatry with permission from Nature Publishing Group (Liebscher et al., 2014).*

In addition to alterations in synapse number and turnover, pathology might also be reflected in changes to the strength of a synapse, which is known to correlate well with spine size (Harris and Stevens, 1989; Kasai et al., 2010; Knott et al., 2006). We hence determined integrated spine brightness, as a measure for spine size (Hofer et al., 2009). In line with a previous report (Loewenstein et al., 2011), the overall distribution of spine sizes resembled a log-normal distribution, both for spines close to plaques in APP and WT mice (Figure 20a,c). Average spine size as well as spine size distribution did not differ between treatment groups (Figure 20 b,c,d).

Since stable spines are considered the structural correlates of long-term memories (Xu et al., 2009; Yang et al., 2009), we next performed the same analysis separately for persistent spines. We determined their size difference between the first and the last imaging time point (Figure 20e). In line with our findings of higher spine turnover rates in the vicinity of plaques, we observed a significantly higher fraction of persistent spines with a large size change (difference in integrated brightness larger than the mean difference ± 1.5 x standard deviation of persistent spines size changes in WT vehicle treated mice) close to plaques (WT vehicle 15.4% vs. APP near vehicle 27.7%, Figure 20f). GSI treatment led to a reduction of this 'large size change fraction' of persistent spines (20.1%), which did not significantly differ anymore from WT vehicle mice (Figure 20f).

GSI treatment did not affect spines further away from plaques and in WT mice (for data on WT mice, see Figure 17a-d), indicating no obvious neuropathological side effect of the GSI treatment. Spines near plaques are less stable than those further away. The distance of the analysed dendritic stretch to the respective plaque as well as plaque size could have biased our results. We hence compared the average and the minimum distance of dendritic stretches to plaques as well as plaque size between treatment conditions and found no difference (plaque size $P = 0.34$, average plaque distance $P = 0.49$, minimum plaque distance $P = 0.37$, all Mann-Whitney tests, Figure 21a-c), excluding those factors as potential confounds.

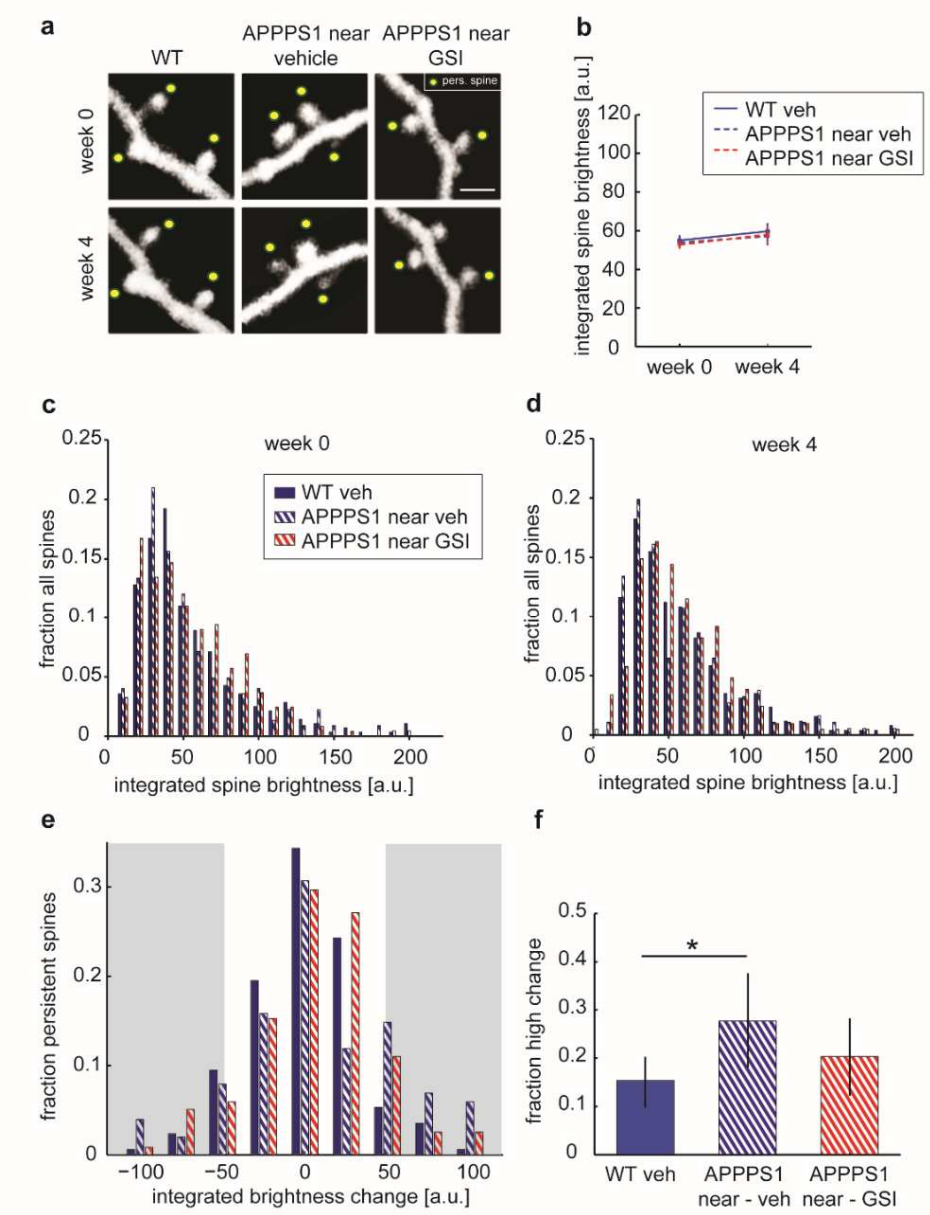

Figure 20: Spine size distribution.

(a) Examples of spines at week 0 and week 4 for the WT vehicle, APP near vehicle and APP near GSI cohort. Persistent spines (spines present at all imaging time points) are denoted with a yellow dot. (b) Average spine size (assessed by determining integrated spine brightness, see Materials & Methods) does not differ between groups and time points (between groups at week 0: P = 0.79, between groups at week 4: P = 0.4 both Kruskal-Wallis; between time points: WT veh P = 0.07, APP near veh P = 0.22, APP near GSI P = 0.054). (c) Size distributions of all spines in WT vehicle mice, near plaques in APP vehicle, and near plaques in GSI treated mice at week 0 (pre-treatment). There is no difference between the distributions (WT veh vs APP near veh P = 0.68, WT veh vs APP near GSI P = 0.59, APP near veh vs APP near GSI P = 0.26, Kolmogorov-Smirnov test). (d) Similarly, spine size distribution at week 4 does not differ significantly between these groups (WT veh vs APP near veh P = 0.56, WT veh vs APP near GSI P = 0.48, APP near veh vs APP near GSI P = 0.07, Kolmogorov-Smirnov test). (e) Distribution of persistent spine size changes between the first and the last imaging session. (f) Fraction persistent spines with a change in size between week 0 and 4 exceeding the mean difference ± 1.5 x standard deviations of persistent spine size changes in WT vehicle treated mice (-0.06 ± 48.89 a.u.; grey regions in (e)). The fraction of such spines with large size changes is significantly increased close to plaques (WT vehicle 15.4% vs. APP near vehicle 27.7%, P = 0.018, Fisher's exact test). GSI treatment leads to a reduction of this 'large size change fraction' of persistent spines (20.1%), which does not significantly differ from WT vehicle mice anymore (P = 0.34, Fisher's exact test; WT veh 169 spines, APP near veh 101 spines, APP near GSI 118 spines). Data are median ± 95% confidence intervals. Reprint from Molecular Psychiatry with permission from Nature Publishing Group (Liebscher et al., 2014).

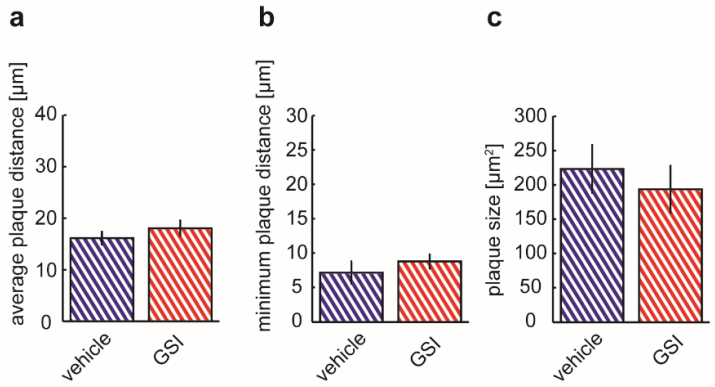

Figure 21: Plaque parameters do not differ between treatment groups.
(a-c) Factors potentially affecting spine stability near plaques, such as the distance (defined as the average of the plaque distance of both end points and the center of the respective dendritic stretch) (a), the minimum distance between dendritic stretch and plaque border (shortest distance) (b), or plaque size (c) do not differ between treatment groups. APP near vehicle: 12 dendrites (5 mice) and APP near GSI: 15 dendrites (7 mice). Values are mean ± SEM. Reprint from Molecular Psychiatry with permission from Nature Publishing Group (Liebscher et al., 2014).

Owing to the high variability, it was more difficult to pinpoint the impact of the GSI on bouton dynamics (Figure 22a), but overall we found the same trend as for dendritic spines. Bouton density was not significantly affected by the GSI treatment, yet a trend towards a decrease throughout the imaging period was observed near plaques in vehicle treated mice (Figure 22b). These findings notwithstanding, we did observe a normalization of the bouton survival fraction near plaques to levels found in those distant from plaques (Figure 22c). The significantly elevated bouton turnover rate near plaques was somewhat decreased by the GSI, but the effect did not reach significance (Figure 22d). The same held true for the fraction of persistent boutons near plaques, where we observed a non-significant increase after GSI treatment (one-way ANOVA, $P = 0.22$, Figure 22e).

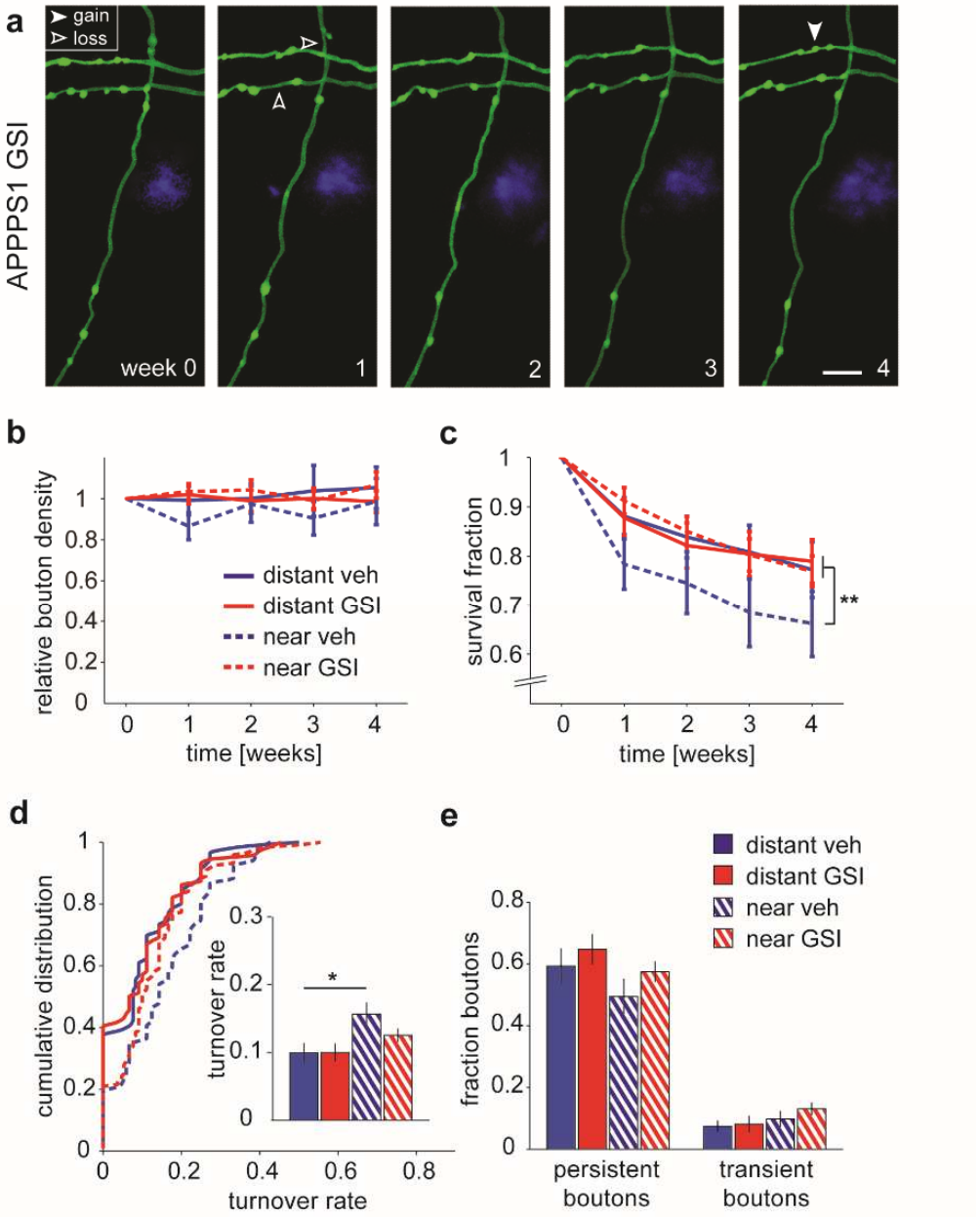

Figure 22: GSI effect on axonal boutons in APPPS1 mice.

*(a) Example of an axonal stretch near a plaque in an APPPS1 mouse. (b) Bouton density is not affected by GSI treatment (Friedman's test, P = 0.07). (c) The lower survival fraction of boutons near plaques is normalized to levels observed distant from plaques (repeated measures ANOVA APP distant vehicle vs. APP near vehicle P < 0.01, APP near vehicle vs. APP near GSI P < 0.001). (d) The increased turnover rate of boutons near plaques is reduced after treatment; the effect did not reach significance (Kruskal -Wallis, APP near vehicle vs. APP near GSI P > 0.05). (e) Bouton lifetime fractions do not differ significantly between treated and untreated mice. APP distant veh: n = 14 axons (4 mice); APP near veh: n = 13 axons (4 mice); APP distant GSI: n = 18 axons (7 mice); APP near GSI: n = 30 axons (7 mice). Values are means ± SEM, Scale bar 10 µm * P < 0.05, ** P < 0.01. Reprint from Molecular Psychiatry with permission from Nature Publishing Group (Liebscher et al., 2014).*

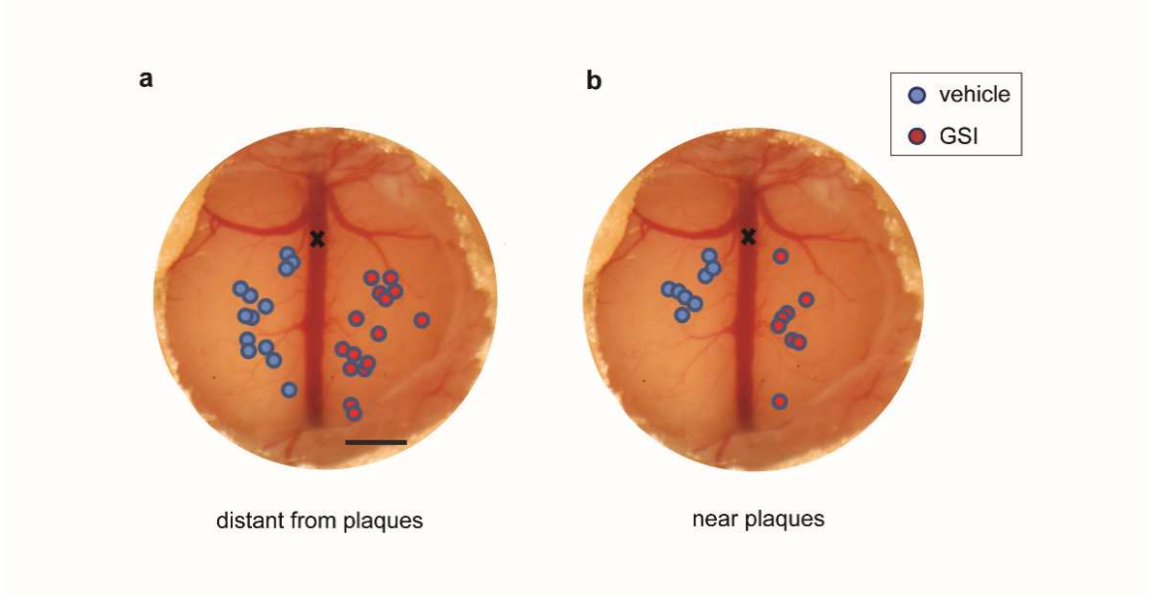

Figure 23: Position of imaged regions within the cranial window.
(a) Localization of imaging regions of dendrites distant from plaques superimposed on a representative example of a cranial window. Regions were sampled from both hemispheres but for the purpose of display all locations acquired within vehicle treated mice are shown on the left side (blue circles) and all spots taken from GSI treated mice on the right (red circles). Note number of imaging sites does not correspond to the number of analysed neurites as in some cases multiple stretches located within the same imaging region were investigated. X denotes position of Bregma. (b) Position of imaged regions bearing dendrites close to plaques (APP near spots) superimposed on the same cranial window example. Scale bar 1mm. Reprint from Molecular Psychiatry with permission from Nature Publishing Group (Liebscher et al., 2014).

Taken together, these data demonstrate that the dynamics of both the pre- and postsynaptic compartment are affected by the amyloid plaque pathology, resulting in a strong synaptic instability. Moreover, we found that interference with Aβ generation by applying the selective GSI, ELN594, can attenuate the plaque-associated instability of synaptic structures. ELN594 does neither affect spines or boutons further away from plaques in APPPS1, nor those in WT mice, and hence seems to be devoid of apparent neuropathological side effects.

4 PROJECT 2

Functional alterations of neurons in primary visual cortex of APP/PS1 transgenic mice

4.1. Abstract

The following sections 4.1. – 4.3. (page 64 - 87) are taken from (Liebscher et al., 2016).

Neurodegenerative processes in Alzheimer's disease (AD) affect the structure and function of neurons (Benilova et al., 2012; Haass and Selkoe, 2007; Koffie et al., 2011; Selkoe, 2002), resulting in altered neuronal activity patterns comprising neuronal hypo- and hyperactivity (Busche et al., 2008; Grienberger et al., 2012) and causing the disruption of long-range projections (Delbeuck et al., 2007; Liu et al., 2014). Impaired information processing between functionally connected brain areas is evident in defective visuomotor integration, an early sign of the disease (Hawkins and Sergio, 2014; Tippett and Sergio, 2006; Velasques et al., 2011). The cellular and neuronal circuit mechanisms underlying this disruption of information processing in AD, however, remain elusive. Recent studies in mice suggest that visuomotor integration already occurs in primary visual cortex (V1), as it processes not only sensory input but also exhibits strong motor-related activity, likely driven by neuromodulatory or excitatory inputs (Bennett et al., 2013; Fu et al., 2014; Keller et al., 2012; Lee et al., 2014; Niell and Stryker, 2010; Polack et al., 2013). Here, we probed the integration of visual - and motor related - inputs in V1 of behaving APP/PS1 (Radde et al., 2006) mice, a well characterized mouse model of AD, using two-photon calcium imaging. We find that sensorimotor signals in APP/PS1 mice are differentially affected: while visually-driven and motor-related signals are strongly reduced, neuronal responses signaling a mismatch between expected and actual visual flow are selectively spared. We furthermore observe an increase in aberrant activity during quiescent states in APP/PS1 mice. Jointly, the reduction in running-correlated activity and the enhanced aberrant activity degrade the coding accuracy of the network, indicating that the impairment of visuomotor integration in AD is already taking place at early stages of visual processing.

4.2. Material & Methods

4.2.1. Animals

Female APP/PS1$^{+/-}$ mice (bearing the Swedish double-mutation KM670/671NL within the APP gene, as well as a L166P mutation within the Presenilin1 (PS1) gene, both driven by the neuronal Thy-1 promoter) and APP/PS1$^{-/-}$ (referred to as WT) siblings were housed in groups of 3-6 individuals in standard cages, with standard bedding and additional nesting material. Food and water were provided *ad libitum*. Mice were kept under a 14/10 hours light/dark cycle. In total, 6 APP/PS1 and 5 WT mice at the age of 10-11 months were included in the study. In each mouse, 2 to 4 regions at depths of 120 – 200 μm below the pial surface were imaged, resulting in a total number of 1350 cells (n = 22 experiments) in APP/PS1 and 1399 cells (n = 21 experiments) in WT mice. All animal procedures followed a protocol approved by the local authorities (Regierung von Oberbayern).

4.2.2. Cranial window surgery and virus injection

At the age of 10 months, mice were injected with AAV2/1.hSyn.GCaMP6m.WPRE.SV40 into V1 and a cranial window was implanted above as described previously (Holtmaat et al., 2009). Briefly, mice were anesthetized with Midazolam (0.05 mg/kg Dormicum, Roche), Fentanyl (5.0 mg/kg Hexal), and Medetomidin (0.5 mg/kg Dormitor, Orion Pharma). A circular craniotomy (diameter 5 mm, centered over V1) was performed, and a round 5 mm glass coverslip was fit snugly into it. The craniotomy was sealed with UV curable dental acrylic (Venus Diamond Flow, Heraeus Kulzer GmbH). A metal head bar was firmly attached to the skull with dental acrylic (Paladur, Heraeus Kulzer GmbH), allowing access of the objective to the cranial window (Leinweber et al., 2014). This procedure allowed for a stable head and brain position during awake imaging sessions. Imaging started four weeks post injection. At least 24 hours before imaging experiments mice were injected intraperitoneally with Methoxy-XO4 (Neuroptix Corporation) at a concentration of 3.33 mg/kg (3.3% vol of 10 mg/ml stock solution in DMSO (light shielded), 6.66% vol Cremophore EL (Sigma Aldrich) in 90% vol PBS (Klunk et al., 2002), a dye that readily crosses the blood-brain-barrier and binds to fibrillary Aβ.

4.2.3. Two-photon imaging of behaving mice

Images were acquired on a custom-built two-photon microscope equipped with an 8 kHz resonant scanner, resulting in frame rates of 40 Hz at an image resolution of 400 x 750 pixels (Keller et al., 2012). The field of view for functional imaging was approximately 190 x 250 µm, and overview z-stacks to visualize plaque positions were acquired over a region of 340 x 500 x 5 µm (xyz). Light source was a Ti:Sapphire laser with a DeepSee pre-chirp unit (Spectra Physics MaiTai eHP). Excitation wavelength for GCaMP6m functional imaging was 930nm. Overview z-stacks were acquired at 830nm to excite both GCaMP6m and Methoxy-XO4 labeled plaques. Laser power under the objective (16 x, 0.8 NA, Nikon) was between 15-25 mW for all imaging experiments. During imaging, mice were allowed to run on an air-supported styrofoam ball (Dombeck et al., 2007) with a pin restricting movement to forward and backward rotation. Running velocity was tracked with an optical computer mouse placed in front of the ball. To avoid stimulus light leaks, the monitors were flickered at 16 kHz, locked to scanning (Leinweber et al., 2014).

4.2.4. Experimental design

Two LCD monitors arranged at an angle of 60° to one another in front of the mouse were used to display full-field vertical gratings. This monitor configuration covered 180° along the horizontal axis and 50-65° along the vertical axis of the mouse's visual space (Keller et al., 2012). Visual flow of vertical full - field moving sinusoidal gratings with a spatial frequency of 0.04 cycles per degree was either coupled to the running velocity of the mouse (closed loop or feedback configuration) or uncoupled from actual running speed, during re-play of the visual flow of the previous feedback session (open loop or playback configuration). In some experiments, short interruptions of 1s duration (perturbations) of the visual flow were introduced while the mouse was in closed loop configuration. These perturbations were used to induce sensorimotor mismatch signals. Each experiment was carried out in the following sequence, with the mouse free to run throughout (Figure 12C): First 8.3 min (20.000 imaging frames) of visual feedback with interspersed brief perturbations of the visual flow (Poisson distribution, on average 5/min) were conducted, followed by a 'pure' 8.3 min feedback session without any perturbations and a subsequent 8.3 min playback session, where visual flow of the initial experiment (feedback with perturbations) was re-played. Subsequently, all lights were switched off and the mouse was allowed to dark-adapt for 30 min. The second part of the experiment consisted of 6.25 min (15.000 imaging frames) recorded in darkness.

To assess orientation and direction tuning, we presented sinusoidal gratings with a temporal frequency of 2 Hz and a spatial frequency of 0.04 cycles per degree at 8 different directions spaced by 45°. Each trial consisted of 8 sec of standing grating, followed by 6 sec of moving grating. The complete stimulus set was repeated 10 times, with a random order of directions. Mice were free to run throughout the experiments.

4.2.5. Pupil tracking

In all experiments, the mouse's left eye was continuously recorded with a video camera (The Imaging Source, frame rate 30 Hz, see Figure S4). Pupil position and diameter were assessed online by a custom-written algorithm in LabVIEW (National Instruments) (Sakatani and Isa, 2007). Saccades were defined as displacement of the pupil center by more than 3 pixels (60 μm).

4.2.6. Image processing and data analysis

All analysis was carried out in Matlab (MathWorks) using custom written routines. Full frame images were registered, and regions of interests (ROIs) were manually selected based on both a maximum and a mean projection of all frames. For most neurons, a ring-like structure was chosen, excluding the nucleus. In case of directly abutting cells, pixels containing signal from both neurons were excluded from the selection. The fluorescence intensity of all pixels comprising the ROI was averaged, and intensity traces were low pass filtered at 10 Hz. To account for contamination by both local (occasionally active neurites next to selected ROIs) and global (increase in fluorescence over a larger area, not attributable to a discrete structure) neuropil signals, the following measures were taken: the initial ROI was fitted with an ellipse and this ellipse was stretched by 10 pixels. All pixels of the initial ROI, as well as those in neighbouring ROIs were excluded from the resulting larger ellipse. The corrected ROI signal was then computed according to the following equation (adapted from (Kerlin et al., 2010)):

$$F_{ROI\_comp} = F_{ROI} - 0.7 \times F_{neuropil} + 0.7 \times \text{median}\,(F_{neuropil})$$

With F_{ROI_comp} representing the neuropil compensated fluorescence of the ROI, F_{ROI} referring to the fluorescence signal of the initial ROI selection and $F_{neuropil}$ to the signal stemming from the neuropil (Chen et al., 2013). In order to estimate the baseline level (F_0) of the fluorescence traces, we derived a "noise-band" by

subtracting the 8th percentile within a short sliding window covering 40 frames (1s). This procedure largely smoothed out activity transients. The median of this "noise band" reflects the baseline well, as judged by visual inspection, even for highly active cells and was hence used as F_0. Consequently, relative changes in fluorescence (ΔF/F traces) were computed by dividing the corrected fluorescence trace by the median of the "noise band" and subtracting 1. Cells were classified as active in a particular experiment if they crossed a threshold of baseline + 3.72 x standard deviation of the ΔF/F trace (i.e. probability of false positive by chance being 0.0001) at least once for a minimum of 40 continuous frames (1 sec). All correlation analyses were performed on ΔF/F traces deconvolved with a nonnegative deconvolution algorithm; for details see (Huber et al., 2012; Vogelstein et al., 2010).

4.2.7. Analysis of responses to moving grating stimulation

A neuron was defined as strongly driven by visual stimulation if it displayed a significant (average activity within 0.5-2 sec after onset of moving grating compared with the average neuronal activity within 0.5 sec prior to stimulus onset, Wilcoxon rank sum test, α level 0.01) and sufficiently large (integral > 1.2 ΔF/F within 0.5-2 sec after moving onset, corresponding to an average ΔF/F of 2%) response to the presentation of the moving grating while the mouse was stationary. Neuronal responses were normalized to the average activity within 1 sec prior to stimulus onset. Neuronal responses to moving gratings were separately analysed during stationary and during running periods. In order to reduce confounding neuronal activity coinciding with the onset of the moving grating but related to running on- and offsets, we only considered visual onsets during clear stationary (no running activity 1/2 sec before until 3 sec after onset of moving grating) and running epochs (running 1/2 sec before until 2 seconds after onset of moving grating), respectively. The orientation (OSI) and direction selectivity indices (DSI) were computed as follows: $OSI = (R_{pref} - R_{ortho})/(R_{pref} + R_{ortho})$, with R_{pref} being the median response at the preferred orientation and R_{ortho} the median response to the orthogonal orientation (the median was chosen as the responses to moving gratings were non-normally distributed.). $DSI = (R_{pref\_dir} - R_{opp\_dir})/(R_{pref\_dir} + R_{opp\_dir})$, with R_{pref_dir} being the median response at the preferred direction and R_{opp_dir} the median response to the opposite direction. The neuronal tuning curves were obtained by fitting the average response to each direction with a two peaked Gaussian curve (Goltstein et al., 2015; Li et al., 2008). The tuning curve bandwidth reflects half width at $1/\sqrt{2}$ maximum.

4.2.8. Analysis of sensorimotor responses

A neuron was defined as strongly driven by a given sensorimotor event, if it displayed both a significant (average activity within 0.5- 2 sec (for sensorimotor mismatch signal 0.5-1.5 sec) after onset of the sensorimotor event compared with the average neuronal activity within 0.5 sec prior to stimulus onset, rank sum test, α level 0.01) and sufficiently large (average $\Delta F/F > 2\%$ within 0.5 – 2 sec upon onset (within 0.5-1.5 sec for sensorimotor mismatch)) response. The total number of sensorimotor onsets we analysed were as follows: (i) running with visual feedback: WT 531 and APP/PS1 557; (ii) running in the dark: WT 201 and APP/PS1 191; (iii) playback: WT 443 and APP/PS1 460. Initial running speed and virtual velocity of the playback was higher in WT mice compared to APP/PS1 mice ((i) running with feedback in WT 6.72 [3.28; 10.97] cm/s and in APP/PS1 4.86 [2.36; 8] cm/s, rank sum test, $P < 0.001$; (ii) running in the dark: WT 6.45 [3.28; 10.97] cm/s and in APP/PS1 4.14 [1.99; 6.86] cm/s, $P < 0.001$; (iii) playback: WT 5.4 [2.1; 8.85] cm/s and in APP/PS1 3.76 [1.4; 7.27] cm/s, $P < 0.001$, data are median velocity [interquartile range]). To account for the differences in running speed and virtual velocity between genotypes we bootstrapped the population responses by matching the two velocity distributions by resampling. To this end a sample of 1000 sensorimotor evoked signals in APP/PS1 and WT mice was pseudorandomly selected to match the original distribution of initial velocities; this procedure was repeated 100 times (Figure S3). Overall fraction of time spent running in the feedback session (i.e. speed > 0.5 cm/s) was 28.42 ± 1.6 % in WT and 31.8 ± 1.6 % in APP/PS1, Student's *t*-test, $P = 0.14$; during playback sessions in WT: 32 ± 3.2 % and 34 ± 2.6 % in APP/PS1, $P = 0.63$ and during darkness in WT: 40.45 ± 2.5 % and APP/PS1: 45.9 ± 3.9 %, $P = 0.26$.

When assessing the correlation of neuronal activity and running velocity, we excluded data in a two second window prior and post saccadic eye movements and prior and post running periods from data analysis in order to minimize the effect of potential signals associated with the initiation and cessation of movements. The same corrected traces were used to assess pairwise neuronal correlations during quiescence and locomotion.

4.2.9. Random Forests Model

To decode behavioural state from neuronal responses we used a classifier based on a random forest regression tree algorithm, for details see (Huber et al., 2012). We applied this method to the feedback session,

aiming at decoding the actual running velocity (running is treated as a continuous variable). For all analysis the Matlab (Mathworks) implementation of the random forest algorithm (treebagger) was used. The algorithm was trained on 75 % of the data, repeated 4 times, each round with the onset of the training set circularly shifted along the data vector. The remaining 25 % of data were used for cross validation (R^2 between the actual and running velocity predicted by the model). Shown is the average R^2 out of the four repetitions for each experiment.

4.2.10. Distance to nearest plaque

The position and size of the ROIs were projected into the 3D rendered overview stack. The two channels carrying either the GCaMP6m or the Methoxy-XO4 signal were background subtracted, and subsequently the GCaMP6m channel was subtracted from the Methoxy-XO4 channel in order to remove slight bleed through. Detection stringency of the Methoxy signal was set to the median + 2 x standard deviation of the background signal. Plaque distance is the 3D Euclidean distance between the centroid of the respective ROI and the nearest Methoxy positive voxel (Supplementary Figure S13A). All overview stacks were visually checked for correct plaque detection and 3D rendered stacks were inspected for accurate neuron - plaque assignment (ruling out accidental pairing with voxels carrying signal stemming from the dura (due to generation of second harmonics)).

4.2.11. Immunohistochemistry

Animals were cardially perfused with saline and 4% paraformaldehyde (PFA), after which brains were gently dissected out of the skull. Brains were cryoprotected in a 30 % sucrose solution until they sank. They were then cut parallel to the imaging plane on a cryostat into 50 µm thick sections. Sections were blocked overnight with 10% normal goat serum containing 1% Triton X-100 in PBS, before they were incubated with the primary antibodies (rabbit anti-VIP 1:500 (ImmunoStar), mouse anti-PV 1:1000 (Swant)) overnight. Incubation with secondary antibodies (goat anti-rabbit Alexa Fluor 633 1:200, goat anti-mouse Alexa Fluor 405 1:200, both Life Technologies) was conducted for 2 hours at room temperature. Confocal stacks (Leica TCS SP8) were acquired first at a low magnification (10x objective, HC PL Fluotar, Leica) to allow for re-identification of imaged regions based on fiduciary markers, such as blood vessel patterns, which were compared with *in vivo* overview z-stacks. Confocal stacks of re-identified imaging spots were then acquired

with a 20x objective (HC PL APO CS2, Leica). In total, 665 out of 1399 imaged neurons in 3 WT mice were identified, of which 16 were PV and 18 VIP positive neurons, and 1154 out of 1350 imaged neurons in 6 APP/PS1 mice were identified, of which 38 were PV and 37 VIP positive cells.

4.2.12. Statistics

Unless stated otherwise we employed a Student's *t*-test or a Wilcoxon rank sum test in case of non-normality to compare fractions. Cumulative distributions were analysed with the Kolmogorov-Smirnov test (KS test). The difference between population responses was tested by comparing the average area under the curve between 0.5-2.5 sec after the respective onset (0.5 – 1.5 sec for mismatch responses) for each 'neuron – sensorimotor onset' response pair. Cross validation of the actual and the model predicted running velocity was implemented by computing the variance explained (R^2, with R being the Pearson correlation coefficient) between both vectors. The difference of the R^2 values between genotypes was tested with a Wilcoxon rank sum test.

4.3. Results

To probe the integration of multimodal inputs in primary visual cortex (V1), we recorded both sensory - and motor-related activity during active behaviour by two-photon imaging of layer II/III neurons expressing the genetically encoded calcium indicator GCaMP6m (Chen et al., 2013) (Figure 24A-B). We used mice at the age of 10-11 months, when cortical plaque load in APP/PS1 (Radde et al., 2006) mice is prominent. We employed a visual flow feedback paradigm, in which the velocity of a mouse running on a spherical treadmill was coupled to visual flow feedback generated by drifting vertical gratings presented on either side of the mouse (feedback, closed loop; Figure 24C).

4.3.1. Sensorimotor signals in primary visual cortex of APP/PS1 mice

We first assessed how many neurons were *active* (see Supplemental Experimental Procedures) under this condition in both wild type (WT) and APP/PS1 mice, and found significantly fewer active neurons in APP/PS1 mice (Figure 24D).

In a previous study, altered neuronal activity patterns in anesthetized mice were linked to amyloid plaque proximity (Busche et al., 2008). We therefore analysed the plaque distance of active and non-active cells in awake mice, but did not observe a difference (Figure 25A-D).

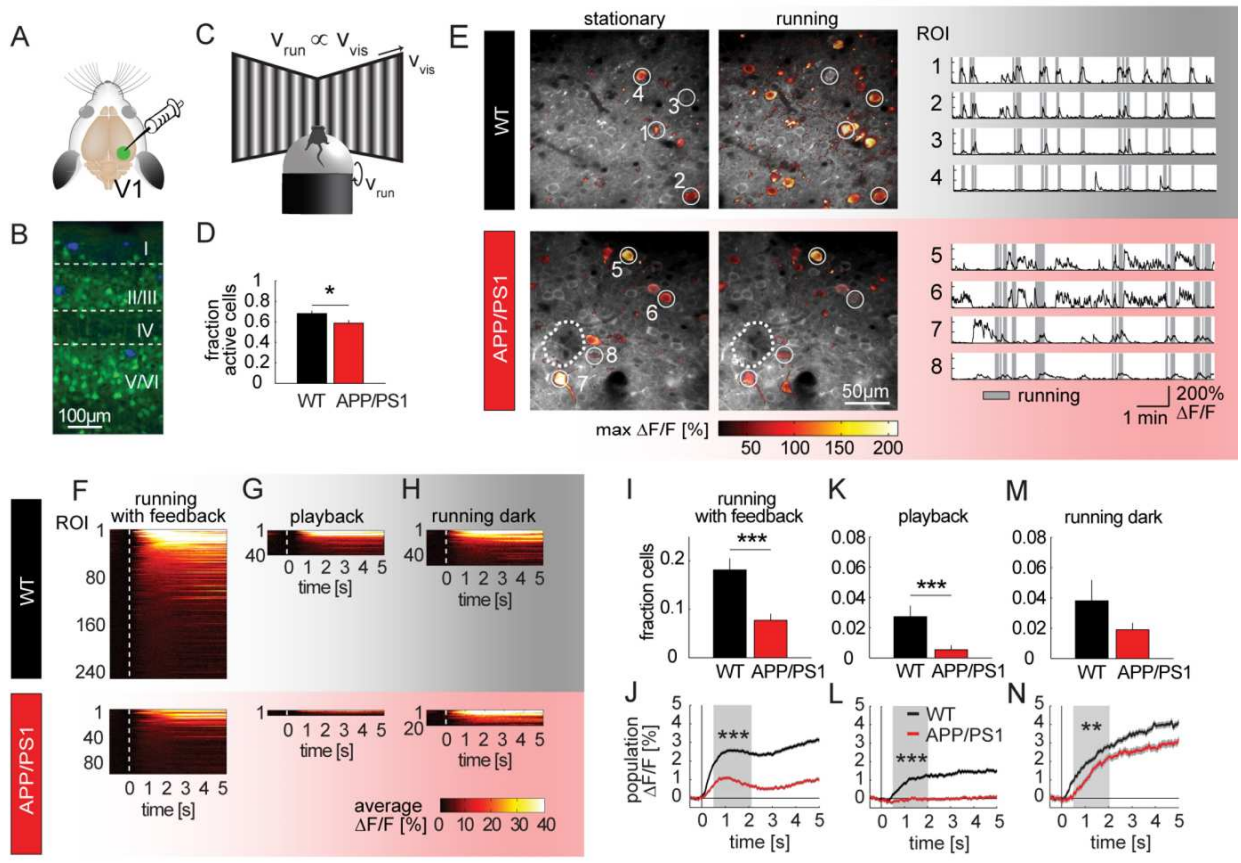

Figure 24: Impaired sensorimotor signals in V1 of APP/PS1 mice.

*(**A**) Mice were injected with AAV2/1-hsyn-GCaMP6m in V1. (**B**) Epifluorescence image of a histological section through V1. GCaMP6m expressing neurons are pseudocoloured in green. Amyloid plaques stained in vivo with Methoxy-XO4 are shown in blue. Cortical layers are delineated by dashed lines. (**C**) Experiments were conducted in closed loop condition, in which locomotion of the mouse was coupled to visual flow feedback, in open loop condition (playback) and in darkness. (**D**) Average fraction of active cells in feedback sessions in each experiment (rank sum test, P = 0.015, WT: n = 21, APP/PS1: n = 22). Amyloid plaque proximity did not differ between active and silent neurons (see Supplementary Figure S13). (**E**) Examples of imaging regions in WT and APP/PS1 mice, color coding indicates maximum neuronal activity during stationary periods and running with visual feedback. Dashed lines in the lower panel delineate the position of an amyloid plaque. Activity traces of example neurons (ROI – region of interest) marked by circles in the activity maps are depicted. Gray areas denote running periods. (**F-H**) Heat maps depicting average activity of responsive neurons to running with visual feedback (F), passive playback (G) and running in the dark (H) sorted by response magnitude in WT (upper panel) and APP/PS1 (lower panel) mice. (**I**) Fraction of neurons in each experiment that were strongly driven by running with visual feedback (rank sum test, $P = 1.6 \times 10^{-4}$, WT n = 21, APP/PS1 n = 22) and (**J**) the average population response to running with visual feedback (Student's t – test for the difference of the area under the curve (0.5 – 2 sec upon respective onset (gray box)), $P < 10^{-40}$) is significantly reduced in APP/PS1 mice. An effect that was also observed in inhibitory neurons (see Figure 26). (**K**) Fraction of cells strongly driven by passive playback in each experiment is also significantly lower (rank sum test, $P < 10^{-3}$, WT n = 21, APP/PS1 n = 22) in APP/PS1 mice, as is (**L**) the population response to playback (Student's t – test, $P < 10^{-21}$). (**M**) The fraction of neurons driven by running in the dark in each experiment does not differ significantly between genotypes (rank sum test, P = 0.5, WT n = 21, APP/PS1 n = 22), while (**N**) the average population response to running in the dark is reduced in APP/PS1 mice (Student's t – test, $P < 10^{-3}$). Differences in population responses were not due to differences in running or playback velocities (see Figure 27). Data in (D, I, K, M) represent mean ± SEM. In total 1399 neurons in 21 experiments in WT mice and 1350 neurons in 22 experiments in APP/PS1 mice were analysed. * P < 0.05, ** P < 0.01, *** P < 0.001. Reprinted from Current Biology with permission from Elsevier (Liebscher et al., 2016).*

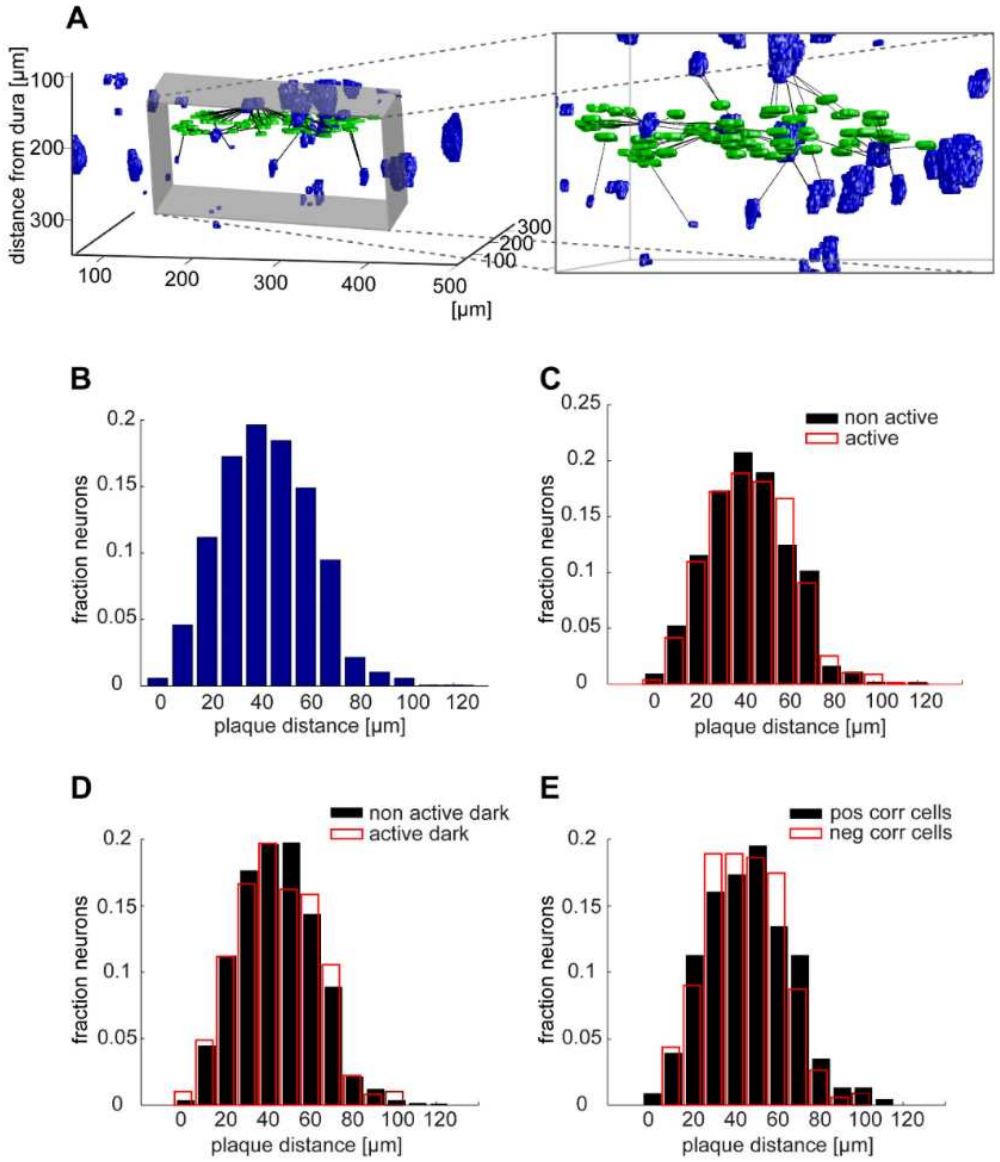

Figure 25: Amyloid plaque detection.
*(**A**) 3D rendered overview stack depicting the position and size of plaques (blue, visualized by Methoxy-XO4 labeling) with the scaled ROI selection superimposed (green). Inset: magnified view at vertically rotated angle. Black lines mark the Euclidean distance to nearest plaque containing voxel. (**B**) Distribution of plaque distances for all cells analysed in APP/PS1 mice (43.9 ± 18.5 µm). (**C**) Plaque distances of active and non - active cells during feedback sessions (active cells: 44.7 ± 18.7 µm, non-active cells: 42.7 ± 18.3 µm, P = 0.054). (**D**) Plaque distances of active and non - active cells in the dark sessions (active cells: 44.1 ± 19 µm, non-active cells: 43.7 ± 18.3 µm, P = 0.7). (**E**) Distribution of plaque distances of neurons positively and negatively correlated with running (negatively correlated neurons 44.7 ± 17.9 µm, positively correlated cells 45.9 ± 20.1 µm, P = 0.46). Data are mean ± standard deviation, Student's t-test). Reprinted from Current Biology with permission from Elsevier (Liebscher et al., 2016).*

Locomotion elicits responses in a substantial proportion of neurons in V1 (Keller et al., 2012; Lee et al., 2014) (Figure 24E). If projections driving these responses are impaired in APP/PS1 mice, activity in V1 evoked by running with visual feedback should be reduced. Indeed, we observed both quantitative and

qualitative differences in the neuronal responses during locomotion in APP/PS1 mice. The fraction of neurons that were strongly driven by running with feedback was significantly lower in APP/PS1 mice (Figure 24F,I). Furthermore, the average population response of all *active* neurons to running with feedback was markedly reduced in APP/PS1 mice (Figure 24J). Recently, inhibitory neuron subtypes in V1 were suggested to be particularly responsive to locomotion (Fu et al., 2014).

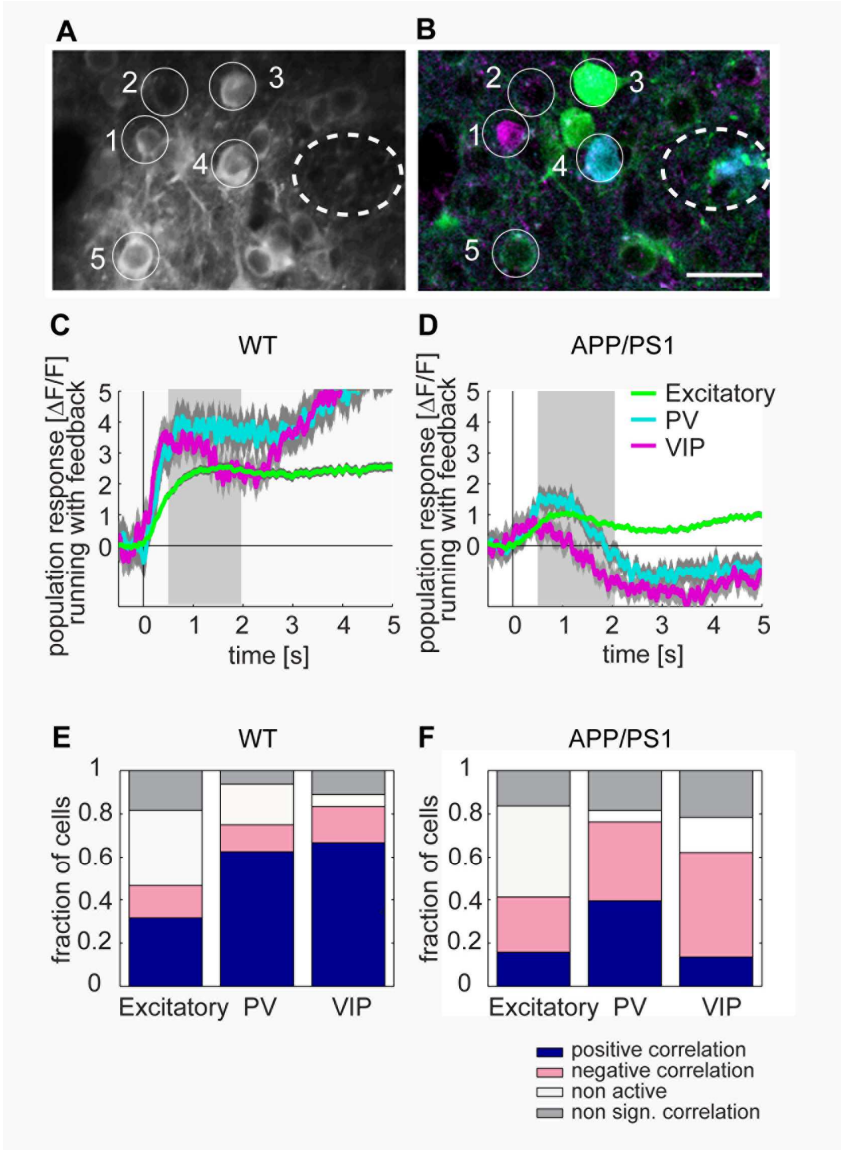

Figure 26: Immunohistochemical analysis of imaged neurons reveals functional alterations in both excitatory and inhibitory neurons in APP/PS1 mice.

*(**A**) Mean projection of an in vivo stack. Example neurons are denoted by white circles; the position of an amyloid plaque is depicted by the dashed ellipse. (**B**) Confocal image of region shown in (A). VIP expressing neurons are pseudocoloured in magenta (cell 1), PV positive neurons in cyan (cell 4) and putative excitatory neurons are shown in green (cells 2, 3, 5). (**C-D**) Cell type - specific average population response upon running onset in WT (C) and APP/PS1 mice (D, Student's t – test for the difference of the area under the curve (0.5 – 2 sec after onset (gray box)), excitatory neurons: $P < 10^{-47}$, PV neurons: $P < 10^{-11}$, VIP neurons: $P < 10^{-12}$, strongly driven by running with feedback were 96/665 of the re-identified excitatory; 3/16 PV+ and 5/18 VIP+ neurons in 3 WT mice and 68/1154 excitatory, 6/38 PV+, 2/37 VIP+ neurons in 6 APP/PS1 mice. (**E-F**) Cell type - specific distributions of neuronal fractions based on their correlation with running velocity in WT (E) and APP/PS1 mice (F, Fisher's exact test, fraction positively correlated: excitatory neurons $P < 10^{-14}$, PV $P = 0.14$; VIP $P < 10^{-3}$; fraction negatively correlated: excitatory neurons $P < 10^{-7}$, PV $P = 0.11$; VIP $P = 0.037$). Reprinted from Current Biology with permission from Elsevier (Liebscher et al., 2016).*

We hence performed post-hoc immunohistochemical stainings of neurons imaged *in vivo,* probing for the two main inhibitory subtypes reportedly being driven by locomotion, i.e. parvalbumin (PV) and vasoactive intestinal peptide (VIP) expressing neurons ((Fu et al., 2014), Figure 26A,B). We found strong motor-related population responses not only in putative excitatory (that is PV and VIP negative neurons), but also in PV and VIP expressing interneurons in WT mice. Motor-related responses were reduced in APP/PS1 mice in all three cell types (Figure 26C,D).

We next asked whether the reduced activity during running with feedback in APP/PS1 mice was caused by an impairment of the responses to visual input or to running. To disentangle the contribution of both response types, we recorded neural activity during a playback session, in which the visual flow pattern of the previous feedback session was re-played in an open loop configuration with running velocity now uncoupled from visual flow. Visually driven responses were assessed during stationary phases in the playback session. Running-related responses, on the other hand, were probed in a dark session, in which all visual input was removed. We found that the fraction of neurons strongly driven by playback was significantly smaller in APP/PS1 mice (Figure 24G,K). Moreover, the average population responses to both playback and to running in the dark were reduced in APP/PS1 mice (Figure 24L,N). These differences were not attributable to differences in running velocity (Figure 27).

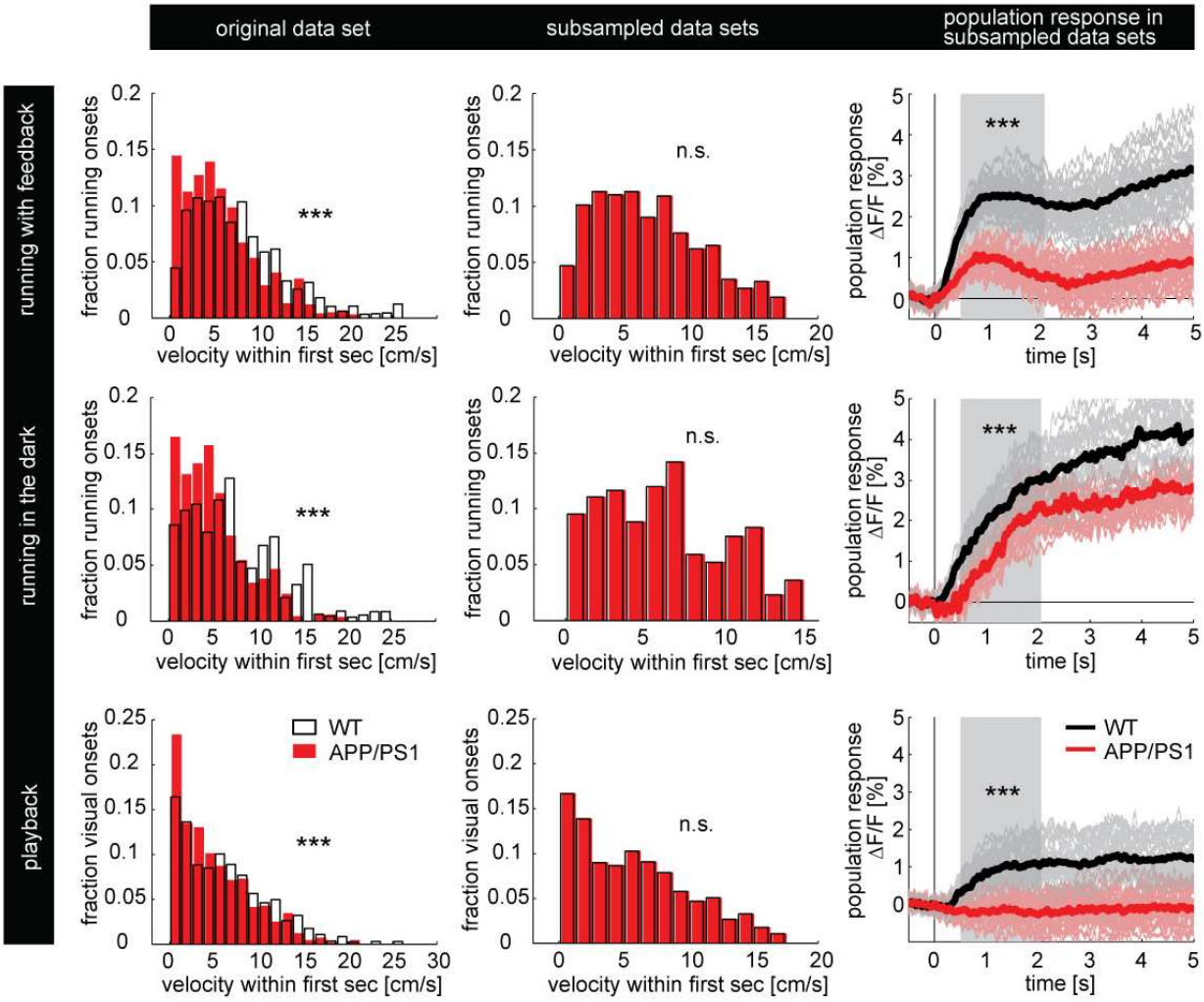

Figure 27: Differences in running speed and virtual playback velocity between genotypes do not account for difference in average population response.

*Distribution of average velocity within the first second of running with feedback, running in the dark and playback in original data set (first column; running with feedback in WT 6.72 [3.28; 10.97] cm/s and in APP/PS1 4.86 [2.36; 8] cm/s, P < 0.001; running in the dark: WT 6.45 [3.28; 10.97] cm/s and in APP/PS1 4.14 [1.99; 6.86] cm/s, P < 0.001; playback (virtual velocity): WT 5.4 [2.1; 8.85] cm/s and in APP/PS1 3.76 [1.4; 7.27] cm/s, P < 0.001, all rank sum tests, data are median [interquartile range]). To control for behavioural differences between WT and APP/PS1 mice, average neural responses were measured on a subset of behaviourally matched trials. To this end the original distribution of running onset speeds of APP/PS1 and WT mice was resampled to match the distribution of WT mice (second column). The average population response of the subsampled data set for the respective stimulus conditions was significantly reduced in APP/PS1 compared with WT mice (third column; bootstrapped difference of the area under the curve (AUC, 0.5 – 2 sec upon respective onset, (gray box)). Thin gray (WT) and red (APP/PS1) lines depict population response of single iterations. Thick lines represent average of 100 bootstrap iterations. *** P < 0.001. Reprinted from Current Biology with permission from Elsevier (Liebscher et al., 2016).*

4.3.2. Characterization of visually driven responses in V1 of APP/PS1 mice

Visual stimulation induced by playback of the previously generated visual flow was restricted to only one direction of motion and consisted of rather low temporal frequencies (average within first second after onset: 0.7 [0.01; 1.72] Hz, data are median [interquartile range] of all playback onsets), essentially resulting in a suboptimal stimulation of neurons in V1 of awake mice (Andermann et al., 2011). To more comprehensively quantify visually-driven responses, we recorded neural responses to conventional grating stimuli moving in 8 different directions at a temporal frequency of 2 Hz (Figure 28). These analyses further substantiated our findings of reduced responsiveness to visual stimuli (Figure 28A-C) and also demonstrate that visual responses were enhanced less strongly by locomotion in APP/PS1 mice (Figure 28D,E). Tuning properties, such as orientation (orientation selectivity index (OSI), Figure 13F) – and direction selectivity (direction selectivity index (DSI), Figure 28G) as well as tuning bandwidth (WT: 27.7° ± 0.98°; APP/PS1: 27.8° ± 1.27°; rank sum test, $P = 0.84$, data are mean ± SEM), however, did not differ significantly between WT and APP/PS1 mice (Figure 28F-H). Together, these data indicate that the reduced responsiveness to running with visual feedback in APP/PS1 mice may be based on an impairment of both neuronal circuits, those conveying visual signals and those providing information about running velocity.

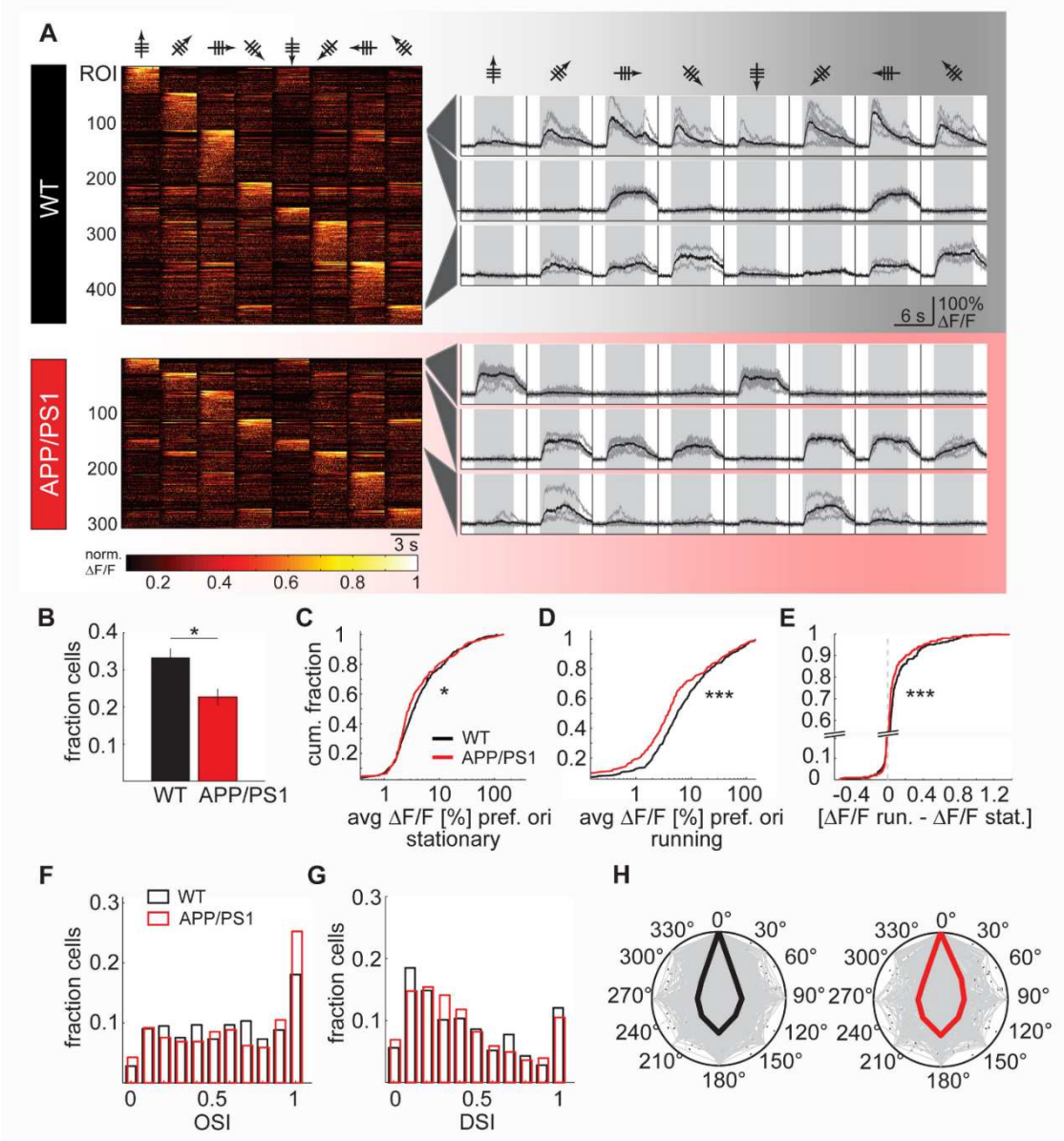

Figure 28: Neuronal responses to moving gratings.

*(**A**) Heat maps depicting normalized neuronal responses to stimulation with moving gratings, sorted by preferred direction and response magnitude in WT and APP/PS1 mice. Representative neuronal traces are shown. Gray areas mark epochs of moving grating stimulation, preceded by the presentation of standing gratings. (**B**) Fraction of cells in each experiment that were strongly driven by visual stimulation in WT and APP/PS1 mice (rank sum test, P = 0.028, WT n = 21, APP/PS1 n = 22). (**C**) Cumulative distribution of average responses (ΔF/F) of visually driven cells at the preferred orientation during stationary periods (KS test, P = 0.039, WT n = 465 neurons, APP/PS1 n = 305 neurons). (**D**) Cumulative distribution of average responses of visually driven neurons at the preferred orientation during running (KS test, $P < 10^{-3}$; WT n = 361 neurons, APP/PS1 n = 297 neurons). (**E**) Cumulative distribution of the difference between responses to visual stimulation during running and stationary epochs for visually driven neurons (KS test, $P < 10^{-3}$, WT n = 361 neurons, APP/PS1 n = 297 neurons). (**F,G**) Distribution of orientation selectivity index (OSI, F) and direction selectivity index (DSI, G) of neuronal responses during stationary periods (KS test, P = 0.06 and P = 0.46; WT n = 465 neurons, APP/PS1 n = 305 neurons). (**H**) Average tuning of visually driven neurons normalized to preferred orientation (0°; WT n = 465 neurons, APP/PS1 n = 305 neurons). Data in (B) are mean ± SEM. Reprinted from Current Biology with permission from Elsevier (Liebscher et al., 2016).*

4.3.3. Pupillary response to locomotion

Which mechanisms might underlie the observed reduction of visual – and motor related responses? There is increasing evidence for an involvement of neuromodulatory inputs in driving locomotion-related neuronal activity in V1, in particular for acetylcholine and noradrenaline (NA) (Fu et al., 2014; Polack et al., 2013). Reduced responses in APP/PS1 mice could hence be based on neuromodulatory deficits, which are characteristic for AD patients (Bondareff et al., 1987; German et al., 1992; Haglund et al., 2006; Matthews et al., 2002). A simple means of probing neuromodulatory function in behaving animals is tracking the pupil diameter (Erisken et al., 2014; Samuels and Szabadi, 2008a, b). In fact, we observed indirect evidence for a functional noradrenergic deficit, when we analysed pupil size in feedback sessions. APP/PS1 mice showed strongly reduced pupil diameters (Figure 29A,B), similar to what has been observed in AD patients (Bitsios et al., 1996; Prettyman et al., 1997). Recent studies have demonstrated that locomotion and even short periods of brain state changes during quiescence are associated with pupil dilation, most likely mediated by noradrenergic inputs (Erisken et al., 2014; Polack et al., 2013; Reimer et al., 2014). The locomotion - associated pupillary response, consisting of dilation and a ventronasal shift of the pupil, however, was still preserved in APP/PS1 mice (Figure 29C-H). Our findings are thus in line with previous studies reporting an impairment of the noradrenergic system in AD mouse models (Francis et al., 2012; German et al., 2005; O'Neil et al., 2007).

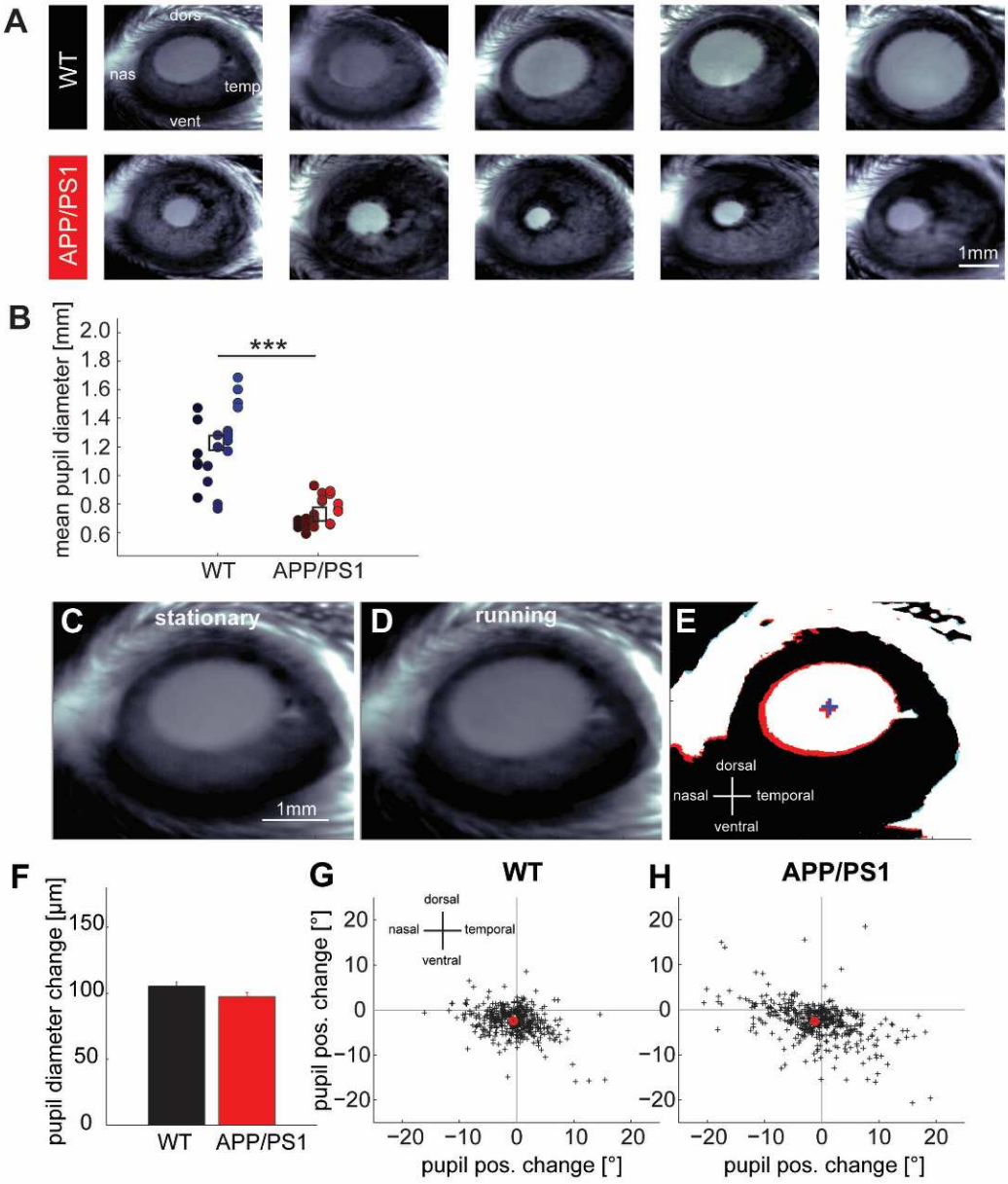

Figure 29: Average pupil size.

*(**A**) Representative snapshot of the left eye during a stationary period of WT (upper panel) and APP/PS1 mice (lower panel). (**B**) Average pupil diameter. Colour reflects mouse identity and each data point depicts a single experiment. Squares denote the group mean. Student's t-test, $P < 10^{-9}$. (**C**) Mean projection of a representative pupil recording encompassing 1 second preceding each running onset. (**D**) Mean projection of 2 seconds after each running onset. (**E**) Superposition of binary images depicting average eye position preceding (light blue) and following (red) running onsets. Crosses denote position of pupil center during respective behavioural state (blue – stationary, red – running). (**F**) Locomotion-associated difference in pupil diameter in WT (black) and APP/PS1 mice (red) (Student's t-test, P = 0.09). (**G,H**) Change of pupil position upon running in (G) WT and (H) APP/PS1 mice (WT: nasal 0.53 ± 0.17°, ventral 2.2 ± 0.11°, APP/PS1: 1.5 ± 0.29 °, ventral 2.4 ± 0.19°, rank sum test, nasal shift P = 0.021, ventral shift P = 0.61). Red circle represents average position. All data are mean ± SEM. nas - nasal, temp – temporal, ven – ventral, dors – dorsal. Reprinted from Current Biology with permission from Elsevier (Liebscher et al., 2016).*

4.3.4. Sensorimotor mismatch response in primary visual cortex

Normal function of neural networks not only hinges on undisrupted input but also on a correct integration of different input streams. A signal that is based on the integration of motor-related and visual signals in mouse V1 is the sensorimotor mismatch response (Keller et al., 2012). A mismatch response is elicited by a difference between actual and *expected* visual flow, caused by brief perturbations of the visual flow during running (Keller et al., 2012). Surprisingly, we found that despite a marked reduction in the responsiveness to both, motor and visual input, sensorimotor mismatch signals were spared in APP/PS1 mice (Figure 30A,B). The fraction of neurons strongly driven by perturbations of visual flow did not differ between WT and APP/PS1 mice (Figure 30C). The mean population response in APP/PS1 mice even exhibited a slight increase in the mismatch response (Figure 30D). As the mismatch response depends on the running velocity at the time of perturbation (Keller et al., 2012), we analysed the tuning of the mismatch signal with respect to the running speed of the mouse and found no significant difference between genotypes (Figure 30E).

Immunohistochemical analyses revealed that both excitatory and inhibitory cells (VIP, PV expressing) were strongly driven by sensorimotor mismatch (mismatch cells in WT: 18 excitatory, 5 PV and 7 VIP out of 30 re-identified mismatch cells in 3 mice; in APP/PS1: 37 excitatory, 11 PV and 2 VIP out of 50 re-identified mismatch responsive cells in 6 mice). Despite the maintenance of the mismatch response in excitatory and PV positive neurons, we observed a strong reduction in responsiveness in VIP interneurons (Figure 31A-G). Nevertheless, in contrast to the strong reduction in motor - related responses in APP/PS1 mice, these data argue for a particular resilience of the mismatch signal.

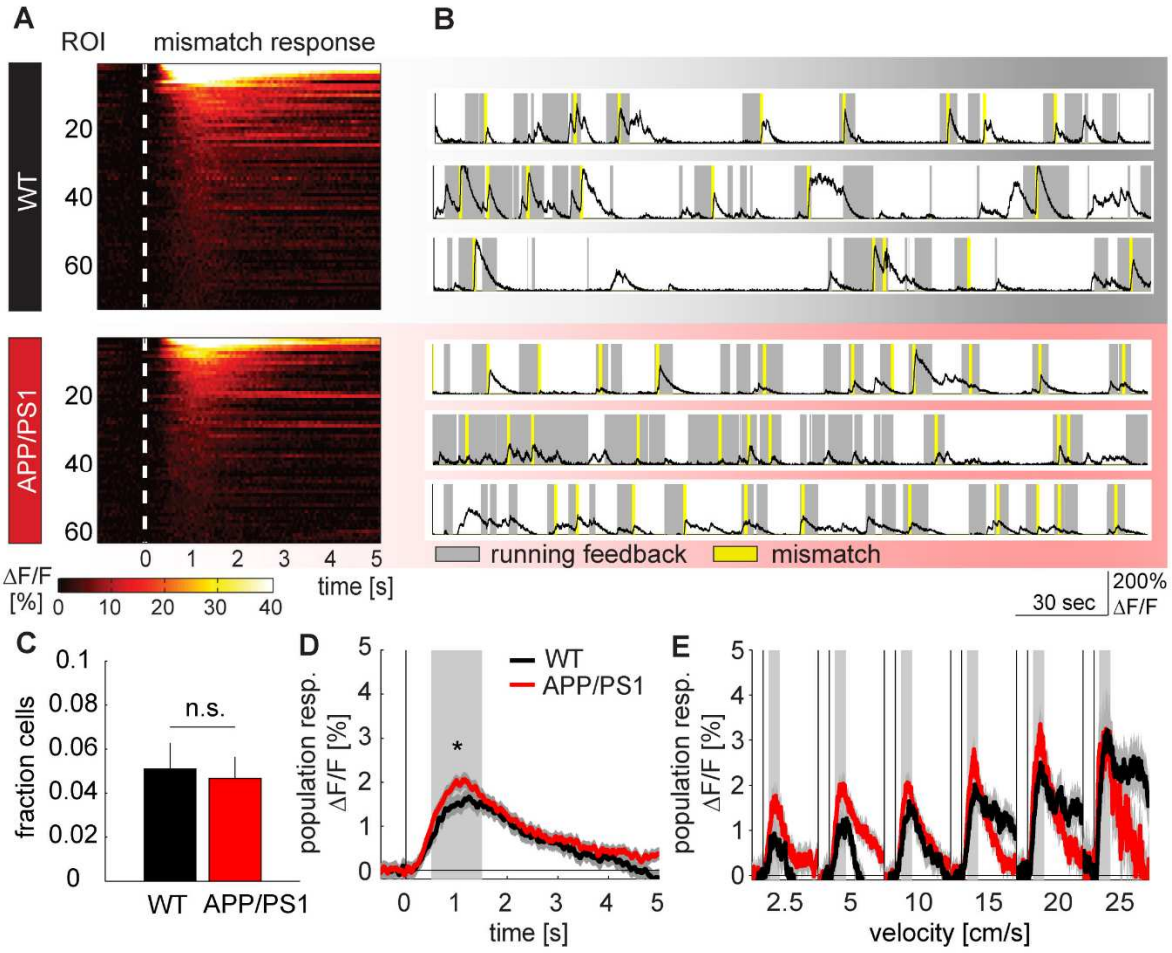

Figure 30: Sensorimotor mismatch response is spared in APP/PS1 mice.

*(**A**) Heat maps depicting average activity to sensorimotor mismatch of neurons strongly driven by mismatch, sorted by response magnitude for both genotypes. (**B**) Example calcium traces demonstrating neuronal activity elicited by sensorimotor mismatch (gray areas mark periods of running with visual feedback, yellow lines depict brief halts of visual flow, reflecting sensorimotor mismatch). (**C**) Fraction of neurons strongly driven by mismatch in each experiment does not differ between genotypes (rank sum test, P = 0.91, WT n = 21, APP/PS1 n = 22). (**D**) Average mismatch response of the population (area under the curve between 0.5-1.5 seconds after mismatch onset (gray box), Student's t-test, P = 0.017). (**E**) Tuning of the population mismatch response at different running velocities at time of mismatch onset (analysis of covariance for area under the curve values in each velocity bin, F(1,40890) = 0.5, P = 0.48). Data in (C) are mean ± SEM, ROI - region of interest, * P < 0.05. Reprinted from Current Biology with permission from Elsevier (Liebscher et al., 2016).*

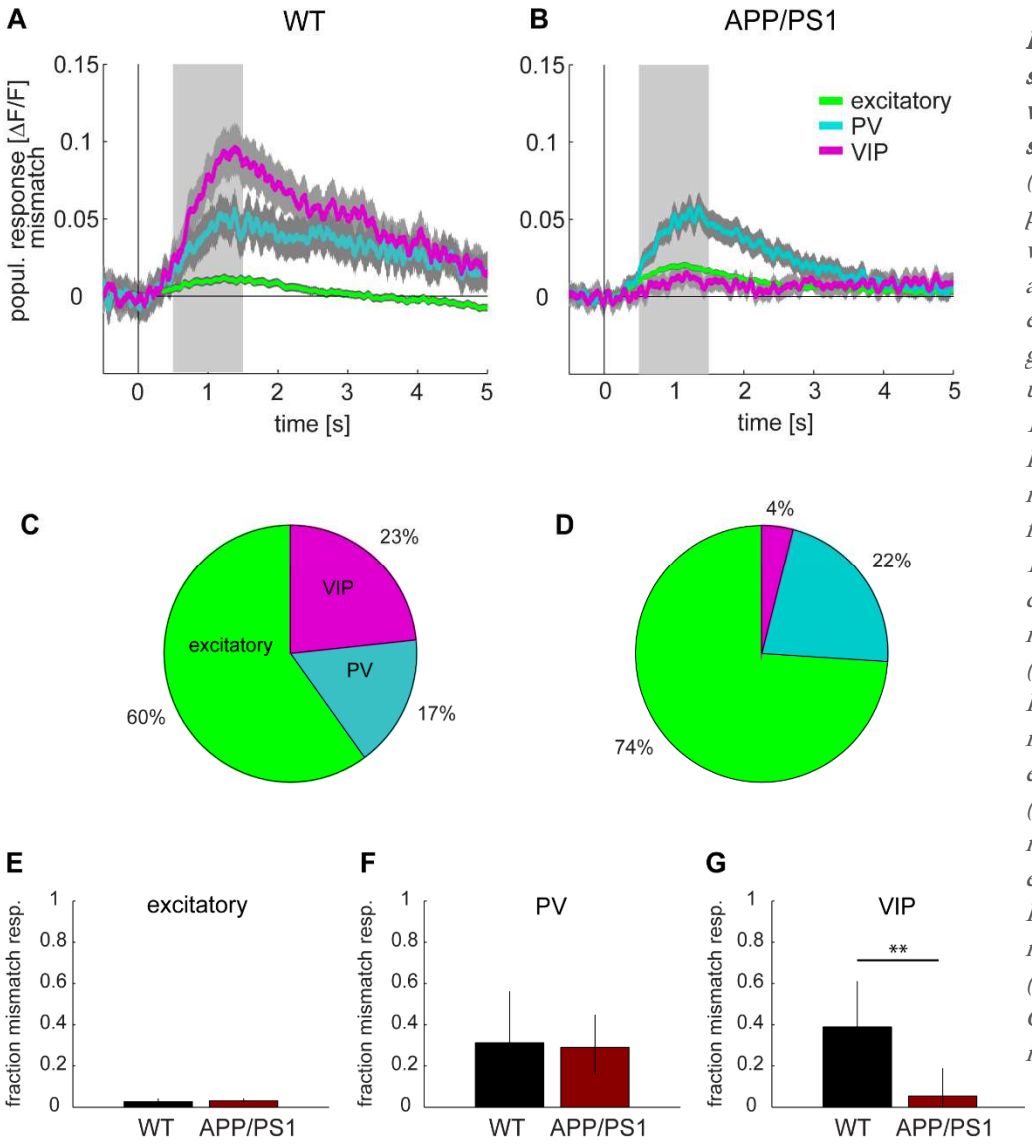

Figure 31: Cell type - specific contribution to the visuomotor mismatch signal.

(A) Cell type – specific population response to visuomotor mismatch in WT and (B) in APP/PS1 mice for excitatory neurons (shown in green, rank sum test for area under the curve between 0.5-1.5 sec after mismatch onset, P = 0.035, for PV positive neurons (blue trace) P = 0.44, for VIP positive neurons P < 10^{-6}). (C) Contribution of different cell types to the mismatch signal in WT and (D) in APP/PS1 mice. (E) Fraction of mismatch responsive cells amongst excitatory neurons in WT (black) and APP/PS1 (red) mice (Fisher's exact test, for excitatory neurons P = 0.67, PV neurons P = 0.99, VIP neurons P = 0.003). Data in (A,B) are mean ± SEM, in (E-G) mean ± 95% confidence interval of the mean.

4.3.5. Aberrant neuronal activity in V1 of APP/PS1 mice

AD is characterized by alterations of neuronal structure, such as spine instability, spine loss and neuritic dystrophies (Liebscher and Meyer-Luehmann, 2012; Liebscher et al., 2014; Spires-Jones et al., 2007), which affect neuronal connectivity. To test if this in turn reduces the precision and reliability of neuronal responses, we probed the correlation of neuronal activity with running velocity in feedback sessions (Figure 32A-C). In addition to an overall increase in the number of silent cells during feedback conditions (average fraction of silent cells per experiment WT: 0.32 ± 0.03, APP/PS1: 0.41 ± 0.03, rank sum test, $P = 0.015$) and consistent with a reduced population response and a lower fraction of neurons responsive to running with feedback

(Figure 24G,H), we observed a strong reduction in the fraction of neurons positively correlated with running (Figure 32A,B) and a decrease of the strength of this correlation (Figure 24C) in APP/PS1 mice. We also noticed that a significant fraction of neurons was predominantly active during quiescent periods (Figure 24E, ROIs 5 and 6). In WT mice these quiescent periods are characterized by low levels of neuronal activity (Keller et al., 2012). In order to quantify these presumably aberrantly active cells in APP/PS1 mice, we analysed the fraction of neurons negatively correlated with running speed.

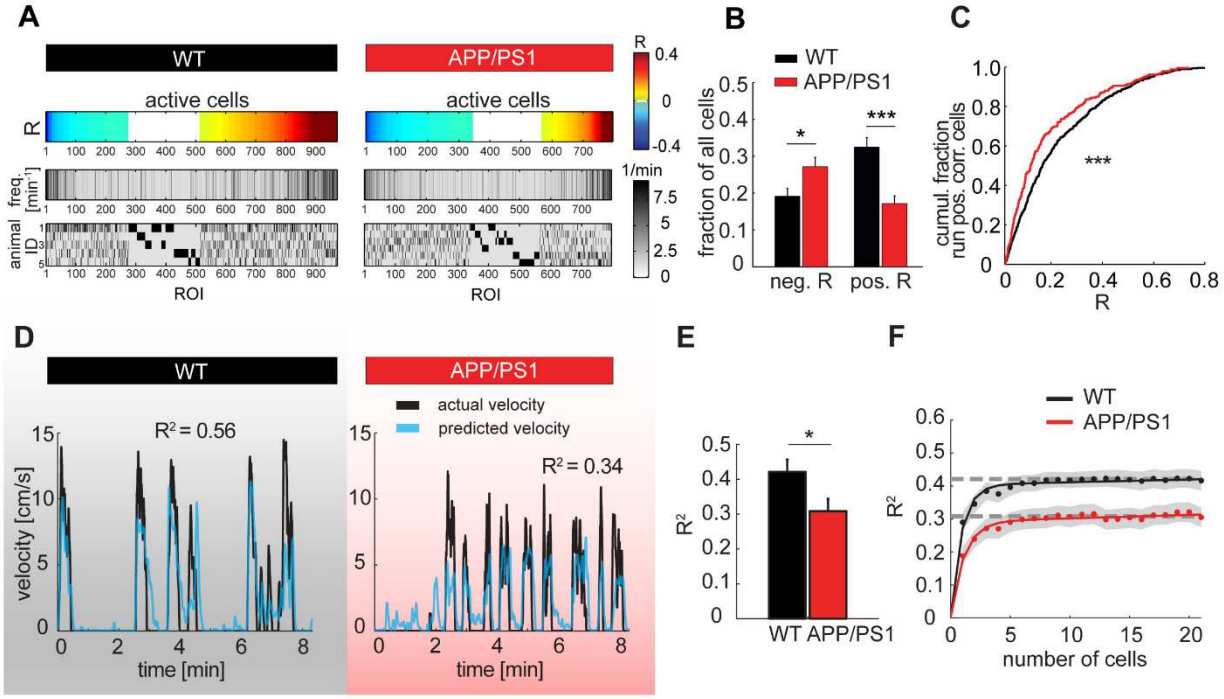

Figure 32: Aberrant neuronal activity in awake APP/PS1 mice and impact on decoding accuracy of V1 neurons. *(A) Distribution of Pearson's correlation coefficient (R) for the correlation of neuronal activity and running velocity in the feedback sessions. Aligned to the R values are the respective frequencies of calcium events and the animal ID. (B) Fraction of neurons negatively or positively correlated with running (Student's t-test, negatively correlated: P = 0.019; positively correlated: P = 4.6 x 10^{-5}, WT n = 21, APP/PS1 n = 22). (C) Cumulative distribution of correlation coefficients of neurons positively correlated with running in APP/PS1 (red) and WT mice (black, KS test, P = 0.0008, WT n = 459, APP/PS1 n = 231) (D) Running velocity predicted by random forest classifier based on neuronal activity. Actual running velocity in an example feedback session (black trace) overlaid with the velocity predicted by the model (blue trace) for WT and APP/PS1 mice. (E) Correlation between actual and predicted velocity is lower in APP/PS1 mice (Student's t-test, P = 0.014, WT n = 21, APP/PS1 n = 22). (F) Decoding performance as a function of the number of cells used to train the classifier. Cells were successively added to the algorithm ranked by the correlation of their activity and running velocity (dashed lines: mean R^2 ± SEM). The number of cells needed to reach saturation of decoding performance did not differ between genotypes (6 neurons per experiment). Data in (B, E) are mean ± SEM, * P < 0.05, *** P < 0.001. Reprinted from Current Biology with permission from Elsevier (Liebscher et al., 2016).*

Indeed, we observed a significantly higher fraction of neurons in APP/PS1 mice negatively correlated with running and hence predominantly active during quiescent periods both in feedback sessions (Figure 32A,B) and in the dark (fraction of neurons negatively correlated with running in the dark: WT: 0.09 ± 0.01, APP/PS1: 0.14 ± 0.01, $P = 0.0013$; positively correlated: WT: 0.25 ± 0.03, APP/PS1: 0.19 ± 0.01, $P = 0.1$, both Student's *t*-test, data are mean ± SEM), an effect that was observed both in excitatory and inhibitory cells (Figure 26E,F). These spontaneously active cells exhibited reduced neuronal activity during running compared to stationary episodes in both genotypes (Figure 33A-C, linear regression of average neuronal response during running as function of average response during stationary periods in running negatively correlated neurons: (A) WT $f(x) = 0.67x + 0.003$, $P < 10^{-3}$; (B) APP/PS1 $f(x) = 0.46 + 0.0003$, $P < 10^{-4}$). However, the degree to which the activity of spontaneously active cells was suppressed during running was significantly higher in APP/PS1 mice (Figure 33C, difference in average neuronal activity (mean $\Delta F/F$) during stationary epochs and during running: WT 0.053 ± 0.01; APP/PS1 0.072 ± 0.009, $P < 10^{-5}$, rank sum test, data are mean ± SEM). These data suggest that motor-elated inputs into V1 are sufficient to silence those aberrantly active cells, indicating that their functional integrity is not entirely lost.

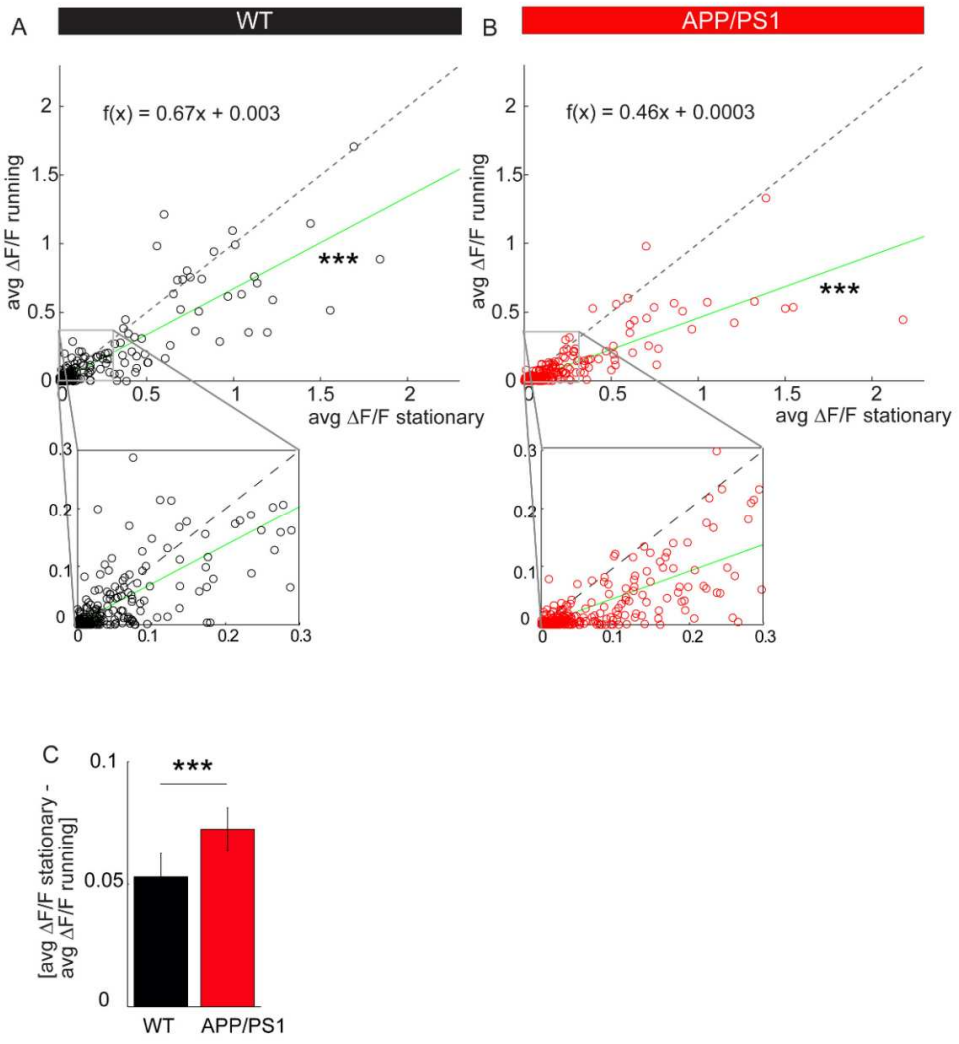

Figure 33: Locomotion suppresses activity of running negatively correlated cells more strongly in APP/PS1 mice. *(A,B) Spontaneously active cells (negatively correlated to running) exhibit less activity during running periods in (A) WT and in (B) APP/PS1 mice. Each circle depicts the average activity during stationary and running periods of a neuron negatively correlated to running. Green line represents the linear regression (WT: $P < 10^{-3}$, APP/PS1: $P < 10^{-4}$). Dashed lines represent the unity line. Insets show a higher magnification of ΔF/F values below 0.3. The slope of the linear regression in APP/PS1 mice is significantly smaller compared to WT mice ($P < 10^{-11}$, Analysis of covariance). (**C**) The difference between average activity during stationary periods and running periods is significantly higher in APP/PS1 ($P < 10^{-5}$, rank sum test).*

We again probed for a relationship between plaque distance and a cell's correlation with locomotion, but did not find a difference in average distance to the nearest plaque between neurons positively or negatively correlated with locomotion (Figure 25E). Given the higher fraction of neurons negatively correlated with running and reports on epileptiform discharges in AD transgenic mice (Palop and Mucke, 2010; Verret et al., 2012), we next sought to investigate whether this aberrant activity occurs in a synchronized fashion. We thus computed pairwise neuronal correlations during quiescence and during locomotion. In line with a recent study (Erisken et al., 2014) we found that locomotion led to a slight reduction of the pairwise correlation of neuronal activity in WT mice (stationary: R = 0.065 ± 0.0014, locomotion: R = 0.053 ± 0.0016, data are mean ± SEM, rank sum test, $P < 10^{-44}$; data not shown). To our surprise we observed that during quiescence the average pairwise correlations of neuronal activity, was significantly higher in WT compared to APP/PS1 mice

(WT: R = 0.065 ± 0.0014, APP/PS1: R = 0.037 ± 0.0016, data are mean ± SEM, rank sum test, $P < 10^{-63}$, data not shown). To assess whether neurons that were predominantly active during quiescence, exhibit synchronous activity, we measured the pairwise correlation of running-negatively correlated neurons during quiescence and did not observe any significant difference between WT and APP/PS1 mice (WT: R = 0.04 ± 0.004; APP/PS1: R = 0.034 ± 0.0029, rank sum test, $P = 0.13$, data not shown). Together these data indicate that the observed aberrant activity during quiescent states in APP/PS1 mice does not manifest in increased pairwise neuronal correlations and likely reflects uncorrelated noise.

Finally, having shown that behaving APP/PS1 mice exhibit aberrant patterns of neuronal activity we asked whether this affects the ability to decode running velocity from network activity. To address this question, we employed a machine learning algorithm (Random Forests Model) that was trained to decode running velocity based on neuronal activity. We indeed found the average decoding performance to be significantly reduced in APP/PS1 compared to WT mice (Figure 32E,F). To exclude that differences in overall activity levels between genotypes result in poorer decoding accuracy, we subsampled experiments in WT and APP/PS1 mice to match the distribution of the fraction of active cells observed in APP/PS1 mice and found that this could not explain differences in decoding performance (mean cross validation (R^2) in WT: 0.44 ± 0.01, in APP/PS1: 0.31 ± 0.01, mean ± std, Student's t – test, $P < 10^{-140}$).

To assess the number of cells necessary to reach saturation of decoding performance, we trained the algorithm on individual cells in each experiment and ranked all cells based on their decoding accuracy. We then decoded running velocity by adding neurons successively, starting with the neuron that yielded the best performance of the classifier, followed by the combination of the best and the 2nd best neuron and so forth. The number of cells needed to reach saturation of decoding performance did not differ between genotypes (Figure 32F). These data hence demonstrate that the representation of running velocity is less stable in visual cortex of APP/PS1 mice.

The reduced reliability of neuronal activity (Figure 32A-C) in concert with increased uncorrelated spontaneous activity may represent a general feature of AD pathology, likely affecting diverse neuronal circuits in AD.

5 DISCUSSION

Alzheimer's disease is considered to represent a synaptopathy – a defect of the communication sites between neurons. Little is known about the actual nature of this synaptic defect as well as its consequences on the function of single neurons and neuronal networks. To address these questions, I investigated both structural and functional alterations on cortical neurons in a mouse model of Alzheimer's disease.

5.1. Synaptic alterations in Alzheimer's disease

From autopsy cases it had been known that the synaptic density in cortex and hippocampus of AD patients is strongly reduced compared to healthy age matched controls (Masliah et al., 1991; Scheff and Price, 2006; Terry et al., 1991). In order to monitor the dynamics of synaptic structures *in vivo* we employed two-photon *in vivo* imaging of AD transgenic (APP/PS1+/- x GFP+/-) mice at an age of three-four months over four consecutive weeks at seven day intervals. At that age APP/PS1 mice have already deposited a considerable amount of amyloid plaques in cortex, as deposition starts around two months of age.

5.1.1. Amyloid plaque - associated effects on dendritic spines

Dendritic spines represent structural correlates of postsynapses, and learning and memory processes are associated with a growth and stabilization of dendritic spines (Engert and Bonhoeffer, 1999). This notion was further supported by evidence for a causal relationship between the formation of long-term memories and the generation of long-lived synapses in cortex as witnessed by chronic in vivo imaging (Xu et al., 2009; Yang et al., 2009). In order to characterize synaptic pathology in AD, we chronically monitored dendritic spines in cortex of APP/PS1 mice. In line with recent publications (Bittner et al., 2012; Spires et al., 2005; Tsai et al., 2004), reviewed by (Liebscher and Meyer-Luehmann, 2012) our analyses revealed a drop in spine density in APP/PS1 mice in the immediate vicinity of the proteinaceous amyloid deposits. In fact, this drop was only significant up to 15 µm away from the plaque border. Spine density throughout the course of the four-week imaging period, however, remained stable. These results indicate that the spine loss observed close to plaques must have occurred at an earlier time point, after which spine density stabilized again. This scenario is supported by a recent publication in which spine loss followed after plaque formation, but spine density close

to plaques in aged APPPS1 mice is not different from that in young mice (Bittner et al., 2012). Plaques were shown to increase in size by both a simple size expansion (Burgold et al., 2011; Hefendehl et al., 2011) as well as a clustering of smaller new plaques that appear in the vicinity of already existing ones, which fused to form a bigger aggregate over time (McCarter et al., 2013). As I could show that spines are lost in a narrow halo surrounding plaques, the slow but steady growth of those aggregates over time might result in a progressive global loss of spines.

Importantly, I found that dendritic spines close to amyloid plaques were highly instable as both their formation and elimination rates were almost twice as high compared to spines further away (> 50µm) from plaques or spines in WT mice. Elimination and formation rates of spines were increased to the same degree, thereby not affecting spine density. Moreover, even persistent spines considered to stably encode information varied in size more strongly over time than their counterparts in WT mice. As spine size correlates well with synaptic strength (Harris and Stevens, 1989; Kasai et al., 2010; Knott et al., 2006) these fluctuations indicate synapse instability even of those structures believed to represent solid and stable contacts. Notably, synaptic instability was evident in a much larger region as spine loss was, thereby indicating that the impact on spines is in fact much more widespread than previously thought based on histological analyses. Given the importance of the stabilization of newly formed synapses for the formation of long-term memories, highly instable synapses represent a conceivable correlate of the decline in memory function and cognition typical of AD.

A pronounced instability of synaptic structures in cortex as observed by an increased turnover rate has recently been demonstrated in other neurodegenerative diseases, such as Huntington's disease (Murmu et al., 2013), neurodevelopmental disorders, like Fragile X Syndrome (Cruz-Martin et al., 2010; Pan et al., 2010) and also during normal aging (Grillo et al., 2013; Mostany et al., 2013). Together, these studies stress the causal relevance of synaptic instability in neurodegenerative diseases and indicate that synaptic stability in turn serves as a sensitive marker for neuronal health. The underlying mechanisms causing synapse instability, however, are not well understood and can in fact be manifold. Notably, in AD many pathological features are closely tied to the peri-plaque area, such as dystrophic neurites (Meyer-Luehmann et al., 2008; Tsai et al., 2004), hyperactive neurons (Busche et al., 2008) and calcium overloaded dendrites and spines (Kuchibhotla et al., 2008). Spines on calcium-overloaded dendrites lack an important prerequisite for synaptic integration, namely functional compartmentalization (Kuchibhotla et al., 2008). Given these plaque proximity - linked

effects on neurons and dendritic spines, it is conceivable that cellular and molecular alterations within this microenvironment are causal to the synaptic pathology in AD. Amyloid plaques are composed not only of fibrillar forms of the amyloid beta peptide but, in addition, represent a reservoir of soluble Aβ oligomers (Koffie et al., 2009). Oligomers are believed to represent the toxic 'bioactive' moiety (Benilova et al., 2012; Haass and Selkoe, 2007), and have been proposed to interact directly or indirectly with synaptic components (Prion Protein C (Dohler et al., 2014; Lauren et al., 2009; Um et al., 2013; Um et al., 2012), NMDA-receptors (Texido et al., 2011), paired immunoglobulin-like receptor B (PirB) (Kim et al., 2013) etc.) thereby triggering receptor internalization, inducing LTD, spine loss and causing behavioural deficits (Kim et al., 2013; Selkoe, 2002; Shankar et al., 2007; Shankar et al., 2008; Walsh et al., 2002). Apart from the local high concentration of Aβ oligomers, another mechanism potentially causing synapse loss near plaques is the mere physical disruption of synaptic contacts by the deposited protein aggregates.

The plaque microenvironment is also characterized by the accumulation of activated glia cells, such as microglia and astrocytes. Both cell types can phagocytose cellular material and are associated not only with the removal of synapses (Chung et al., 2015a; Chung et al., 2015b; Sokolowski and Mandell, 2011) but also with the modification of synaptic strength (Bernardinelli et al., 2014; Tremblay et al., 2010). Bernardinelli et al. demonstrated that synaptic stability is associated with an increased coverage of spines by periastrocytic processes, an effect that is dependent on synaptic activity (Bernardinelli et al., 2014). Activated astrocytes possess strongly thickened processes and may hence lose their intimate relationship with spines, thereby not being able to stabilize them any longer. Further credence to the notion of neuroinflammatory factors causing synaptic deficits is based on the finding that the complement C3 released by astrocytes can reduce spine density (Lian et al., 2015). Microglia, the macrophages of the brain, are also known to remove damaged cells and subcellular structures as well as to sculpt synaptic structures in both health and disease (reviewed by (Kettenmann et al., 2013)). Very recent evidence suggests that microglia can in fact drive synaptic impairment in disease by secreting factors or triggering contact-dependent signals and removing synapses (Chung et al., 2015b; Hong et al., 2016). Both glia cell types hence seem to serve a dual role: on the one hand they are protective as i.e. microglia can phagocytose fibrillary amyloid material, but in the face of a toxic stimulus they may not only lose their physiological role in regulating synaptic plasticity, but might directly and indirectly cause the elimination of synapses.

5.1.2. Amyloid plaque - independent effects on dendritic spines

Apart from the synaptic alterations spatially linked to the deposition of amyloid plaques, I also found evidence for altered structural plasticity on spines further away from plaques. In line with the literature (Holtmaat et al., 2005), I observed a negative correlation between spine density and turnover rate in WT mice. In contrast, in APP/PS1 mice I found a significant positive correlation between spine density and turnover rate. This effect was largely based on the fact that low density stretches in APP/PS1 mice showed a reduced turnover rate. These data may point towards a reduction in synaptic efficacy. The induction of LTP on single spines can potentiate synapses on neighbouring spines and trigger the formation of new adjacent spines under physiological conditions. This effect is known to spread over several µm along the dendrite (De Roo et al., 2008b; Engert and Bonhoeffer, 1999; Harnett et al., 2012; Harvey and Svoboda, 2007; Yuste and Bonhoeffer, 2001). In APP/PS1 mice, Aβ is increased not only within plaques but it is also present in the interstitial fluid. As soluble Aβ has been shown to disrupt LTP induction and to modify synapse composition (Lacor et al., 2007; Shankar et al., 2008; Walsh et al., 2002) its negative impact on synapses might prevent synapse cooperativity, an effect most prominently seen on dendrites bearing only a few spines as their combined synaptic input is already lower.

5.1.3. Alterations of presynaptic structures

In addition to the detrimental effects caused by Aβ interactions with postsynaptic compartments, it is very likely that presynaptic structures are affected as well. To assess the structural plasticity of presynaptic structures, I also monitored axonal boutons in the cortex of APP/PS1 mice. In accordance with the observed spine instability, I also found enhanced turnover rates of axonal boutons close to plaques. Most likely due to the high variability of the axonal bouton data, I did not observe a significant effect on the density of presynaptic structures. This is in contrast to immunohistological analyses, in which a clear loss of synaptic structures close to amyloid plaques is documented (Boncristiano et al., 2005; Dong et al., 2007). In contrast to the analyses of dendritic spines, in which case the cell identity is known, the population of neurons in the bouton dataset is likely much more heterogeneous, as I could not identify the cell-bodies from which the analysed axons originated. Based on a publication that characterized subpopulations of axons in the GFP-M mouse line (De Paola et al., 2006), I tentatively assigned the axons in my dataset to the population of intracortical axons of layer II/III/V neurons. This subpopulation of neurons, however, is still heterogeneous

and, hence, might differ significantly in their bouton density. Taken together, my data demonstrate strong fluctuations of both pre- and postsynaptic structures, changes that are confined to the peri-plaque area, but that are far more widespread than the mere loss of synapses is.

5.1.4. Impact of γ - secretase inhibition on the dynamics of synaptic structures *in vivo*

Having demonstrated the impact of amyloid plaques on synaptic structures, I next asked whether pharmacological inhibition of Aβ generation can have beneficial effects on the stability of synaptic structures. Pharmacological interference with amyloid beta production can be realized by inhibiting the two enzymes that facilitate the cleavage of Aβ, namely the β - and the γ- secretase. The caveat of this approach lies within the ubiquitous expression of those enzymes and their large number of substrates (Haapasalo and Kovacs, 2011; Wakabayashi and De Strooper, 2008). I thus employed a novel selective γ - secretase inhibitor (GSI) developed by the company ELAN, which had been proven to favor the inhibition of APP processing over the cleavage of other γ - secretase substrates (oral communication with ELAN Pharmaceuticals). Moreover, this compound (ELN 594) has the advantage of being orally administrable. The daily treatment over four weeks halted the development of plaque pathology as observed by an initial reduction in the number of newly deposited amyloid plaques and, moreover, slowed down the growth of newborn plaques over the course of the four week treatment period. Throughout the course of the treatment I observed a drop in the number of newly deposited plaques in both treated and untreated mice. This finding might in part be explained by the anti-amyloidogenic properties of Methoxy-XO4 (Cohen et al., 2009), the dye used to fluorescently label amyloid deposits *in vivo*, which was repeatedly applied 24 hours prior to each imaging session. As both, the vehicle and the GSI treated group received the same concentration of the dye, the animals in both groups should have been affected to the same degree by Methoxy-XO4, resulting in an effective underestimation of the GSI treatment effect on *de novo* plaque deposition.

Importantly, the GSI treatment resulted in a pronounced stabilization of pre- and postsynaptic structures close to plaques. A more detailed analysis of this spine stabilizing effect revealed that the strongest impact of the GSI was observed on spines further away from the plaque border than 15 µm (yet < 50 µm). Mechanistically, one could imagine that the reduction of newly generated Aβ may reduce the concentration of Aβ oligomers within and in the immediate surrounding of amyloid plaques, while already deposited

fibrillary material is not affected by the treatment. As the concentration of oligomeric Aβ falls off with a gradient from the histologically defined amyloid plaque border, it is conceivable that Aβ within the periphery of the plaque-surrounding halo, where spine instability is prominent, is cleared more rapidly once generation of new Aβ is blocked. The spine loss observed close to plaques, however, could not be reversed by the treatment, which is in line with the fact, that GSI treatment did not reduce the size of amyloid plaques.

An alternative explanation for the observed synapse stabilizing effect of the GSI is offered by very recent findings regarding the relevance of γ - secretase for the function of phagocytic cells, such as microglia (Glebov et al., 2016). As pointed out above, both microglia and astrocytes can modify synaptic strength and mediate the elimination of synaptic structures, at least in part by phagocytosis (Chung et al., 2015a; Chung et al., 2015b; Hong et al., 2016; Schafer et al., 2012; Stevens et al., 2007; Tremblay et al., 2010). The machinery facilitating the physiological process of synaptic sculpting during development and in healthy adult brains has been suggested to be dysregulated during aging and in neurodegenerative diseases resulting in synaptic degeneration and synapse loss (Hong et al., 2016; Shi et al., 2015), for review see (Chung et al., 2015b). Phagocytic function of monocytic cells including microglia is amongst others regulated by the triggering receptor expressed on myeloid cells-2 (TREM2). This receptor – like APP – is sequentially cleaved, with the last cleavage step also carried out by the γ-secretase. γ-secretase inhibition consequently reduced phagocytic activity and impaired calcium signaling in monocytic cells (Glebov et al., 2016). Assuming that synapse loss in AD is mediated at least in part through the phagocytosis of synapses by microglia and that microglia and astrocytes are strongly activated in plaque - surrounding tissue, one could speculate that the GSI treatment exerts a synapse-protective effect by inhibiting phagocytosis through attenuated TREM-2 processing. Indeed, this hypothesis is somewhat supported by recent findings of a reduced recruitment of microglia to the plaque area in AD transgenic mice deficient of TREM2 (Wang et al., 2015, Ulrich et al., 2014). As TREM2 mutations associated with neurodegenerative diseases per se affect phagocytic function of microglia (Kleinberger et al., 2014), the actual role of the phagocytic function of these brain resident macrophages throughout the course of the disease remains to be clarified.

Despite representing a powerful therapeutic approach, clinical use of GSIs has been hampered to date by its side effects. A large clinical trial probing the efficacy of Semagacestat (LY450139), an unselective GSI, had be halted prematurely due to stronger cognitive worsening and a higher incidence of skin cancer in treated patients (De Strooper, 2014; Doody et al., 2013). Moreover, an *in vivo* imaging study in which WT mice

received unselective GSIs reported a reduction in spine density (Bittner et al., 2009) that was suggested to be causally related to the stronger cognitive worsening of GSI treated AD patients. Thus, potential adverse effects of GSIs need to be carefully assessed. In this study I did not observe any effect of the GSI on spines in WT mice and in spines further away from plaques in APPPS1 mice, which essentially behaved similar to spines in WT mice, suggesting no obvious side effects of the treatment. One important γ - secretase substrate other than APP is the cell surface receptor Notch, which is not only implicated in development (Ables et al., 2011), but has recently also been shown to be crucially involved in memory formation and adult neurogenesis (Alberi et al., 2013). While earlier unselective GSIs, such as DAPT (N-[N-3,5-difluorophenacetyl-L-alanyl]-S-phenylglycine t-butyl ester), do not differentiate between the processing of APP and Notch (ratio of EC_{50} values for Notch and Aβ42: DAPT = 0.5; LY450139= 0.8 (Martone et al., 2009), ELN 594, the GSI used in this study, possesses at least a 10 fold higher selectivity for APP over Notch (communication with ELAN Pharmaceuticals). ELN 594, a sulfonamide type inhibitor, differs structurally from earlier GSIs, which may result in different pharmacokinetic and pharmacologic properties. Another caveat to bear in mind is the large number of γ - secretase substrates already known to date, amongst which are also molecules and receptors implicated in synaptic plasticity, such as EphB2 or ErbB4 (Wakabayashi and De Strooper, 2008). Interestingly, as many mutations within the presenilin gene, known to lead to familial AD, are effectively resulting in a reduction of γ - secretase activity, i.e. a loss of function, additional non-selective inhibition of the γ - secretase may result in further accumulation of unprocessed substrates relevant for synaptic function.

An approach to circumvent this problem could be based on a selective phasic inhibition of the γ - secretase, as transient γ - secretase inhibition is known to result in a subsequent overshoot of its activity (Fleisher et al., 2008; Siemers et al., 2007). A temporary predominant inhibition of APP processing, which most likely will not be fully selective, could thereby be combined with a recovery period, in which accumulated substrates may then be processed. Transient γ - secretase inhibition may be furthermore realized in a brain region-specific or circadian manner. Aβ production has been shown to be both dependent on neuronal activity (Bero et al., 2011), therefore deposition is initially seen in regions of the default mode network (Sperling 2009), and on circadian rhythm, i.e. Aβ is mainly generated during active phases of the day, i.e. at night in mice (Kang et al., 2009) and during day in humans (Huang et al., 2012; Musiek and Holtzman, 2015; Musiek et al., 2015). In order to minimize side effects, caused by the reduced processing of APP

substrates that are crucial for synaptic plasticity, one could hence attempt to selectively inhibit the enzyme within the default mode network only during daytime.

A different approach to interfere with Aβ generation is the inhibition of the β-secretase (BACE), the enzyme that facilitates the initial shedding of the APP protein. Despite considered a safe approach for many years, recent studies have unraveled, in analogy to the γ - secretase, a large number of β-secretase substrates (Hemming et al., 2009; Kuhn et al., 2012), thereby casting doubt on the usefulness of this approach. Indeed, a dose-dependent impairment of cognition, accompanied by a reduced rate of spine formation was observed after chronic administration of β - secretase inhibitors in mice (Filser et al., 2015). Nonetheless, currently BACE inhibitors are in phase III clinical trials, and the development of selective BACE inhibitors is hence heavily pursued.

Taken together, my data provide evidence for beneficial effects of selective γ - secretase inhibition on plaque-associated synaptic instability - a feature affecting a much larger area of the brain than mere spine loss - without displaying side effects on synaptic structures in WT mice and on spines and boutons further away from plaques, respectively.

5.2. Impaired information processing in primary visual cortex of APP/PS1 mice

Having demonstrated widespread amyloid plaque-associated pre- and postsynaptic instability, I investigated in a second study to what extent these structural alterations affect the response properties of single neurons and neuronal circuits. To address these questions, I chose the primary visual cortex (V1) as a model area. The primary visual cortex is endowed with a well-characterized set of neuronal response properties, such as the responsiveness to certain stimulus features, e.g. the orientation of bars and edges or their direction of motion, termed orientation and direction selectivity. In addition to visually driven responses, recent studies in behaving mice have demonstrated strong locomotion-related responses, which in turn can also modulate visual responses (Keller et al., 2012; Niell and Stryker, 2010), as well as pronounced neuronal activity elicited upon a mismatch between actual and expected self-generated visual flow (Keller et al., 2012). Importantly, visuomotor integration is also impaired in AD as an early sign of the disease (Hawkins

and Sergio, 2014; Tippett and Sergio, 2006; Velasques et al., 2011). I conducted two-photon calcium imaging, employing the genetically encoded calcium indicator GCaMP6m (Chen et al., 2013) in behaving, plaque-depositing APP/PS1 (10-11 months) and age-matched transgene negative siblings (WT) to assess different response types in the primary visual cortex applying a visual feedback paradigm. In this paradigm mice were free to run on a spherical treadmill while running velocity was fed back to control the speed of vertically orientated moving gratings presented on two screens placed in front of the mouse. This experimental setup allowed for separately probing neuronal responses to visual input, locomotion, the combination of both as well as a mismatch between actual and expected visual flow.

With this set of experiments I found evidence for both hypoactivity/hyporesponsiveness and hyperexcitability in awake AD transgenic mice. Significantly fewer cells were active at all in V1 in AD transgenic mice, irrespective of their response properties. This drop in activity was accompanied by a strong reduction in feed-forward input as seen in a pronounced decrease in visual – and motor-related signals both at the population as well as the single cell level. Despite the lower responsiveness, tuning properties of neurons in APP/PS1 mice were still comparable to WT mice as seen in a similar orientation and direction tuning. These results are at odds with a recently published study, in which an age- and hence plaque load - dependent impairment of orientation and direction tuning of neurons in V1 in an APP/PS1 mouse model was shown (Grienberger et al., 2012). The differences potentially result from the different experimental conditions, as Grienberger et al. conducted their experiments in anesthetized mice, employing the synthetic calcium indicator Oregon Green BAPTA-1 (OGB-1). Moreover, experiments using OGB-1 are performed acutely, i.e. shortly after the craniotomy and the dye injection is performed. Conversely, experiments employing virus-mediated expression of genetically encoded calcium indicators are performed 3-4 weeks post-injection and window implantation, allowing for ample recovery time from the surgery and hence from potential tissue damage.

Apart from these discrepancies earlier *in vivo* calcium imaging studies in AD transgenic mice also found a strong increase in the fraction of non-active cells (Busche et al., 2008; Grienberger et al., 2012). What might cause this hypoactivity/hyporesponsiveness? Visual responses in V1 are primarily driven by excitatory feed-forward inputs from the lateral geniculate nucleus and shaped by top-down and lateral inputs (Harris and Mrsic-Flogel, 2013; Petro et al., 2014). The circuitry underlying motor - related responses in V1, however, is less well understood and is currently object of investigation (Fu et al., 2014; Lee et al., 2014). The fact that both

visual and motor-related circuits, which rely on very different neuronal connections, are jointly affected, argues for a general AD-associated impairment of information processing, which may be based on impaired long-range connectivity. Indeed, a disruption of resting state functional connectivity between multiple brain areas has been described in AD patients (Buckner et al., 2009; Liu et al., 2014) and in APP/PS1 mice (Bero et al., 2012). Changes in white matter integrity in AD have also been reported using diffusion tensor imaging in patients (Nir et al., 2013; Zhan et al., 2015) and animal models of the disease (Qin et al., 2013; Shu et al., 2013). Probably the most parsimonious explanation for the impaired connectivity is based on the well-characterized structural neuronal alterations accompanying the disease process, such as the instability and loss of synapses as well as the formation of dystrophic neurites shown in my first study (Koffie et al., 2011; Liebscher and Meyer-Luehmann, 2012; Liebscher et al., 2014; Spires-Jones et al., 2007).

5.2.1. Potential mechanisms of gain modulation in V1

The gain of neuronal responses is in addition regulated by neuromodulatory systems, such as noradrenergic or cholinergic inputs, a mechanism which is also prominent for both excitatory and inhibitory neurons in V1 (Polack et al., 2013). While noradrenergic inputs have been shown to depolarize the resting membrane potential and reduce its variability in excitatory and parvalbumin expressing interneurons, cholinergic inputs were shown to have a larger effect on neurons during stationary epochs by maintaining a unimodal distribution of the resting membrane potentials across all cells (Polack et al., 2013). The locomotion-associated depolarizing effect (Bennett et al., 2013; Polack et al., 2013) was still present under glutamatergic inhibition, which led the authors to propose that synaptic glutamatergic input amplifies the locomotion-associated membrane depolarization mediated by noradrenergic inputs (Polack et al., 2013). Interestingly, both publications assessing locomotion-associated subthreshold alterations (Bennett et al., 2013; Polack et al., 2013) did not observe a change in spontaneous firing rates during locomotion when visual input was only provided by an isoluminant gray screen. Though I did not specifically probe motor-related responses in this setting, I recorded neuronal activity in V1 during darkness and still found neurons clearly responsive to running. As the fraction of neurons responsive to running without visual input is quite low (~4%), it is conceivable that these neurons were simply missed in these (Bennett et al., 2013; Polack et al., 2013) electrophysiological experiments. This interpretation further stresses the notion of a large heterogeneity amongst excitatory neurons, even within a given cortical layer. In contrast, visual input

coinciding with locomotion not only increased the membrane potential of excitatory and inhibitory neurons, but also increased spike rates (Niell and Stryker, 2010; Polack et al., 2013), which is in line with the larger fraction of cells responsive to running with feedback compared to running in the dark seen in my experiments.

Moreover, recent publications have expanded our knowledge on the neuronal circuitry underlying the locomotion-associated modulation of sensory processing in V1 (Lee et al., 2014). The authors identified a circuit consisting of the mesencephalic locomotor region (MLR) signaling to the basal forebrain, which in turn sends cholinergic projections to the cortex, including V1 (Lee et al., 2014). The authors proposed that in particular cholinergic inputs to V1 mediate the behavioural, state dependent modulation of sensory responses (Lee et al., 2014). More precisely, cholinergic projections were proposed to activate a disinhibitory cortical circuit by selectively targeting vasoactive intestinal peptide (VIP) expressing interneurons in V1 (Fu et al., 2014). As VIP interneurons are known to inhibit other inhibitory subtypes, such as somatostatin (SOM) or parvalbumin (PV) expressing neurons (Pfeffer et al., 2013), activation of VIP neurons results in a disinhibition of excitatory cells, thereby amplifying visually driven responses in V1 (Fu et al., 2014). In my dataset I, however, found also non-VIP neurons to be strongly driven by locomotion in the absence of visual input, implying that there may also be other circuit mechanisms at play. The described findings emphasizing the role of cholinergic projections in mediating behavioural state- dependent amplification of visually driven responses are somewhat divergent from the pharmacological experiments (Polack et al., 2013), which found no major impact on locomotion-associated changes in the membrane potential or visually driven responses by cholinergic blockade. As Lee et al. (Lee et al., 2014) used optogenetic activation of neurons within the MLR, realized either by direct photoactivation of the MLR or by photoactivation of its projections to the basal forebrain, coincidental activation of noradrenergic neurons residing in the Locus coeruleus can't be ruled out given its close proximity to the MLR and similar projection paths to the basal forebrain (Samuels and Szabadi, 2008a, b) and the entire cortex. Future work is needed to further disentangle the contribution of different neuromodulatory - and potential direct excitatory motor-related inputs - driving neurons in V1.

In Alzheimer's disease a neuromodulatory deficit affecting both the cholinergic and the noradrenergic system is frequently reported (Bondareff et al., 1987; German et al., 1992; Haglund et al., 2006; Matthews et al., 2002). Despite the fact that AD mouse models do not display overt cell loss in brain regions harboring neuromodulatory neurons, such as the Nucleus basalis of Meynert or the Locus coeruleus, there is evidence

for a functional neuromodulatory deficit in AD mice, too (Francis et al., 2012; German et al., 2005; O'Neil et al., 2007). A simple means to probe neuromodulatory signaling in behaving animals is monitoring the pupil diameter (Erisken et al., 2014; Samuels and Szabadi, 2008a, b). I observed a strong reduction in pupil diameter in AD mice during feedback sessions, indicative of a noradrenergic deficit and similar to what has been reported in AD patients (Bitsios et al., 1996; Prettyman et al., 1997). Recent publications demonstrated that locomotion as well as brief brain state changes during quiescence are associated with the dilation of the pupil, likely mediated by noradrenergic inputs (Erisken et al., 2014; Polack et al., 2013; Reimer et al., 2014). The locomotion associated pupil response, consisting of pupil dilation and a ventronasal shift in position, however, was still preserved in AD mice, pointing towards a decreased noradrenergic tone with preserved pulsatile, locomotion-associated noradrenaline release. Together, the data argue for a main impact on the gain of visual and motor-related responses and would hence be in line with a functional neuromodulatory deficit.

5.2.2. Aberrant activity in V1 of AD transgenic mice

The observed hyporesponsiveness to visual – and motor-related inputs was furthermore accompanied by increased spontaneous activity during quiescent states, when neuronal activity typically is strongly reduced (Keller et al., 2012). This spontaneous activity could well reflect the described hyperexcitability in AD transgenic mice (Busche, Palop 2010, Verret 2012), which was suggested to be based on impaired inhibition (Busche et al., 2008; Garcia-Marin et al., 2009; Limon et al., 2012; Palop et al., 2007; Palop and Mucke, 2010; Verret et al., 2012). The disruption of functional connectivity per se should result in impaired information processing and the additional spontaneous, aberrant activity adds further noise to the system thereby potentiating defective circuit function. This hypothesis is corroborated by the significantly impaired coding accuracy of the network as shown by the reduction in accurately decoding running velocity from neuronal activity, which may be jointly caused by the decrease in correlated activity and the increase in spontaneous, uncorrelated activity. Interestingly, the activity of spontaneously active cells in AD mice was reduced during locomotion, which indicates that their integration into functioning circuits is not fully lost. As described above, locomotion reduces background firing rates by decreasing membrane potential variability in excitatory and parvalbumin positive neurons (Bennett et al., 2013; Polack et al., 2013), offering a potential explanation for the decrease in activity during locomotion. It should furthermore be mentioned that I found no link

between any of the parameters analysed, such as active or silent neurons and spontaneously active neurons to plaque proximity. I thus have no indication that neurons close to plaques are affected differently by neurodegenerative processes than those being further away, as had been proposed previously (Busche et al., 2008). This finding at first glance seems to contradict our results of the structural alterations tightly linked spatially to amyloid plaques. A neuron's activity can, however, be dysregulated at multiple levels and affect both pre- and postsynaptic compartments (Liebscher et al., 2014), effects occurring very distant from the soma. As such there could exist both an impact on incoming signals (an effect that should scale with the length of the axon of the respective afferent neuron) and on postsynaptic function due to e.g. the shrinkage, instability or loss of spines. The morphology of neurons, with their radially sent out dendrites of up to multiple hundreds of μm in length, allows them to receive input from various sites. Furthermore, altered activity of single neurons very likely not only affects neighbouring neurons contacted by lateral connections, but at the same time drives inhibitory neurons, which are in turn connected to multiple other excitatory and inhibitory neurons. A disruption of synaptic connectivity may therefore interfere with the fine-tuned balance of excitatory and inhibitory inputs, giving rise to aberrant neuronal activity. Given the intricate complexity of neural networks it is thus conceivable that local synaptic alterations, despite being associated with deposited plaques, have a much more widespread impact on neuronal function, exceeding the directly neighbouring cell bodies. In fact, it is one of the main challenges in AD research to better understand how the globally disrupted synaptic connectivity affects different neural circuits to ultimately result in the clinical symptoms typical of the disease.

As stated above impaired inhibition was proposed to underlie disturbed neuronal activity in AD, I thus also assessed response properties in two different inhibitory cell types, namely parvalbumin and vasoactive intestinal peptide expressing interneurons. These analyses revealed a massive reduction in motor-associated responses in both PV and VIP neurons in AD mice. Moreover, a large fraction of these inhibitory cell types was negatively correlated to running. i.e. spontaneously active. As VIP neurons were proposed to give rise to a disinhibitory circuit controlling PV and SOM positive interneurons (Pfeffer et al., 2013), their aberrant activity could in principle result in impaired inhibition onto pyramidal neurons, hence instigating spontaneous activity in excitatory neurons. Conversely, inhibitory neurons may be activated by aberrantly active excitatory cells, and their increased spontaneous activity may hence be secondary to aberrant activity of excitatory neurons. Given the slow kinetics of GCaMP it is not feasible to distinguish between those two

alternatives using our calcium imaging approach. Irrespective of the actual sequence of events, augmented inhibition - facilitated either by boosting/restoring interneuron function (Verret et al., 2012) or by reducing excitation as realized by pharmacological inhibition of NMDA receptors (a well-established treatment for AD patients, e.g. memantine) - seems to exert beneficial effects on cognition and memory.

5.2.3. Selective resilience of visuomotor mismatch signal in V1

Despite the observed massive alterations in network activity in AD mice comprising a strong reduction in feed-forward signals in V1, paralleled by an increase in uncorrelated noise, I surprisingly found no impact on the visuomotor mismatch signal in V1. This signal is elicited upon a discrepancy between actual and expected visual flow (Keller et al., 2012) and hence hinges on the proper integration of visual and motor-related signals. Given that both signals are scaled down to a similar extent in V1 of APP/PS1 mice, the ratio between both might still be stable and sufficiently large to drive these responses. Additionally, one could imagine that the mismatch signal is secured by a particular synaptic strength of synapses conveying this signal or by a high redundancy of synaptic input sites onto responsive cells, which buffers a potential loss of synapses in APP/PS1 mice. Alternatively, compensatory mechanisms might be at play too, as the mismatch signal seems to be plastic in nature (Keller et al., 2012).

Although the underlying circuitry is not fully understood to date, conceptually one may consider the visuomotor mismatch signal as a prediction error response, which is elicited after the violation of a statistical regularity of a sensory input and commonly studied in auditory and visual processing (Kimura et al., 2011; Naatanen et al., 2007). As such it gives rise to a so-called mismatch negativity signal in humans when assessed via EEG. Typically, the mismatch negativity signal is based on the presentation of a deviant stimulus within a sequence of monotone stimuli. For the visual mismatch negativity (vMMN) this deviation can occur on multiple features of the stimulus, such as color, spatial frequency, line orientation or more complex changes like facial emotions (Stefanics et al., 2014). The cellular and circuit mechanisms giving rise to the vMMN are also not fully understood. One important component of the signal in addition to change detection - that is the detection of a difference in a repetitive sensory stimulation - is repetition suppression (Stefanics et al., 2016). This term refers to a stimulus-specific adaptation in response to the repeated presentation of the same stimulus, for which single neuron correlates were shown in auditory cortex (Escera and Malmierca, 2014; Nelken, 2014).

In an attempt to model the local circuitry giving rise to the mismatch negativity Wacongne et al. 2012 (Wacongne et al., 2012) proposed, amongst other components, a specific population of interneurons, which realize the differentiation between actual and predicted signal. Interestingly, I also found that within the population of mismatch responsive cells in WT animals about 40% were inhibitory, namely PV and VIP positive cells. Given that on average the fraction of interneurons in visual cortex is ~ 20% (DeFelipe, 2002) interneurons are strongly overrepresented in the population of neurons carrying the mismatch signal. Importantly, even though I did not observe a difference in the mismatch response at the population level, the composition of cell types amongst mismatch responsive cells varied strongly in APP/PS1 compared to WT animals, most evidently seen in the strong reduction of the fraction of VIP neurons. VIP neurons were very recently shown to receive more numerous inputs compared to other inhibitory subtypes, such as PV and SOM positive cells (Wall et al., 2016), even from very distant cortical and subcortical areas. Given that structural changes of neurites are mainly observed in association with amyloid plaques throughout the entire cortex, the damage onto long-projecting neurites should scale with length. Thus, input to VIP cells may be particularly affected due to disruptions of long-range neuronal connectivity. The drop in VIP responsiveness to mismatch may in fact be causal to the sustained mismatch response at the population level. However, whether the visuomotor mismatch signal analysed in this work is actually compatible with the mismatch negativity, elicited after the presentation of a deviant stimulus, remains to be clarified. It would, however, be interesting to test whether the selective sparing of mismatch signals holds in human AD patients and if so, whether it can be employed as a diagnostic tool to e.g. differentiate between different forms of dementia.

Taken together, in the second part of my thesis I observed functional alterations of neurons in the visual cortex of behaving APP/PS1 transgenic mice. I found overall a massive reduction in visually driven and motor-related signals, paralleled by an increase in spontaneous, uncorrelated activity, both of which impair the coding accuracy of the local network. These effects were observed in excitatory as well as in inhibitory cells and may represent a general network feature in AD resulting in impaired information processing. Surprisingly, despite the pronounced reduction in feedforward signals I observed a resilience of responses elicited upon a mismatch of actual and expected visual flow in APP/PS1 mice, which may reflect the importance of signals based on the detection of violations of predictions, a mechanism proposed as one of the key principles of brain function.

6 SUMMARY

Alzheimer's disease (AD), the most common form of dementia, has been proposed to result from the degeneration of synapses, putatively caused by assemblies of the amyloid-β peptide (Aβ). The spatiotemporal dynamics of this synaptopathy, its potential reversibility as well as its consequences on the function of single neurons and neuronal circuits, however, are not fully understood to date.

In order to address these questions, I assessed structural and functional alterations of neurons in the neocortex in a transgenic mouse model of Alzheimer's disease, namely APP/PS1 (APPswe, $PS1_{L166P}$) mice, using *in vivo* two-photon imaging. Chronic imaging of dendrites and axons over the course of four weeks revealed not only a reduction in dendritic spine density close to amyloid plaques (proteinaceous extracellular deposits typical of AD), but I also identified synaptic instability as a main aspect contributing to AD pathology. Importantly, while synapse loss was confined to the immediate plaque vicinity (up to 15µm from the histological plaque border), synaptic instability was evident in a much larger region surrounding plaques (50 µm) and affected both, pre- and postsynaptic compartments.

As the prevailing hypothesis in AD holds that Aβ conveys these detrimental effects on synapses one therapeutic approach is based on the pharmacological inhibition of Aβ generation. I thus assessed the impact of a novel selective γ-secretase inhibitor (GSI), a compound that prevents the last cleavage step necessary for the release of Aβ from the longer transmembrane amyloid precursor protein (APP). Notably, the GSI used here primarily interferes with the processing of APP and still allows for processing of other γ-secretase substrates, and hence should largely reduce side effects seen with earlier generations of GSIs before. Daily treatment with the GSI reduced the deposition of Aβ as evidenced by the initial reduction in the number of new plaques and a sustained decrease in the growth of these newly deposited plaques. Importantly, it also ameliorated the plaque-associated synaptic instability, without displaying overt adverse effects on dendritic spines in WT mice. These data represent the first *in vivo* evidence that selective pharmacological inhibition of the γ-secretase mediated APP cleavage can have beneficial effects on synaptic pathology in AD.

Given the widespread impact of Aβ assemblies on neuronal structures, I then asked to which extent these structural alterations affect the function of neurons. To address this question, I recorded neuronal response

properties in the primary visual cortex of behaving APP/PS1 mice, employing *in vivo* two-photon calcium imaging using the genetically encoded calcium indicator GCaMP6m. In order to probe the impact of AD related pathology on specific aspects of information processing, which rely on multiple neuronal circuits, I characterized visually driven and motor-related activity, as well as signals based on mismatches between actual and expected visual input. My data reveal a massive reduction in responsiveness under almost all conditions tested, which is line with the profound impact on neuronal structure. Stimulus selectivity, like orientation or direction tuning, were not altered in APP/PS1 mice, indicating that the main effect is caused by a change in response gain. Along with the massive decrease in feedforward signals, I observed an increase in spontaneous, hence uncorrelated neuronal activity in AD transgenic mice. Both features jointly affected the coding accuracy of the network, and I propose that this combination may represent a common characteristic leading to impaired information processing in AD. Surprisingly, I found that responses elicited after a discordance of actual and expected visual flow during running, i.e. a visuomotor mismatch, were selectively spared in APP/PS1 mice, suggesting a particular resilience of this very signal. Together, both studies demonstrate that global widespread structural changes of neurons in the AD brain are accompanied by a severe impact on information processing, most prominently seen in a strong reduction of feedforward signals. My data, thus, provide a correlate of impaired cognition in AD at the level of single neurons and neural circuits.

7 REFERENCES

Ables, J.L., Breunig, J.J., Eisch, A.J., and Rakic, P. (2011). Not(ch) just development: Notch signalling in the adult brain. Nat Rev Neurosci 12, 269-283.

Akerboom, J., Chen, T.W., Wardill, T.J., Tian, L., Marvin, J.S., Mutlu, S., Calderon, N.C., Esposti, F., Borghuis, B.G., Sun, X.R.*, et al.* (2012). Optimization of a GCaMP calcium indicator for neural activity imaging. J Neurosci 32, 13819-13840.

Akerboom, J., Rivera, J.D., Guilbe, M.M., Malave, E.C., Hernandez, H.H., Tian, L., Hires, S.A., Marvin, J.S., Looger, L.L., and Schreiter, E.R. (2009). Crystal structures of the GCaMP calcium sensor reveal the mechanism of fluorescence signal change and aid rational design. J Biol Chem 284, 6455-6464.

Alberi, L., Hoey, S.E., Brai, E., Scotti, A.L., and Marathe, S. (2013). Notch signaling in the brain: in good and bad times. Ageing Res Rev 12, 801-814.

Albert, M.S., DeKosky, S.T., Dickson, D., Dubois, B., Feldman, H.H., Fox, N.C., Gamst, A., Holtzman, D.M., Jagust, W.J., Petersen, R.C.*, et al.* (2011). The diagnosis of mild cognitive impairment due to Alzheimer's disease: recommendations from the National Institute on Aging-Alzheimer's Association workgroups on diagnostic guidelines for Alzheimer's disease. Alzheimers Dement 7, 270-279.

Alzheimer, A. (1907). Über eine eigenartige Erkrankung der Hirnrinde. Allgeime Zeitschrift für Psychiatrie und Psychisch-Gerichtliche Medizin 64, 146-148.

Andermann, M.L., Kerlin, A.M., Roumis, D.K., Glickfeld, L.L., and Reid, R.C. (2011). Functional specialization of mouse higher visual cortical areas. Neuron 72, 1025-1039.

Anderson, J.C., and Martin, K.A. (2001). Does bouton morphology optimize axon length? Nat Neurosci 4, 1166-1167.

Arellano, J.I., Espinosa, A., Fairen, A., Yuste, R., and DeFelipe, J. (2007). Non-synaptic dendritic spines in neocortex. Neuroscience 145, 464-469.

Atallah, B.V., Bruns, W., Carandini, M., and Scanziani, M. (2012). Parvalbumin-expressing interneurons linearly transform cortical responses to visual stimuli. Neuron 73, 159-170.

Attems, J., Yamaguchi, H., Saido, T.C., and Thal, D.R. (2010). Capillary CAA and perivascular Abeta-deposition: two distinct features of Alzheimer's disease pathology. J Neurol Sci 299, 155-162.

Bailey, C.H., and Kandel, E.R. (1993). Structural changes accompanying memory storage. Annu Rev Physiol 55, 397-426.

Basi, G.S., Hemphill, S., Brigham, E.F., Liao, A., Aubele, D.L., Baker, J., Barbour, R., Bova, M., Chen, X.H., Dappen, M.S.*, et al.* (2010). Amyloid precursor protein selective gamma-secretase inhibitors for treatment of Alzheimer's disease. Alzheimers Res Ther 2, 36.

Benilova, I., Gallardo, R., Ungureanu, A.A., Castillo Cano, V., Snellinx, A., Ramakers, M., Bartic, C., Rousseau, F., Schymkowitz, J., and De Strooper, B. (2014). The Alzheimer disease protective mutation A2T modulates kinetic and thermodynamic properties of amyloid-beta (Abeta) aggregation. J Biol Chem 289, 30977-30989.

Benilova, I., Karran, E., and De Strooper, B. (2012). The toxic Abeta oligomer and Alzheimer's disease: an emperor in need of clothes. Nat Neurosci 15, 349-357.

Bennett, C., Arroyo, S., and Hestrin, S. (2013). Subthreshold mechanisms underlying state-dependent modulation of visual responses. Neuron 80, 350-357.

Bernardinelli, Y., Randall, J., Janett, E., Nikonenko, I., Konig, S., Jones, E.V., Flores, C.E., Murai, K.K., Bochet, C.G., Holtmaat, A., and Muller, D. (2014). Activity-dependent structural plasticity of perisynaptic astrocytic domains promotes excitatory synapse stability. Curr Biol 24, 1679-1688.

Bero, A.W., Bauer, A.Q., Stewart, F.R., White, B.R., Cirrito, J.R., Raichle, M.E., Culver, J.P., and Holtzman, D.M. (2012). Bidirectional relationship between functional connectivity and amyloid-beta deposition in mouse brain. J Neurosci 32, 4334-4340.

Bero, A.W., Yan, P., Roh, J.H., Cirrito, J.R., Stewart, F.R., Raichle, M.E., Lee, J.M., and Holtzman, D.M. (2011). Neuronal activity regulates the regional vulnerability to amyloid-beta deposition. Nat Neurosci 14, 750-756.

Berridge, M.J., Lipp, P., and Bootman, M.D. (2000). The versatility and universality of calcium signalling. Nat Rev Mol Cell Biol 1, 11-21.

Bhatt, D.H., Zhang, S., and Gan, W.B. (2009). Dendritic spine dynamics. Annu Rev Physiol 71, 261-282.

Binzegger, T., Douglas, R.J., and Martin, K.A. (2004). A quantitative map of the circuit of cat primary visual cortex. J Neurosci 24, 8441-8453.

Bishop, G.M., and Robinson, S.R. (2004). Physiological roles of amyloid-beta and implications for its removal in Alzheimer's disease. Drugs Aging 21, 621-630.

Bitan, G., Kirkitadze, M.D., Lomakin, A., Vollers, S.S., Benedek, G.B., and Teplow, D.B. (2003). Amyloid beta -protein (Abeta) assembly: Abeta 40 and Abeta 42 oligomerize through distinct pathways. Proc Natl Acad Sci U S A 100, 330-335.

Bitsios, P., Prettyman, R., and Szabadi, E. (1996). Changes in autonomic function with age: a study of pupillary kinetics in healthy young and old people. Age Ageing 25, 432-438.

Bittner, T., Burgold, S., Dorostkar, M.M., Fuhrmann, M., Wegenast-Braun, B.M., Schmidt, B., Kretzschmar, H., and Herms, J. (2012). Amyloid plaque formation precedes dendritic spine loss. Acta Neuropathol 124, 797-807.

Bittner, T., Fuhrmann, M., Burgold, S., Jung, C.K., Volbracht, C., Steiner, H., Mitteregger, G., Kretzschmar, H.A., Haass, C., and Herms, J. (2009). Gamma-secretase inhibition reduces spine density in vivo via an amyloid precursor protein-dependent pathway. J Neurosci 29, 10405-10409.

Bittner, T., Fuhrmann, M., Burgold, S., Ochs, S.M., Hoffmann, N., Mitteregger, G., Kretzschmar, H., LaFerla, F.M., and Herms, J. (2010). Multiple events lead to dendritic spine loss in triple transgenic Alzheimer's disease mice. PLoS One 5, e15477.

Bock, D.D., Lee, W.C., Kerlin, A.M., Andermann, M.L., Hood, G., Wetzel, A.W., Yurgenson, S., Soucy, E.R., Kim, H.S., and Reid, R.C. (2011). Network anatomy and in vivo physiology of visual cortical neurons. Nature 471, 177-182.

Bolmont, T., Haiss, F., Eicke, D., Radde, R., Mathis, C.A., Klunk, W.E., Kohsaka, S., Jucker, M., and Calhoun, M.E. (2008). Dynamics of the microglial/amyloid interaction indicate a role in plaque maintenance. J Neurosci 28, 4283-4292.

Boncristiano, S., Calhoun, M.E., Howard, V., Bondolfi, L., Kaeser, S.A., Wiederhold, K.H., Staufenbiel, M., and Jucker, M. (2005). Neocortical synaptic bouton number is maintained despite robust amyloid deposition in APP23 transgenic mice. Neurobiol Aging 26, 607-613.

Bondareff, W., Mountjoy, C.Q., Roth, M., Rossor, M.N., Iversen, L.L., Reynolds, G.P., and Hauser, D.L. (1987). Neuronal degeneration in locus ceruleus and cortical correlates of Alzheimer disease. Alzheimer Dis Assoc Disord 1, 256-262.

Bosch, M., and Hayashi, Y. (2012). Structural plasticity of dendritic spines. Curr Opin Neurobiol 22, 383-388.

Braak, H., and Braak, E. (1991). Neuropathological stageing of Alzheimer-related changes. Acta Neuropathol 82, 239-259.

Braak, H., and Braak, E. (1997). Frequency of stages of Alzheimer-related lesions in different age categories. Neurobiol Aging 18, 351-357.

Brookmeyer, R., Corrada, M.M., Curriero, F.C., and Kawas, C. (2002). Survival following a diagnosis of Alzheimer disease. Arch Neurol 59, 1764-1767.

Brouwers, N., Sleegers, K., and Van Broeckhoven, C. (2008). Molecular genetics of Alzheimer's disease: an update. Ann Med 40, 562-583.

Buckner, R.L., Sepulcre, J., Talukdar, T., Krienen, F.M., Liu, H., Hedden, T., Andrews-Hanna, J.R., Sperling, R.A., and Johnson, K.A. (2009). Cortical hubs revealed by intrinsic functional connectivity: mapping, assessment of stability, and relation to Alzheimer's disease. J Neurosci 29, 1860-1873.

Burdick, D., Soreghan, B., Kwon, M., Kosmoski, J., Knauer, M., Henschen, A., Yates, J., Cotman, C., and Glabe, C. (1992). Assembly and aggregation properties of synthetic Alzheimer's A4/beta amyloid peptide analogs. J Biol Chem 267, 546-554.

Burgold, S., Bittner, T., Dorostkar, M.M., Kieser, D., Fuhrmann, M., Mitteregger, G., Kretzschmar, H., Schmidt, B., and Herms, J. (2011). In vivo multiphoton imaging reveals gradual growth of newborn amyloid plaques over weeks. Acta Neuropathol 121, 327-335.

Busche, M.A., Chen, X., Henning, H.A., Reichwald, J., Staufenbiel, M., Sakmann, B., and Konnerth, A. (2012). Critical role of soluble amyloid-beta for early hippocampal hyperactivity in a mouse model of Alzheimer's disease. Proc Natl Acad Sci U S A 109, 8740-8745.

Busche, M.A., Eichhoff, G., Adelsberger, H., Abramowski, D., Wiederhold, K.H., Haass, C., Staufenbiel, M., Konnerth, A., and Garaschuk, O. (2008). Clusters of hyperactive neurons near amyloid plaques in a mouse model of Alzheimer's disease. Science 321, 1686-1689.

Cajal, S.R.y. (1888). Estructura de los centros nerviosos de las aves. Rev Trim Histol Norm Patol, 1-10.

Caroni, P., Donato, F., and Muller, D. (2012). Structural plasticity upon learning: regulation and functions. Nat Rev Neurosci 13, 478-490.

Chalupa, L., and Williams, R. (2008). Eye, Retina and Visual System of the Mouse (Boston: MIT Press).

Chartier-Harlin, M.C., Crawford, F., Houlden, H., Warren, A., Hughes, D., Fidani, L., Goate, A., Rossor, M., Roques, P., Hardy, J., and et al. (1991). Early-onset Alzheimer's disease caused by mutations at codon 717 of the beta-amyloid precursor protein gene. Nature 353, 844-846.

Chen, Q., Cichon, J., Wang, W., Qiu, L., Lee, S.J., Campbell, N.R., Destefino, N., Goard, M.J., Fu, Z., Yasuda, R.*, et al.* (2012a). Imaging neural activity using Thy1-GCaMP transgenic mice. Neuron 76, 297-308.

Chen, T.W., Wardill, T.J., Sun, Y., Pulver, S.R., Renninger, S.L., Baohan, A., Schreiter, E.R., Kerr, R.A., Orger, M.B., Jayaraman, V.*, et al.* (2013). Ultrasensitive fluorescent proteins for imaging neuronal activity. Nature 499, 295-300.

Chen, X., Leischner, U., Varga, Z., Jia, H., Deca, D., Rochefort, N.L., and Konnerth, A. (2012b). LOTOS-based two-photon calcium imaging of dendritic spines in vivo. Nat Protoc 7, 1818-1829.

Christie, R.H., Bacskai, B.J., Zipfel, W.R., Williams, R.M., Kajdasz, S.T., Webb, W.W., and Hyman, B.T. (2001). Growth arrest of individual senile plaques in a model of Alzheimer's disease observed by in vivo multiphoton microscopy. J Neurosci 21, 858-864.

Chung, W.S., Allen, N.J., and Eroglu, C. (2015a). Astrocytes Control Synapse Formation, Function, and Elimination. Cold Spring Harb Perspect Biol 7, a020370.

Chung, W.S., Welsh, C.A., Barres, B.A., and Stevens, B. (2015b). Do glia drive synaptic and cognitive impairment in disease? Nat Neurosci 18, 1539-1545.

Cirrito, J.R., Yamada, K.A., Finn, M.B., Sloviter, R.S., Bales, K.R., May, P.C., Schoepp, D.D., Paul, S.M., Mennerick, S., and Holtzman, D.M. (2005). Synaptic activity regulates interstitial fluid amyloid-beta levels in vivo. Neuron 48, 913-922.

Cisse, M., Halabisky, B., Harris, J., Devidze, N., Dubal, D.B., Sun, B., Orr, A., Lotz, G., Kim, D.H., Hamto, P.*, et al.* (2011). Reversing EphB2 depletion rescues cognitive functions in Alzheimer model. Nature 469, 47-52.

Cohen, A.D., Ikonomovic, M.D., Abrahamson, E.E., Paljug, W.R., Dekosky, S.T., Lefterov, I.M., Koldamova, R.P., Shao, L., Debnath, M.L., Mason, N.S*., et al.* (2009). Anti-Amyloid Effects of Small Molecule Abeta-Binding Agents in PS1/APP Mice. Lett Drug Des Discov 6, 437.

Coleman, P., Federoff, H., and Kurlan, R. (2004). A focus on the synapse for neuroprotection in Alzheimer disease and other dementias. Neurology 63, 1155-1162.

Cooney, J.R., Hurlburt, J.L., Selig, D.K., Harris, K.M., and Fiala, J.C. (2002). Endosomal compartments serve multiple hippocampal dendritic spines from a widespread rather than a local store of recycling membrane. J Neurosci 22, 2215-2224.

Corder, E.H., Saunders, A.M., Strittmatter, W.J., Schmechel, D.E., Gaskell, P.C., Small, G.W., Roses, A.D., Haines, J.L., and Pericak-Vance, M.A. (1993). Gene dose of apolipoprotein E type 4 allele and the risk of Alzheimer's disease in late onset families. Science 261, 921-923.

Cruts, M., and Van Broeckhoven, C. (1998). Molecular genetics of Alzheimer's disease. Ann Med 30, 560-565.

Cruz-Martin, A., Crespo, M., and Portera-Cailliau, C. (2010). Delayed stabilization of dendritic spines in fragile X mice. J Neurosci 30, 7793-7803.

Czirr, E., Leuchtenberger, S., Dorner-Ciossek, C., Schneider, A., Jucker, M.s.p., Koo, E.H., Pietrzik, C.U., Baumann, K., and Weggen, S. (2007). Insensitivity to Abeta42-lowering nonsteroidal anti-inflammatory drugs and gamma-secretase inhibitors is common among aggressive presenilin-1 mutations. J Biol Chem 282, 24504-24513.

D'Andrea, M.R., and Nagele, R.G. (2010). Morphologically distinct types of amyloid plaques point the way to a better understanding of Alzheimer's disease pathogenesis. Biotech Histochem 85, 133-147.

Dana, H., Chen, T.W., Hu, A., Shields, B.C., Guo, C., Looger, L.L., Kim, D.S., and Svoboda, K. (2014). Thy1-GCaMP6 transgenic mice for neuronal population imaging in vivo. PLoS One 9, e108697.

Danysz, W., and Parsons, C.G. (2012). Alzheimer's disease, beta-amyloid, glutamate, NMDA receptors and memantine--searching for the connections. Br J Pharmacol 167, 324-352.

Davies, B., and Morris, T. (1993). Physiological parameters in laboratory animals and humans. Pharm Res 10, 1093-1095.

de Calignon, A., Fox, L.M., Pitstick, R., Carlson, G.A., Bacskai, B.J., Spires-Jones, T.L., and Hyman, B.T. (2010). Caspase activation precedes and leads to tangles. Nature 464, 1201-1204.

de Calignon, A., Spires-Jones, T.L., Pitstick, R., Carlson, G.A., and Hyman, B.T. (2009). Tangle-bearing neurons survive despite disruption of membrane integrity in a mouse model of tauopathy. J Neuropathol Exp Neurol 68, 757-761.

De Paola, V., Holtmaat, A., Knott, G., Song, S., Wilbrecht, L., Caroni, P., and Svoboda, K. (2006). Cell type-specific structural plasticity of axonal branches and boutons in the adult neocortex. Neuron 49, 861-875.

De Roo, M., Klauser, P., Mendez, P., Poglia, L., and Muller, D. (2008a). Activity-dependent PSD formation and stabilization of newly formed spines in hippocampal slice cultures. Cereb Cortex 18, 151-161.

De Roo, M., Klauser, P., and Muller, D. (2008b). LTP promotes a selective long-term stabilization and clustering of dendritic spines. PLoS Biol 6, e219.

De Strooper, B. (2014). Lessons from a failed gamma-secretase Alzheimer trial. Cell 159, 721-726.

DeFelipe, J. (2002). Cortical interneurons: from Cajal to 2001. Prog Brain Res 136, 215-238.

DeKosky, S.T., Scheff, S.W., and Styren, S.D. (1996). Structural correlates of cognition in dementia: quantification and assessment of synapse change. Neurodegeneration 5, 417-421.

Delbeuck, X., Collette, F., and Van der Linden, M. (2007). Is Alzheimer's disease a disconnection syndrome? Evidence from a crossmodal audio-visual illusory experiment. Neuropsychologia 45, 3315-3323.

Denk, W., Strickler, J.H., and Webb, W.W. (1990). Two-photon laser scanning fluorescence microscopy. Science 248, 73-76.

Dohler, F., Sepulveda-Falla, D., Krasemann, S., Altmeppen, H., Schluter, H., Hildebrand, D., Zerr, I., Matschke, J., and Glatzel, M. (2014). High molecular mass assemblies of amyloid-beta oligomers bind prion protein in patients with Alzheimer's disease. Brain 137, 873-886.

Dombeck, D.A., Khabbaz, A.N., Collman, F., Adelman, T.L., and Tank, D.W. (2007). Imaging large-scale neural activity with cellular resolution in awake, mobile mice. Neuron 56, 43-57.

Dong, H., Martin, M.V., Chambers, S., and Csernansky, J.G. (2007). Spatial relationship between synapse loss and beta-amyloid deposition in Tg2576 mice. J Comp Neurol 500, 311-321.

Dong, J., Revilla-Sanchez, R., Moss, S., and Haydon, P.G. (2010). Multiphoton in vivo imaging of amyloid in animal models of Alzheimer's disease. Neuropharmacology 59, 268-275.

Doody, R.S., Raman, R., Farlow, M., Iwatsubo, T., Vellas, B., Joffe, S., Kieburtz, K., He, F., Sun, X., Thomas, R.G.*, et al.* (2013). A phase 3 trial of semagacestat for treatment of Alzheimer's disease. N Engl J Med 369, 341-350.

Dosemeci, A., Makusky, A.J., Jankowska-Stephens, E., Yang, X., Slotta, D.J., and Markey, S.P. (2007). Composition of the synaptic PSD-95 complex. Mol Cell Proteomics 6, 1749-1760.

Douglas, R.J., and Martin, K.A. (2004). Neuronal circuits of the neocortex. Annu Rev Neurosci 27, 419-451.

Douglas, R.J., and Martin, K.A. (2007). Mapping the matrix: the ways of neocortex. Neuron 56, 226-238.

Drager, U.C., and Olsen, J.F. (1980). Origins of crossed and uncrossed retinal projections in pigmented and albino mice. J Comp Neurol 191, 383-412.

Edbauer, D., Winkler, E., Regula, J.T., Pesold, B., Steiner, H., and Haass, C. (2003). Reconstitution of gamma-secretase activity. Nat Cell Biol 5, 486-488.

Engert, F., and Bonhoeffer, T. (1999). Dendritic spine changes associated with hippocampal long-term synaptic plasticity. Nature 399, 66-70.

Erisken, S., Vaiceliunaite, A., Jurjut, O., Fiorini, M., Katzner, S., and Busse, L. (2014). Effects of locomotion extend throughout the mouse early visual system. Curr Biol 24, 2899-2907.

Erskine, L., and Herrera, E. (2014). Connecting the retina to the brain. ASN Neuro 6.

Escera, C., and Malmierca, M.S. (2014). The auditory novelty system: an attempt to integrate human and animal research. Psychophysiology 51, 111-123.

Feng, G., Mellor, R.H., Bernstein, M., Keller-Peck, C., Nguyen, Q.T., Wallace, M., Nerbonne, J.M., Lichtman, J.W., and Sanes, J.R. (2000). Imaging neuronal subsets in transgenic mice expressing multiple spectral variants of GFP. Neuron 28, 41-51.

Filser, S., Ovsepian, S.V., Masana, M., Blazquez-Llorca, L., Brandt Elvang, A., Volbracht, C., Muller, M.B., Jung, C.K., and Herms, J. (2015). Pharmacological inhibition of BACE1 impairs synaptic plasticity and cognitive functions. Biol Psychiatry 77, 729-739.

Fleisher, A.S., Raman, R., Siemers, E.R., Becerra, L., Clark, C.M., Dean, R.A., Farlow, M.R., Galvin, J.E., Peskind, E.R., Quinn, J.F.*, et al.* (2008). Phase 2 safety trial targeting amyloid beta production with a gamma-secretase inhibitor in Alzheimer disease. Arch Neurol 65, 1031-1038.

Fraering, P.C., Ye, W., Strub, J.M., Dolios, G., LaVoie, M.J., Ostaszewski, B.L., van Dorsselaer, A., Wang, R., Selkoe, D.J., and Wolfe, M.S. (2004). Purification and characterization of the human gamma-secretase complex. Biochemistry 43, 9774-9789.

Francis, B.M., Yang, J., Hajderi, E., Brown, M.E., Michalski, B., McLaurin, J., Fahnestock, M., and Mount, H.T. (2012). Reduced tissue levels of noradrenaline are associated with behavioral phenotypes of the TgCRND8 mouse model of Alzheimer's disease. Neuropsychopharmacology 37, 1934-1944.

Fu, M., Yu, X., Lu, J., and Zuo, Y. (2012). Repetitive motor learning induces coordinated formation of clustered dendritic spines in vivo. Nature 483, 92-95.

Fu, Y., Tucciarone, J.M., Espinosa, J.S., Sheng, N., Darcy, D.P., Nicoll, R.A., Huang, Z.J., and Stryker, M.P. (2014). A cortical circuit for gain control by behavioral state. Cell 156, 1139-1152.

Fuhrmann, M., Bittner, T., Jung, C.K., Burgold, S., Page, R.M., Mitteregger, G., Haass, C., LaFerla, F.M., Kretzschmar, H., and Herms, J. (2010). Microglial Cx3cr1 knockout prevents neuron loss in a mouse model of Alzheimer's disease. Nat Neurosci 13, 411-413.

Ganguli, M., Dodge, H.H., Shen, C., Pandav, R.S., and DeKosky, S.T. (2005). Alzheimer disease and mortality: a 15-year epidemiological study. Arch Neurol 62, 779-784.

Gao, E., DeAngelis, G.C., and Burkhalter, A. (2010). Parallel input channels to mouse primary visual cortex. J Neurosci 30, 5912-5926.

Garcia-Alloza, M., Borrelli, L.A., Hyman, B.T., and Bacskai, B.J. (2010). Antioxidants have a rapid and long-lasting effect on neuritic abnormalities in APP:PS1 mice. Neurobiol Aging 31, 2058-2068.

Garcia-Alloza, M., Dodwell, S.A., Meyer-Luehmann, M., Hyman, B.T., and Bacskai, B.J. (2006a). Plaque-derived oxidative stress mediates distorted neurite trajectories in the Alzheimer mouse model. J Neuropathol Exp Neurol 65, 1082-1089.

Garcia-Alloza, M., Robbins, E.M., Zhang-Nunes, S.X., Purcell, S.M., Betensky, R.A., Raju, S., Prada, C., Greenberg, S.M., Bacskai, B.J., and Frosch, M.P. (2006b). Characterization of amyloid deposition in the APPswe/PS1dE9 mouse model of Alzheimer disease. Neurobiol Dis 24, 516-524.

Garcia-Lopez, P., Garcia-Marin, V., and Freire, M. (2007). The discovery of dendritic spines by Cajal in 1888 and its relevance in the present neuroscience. Prog Neurobiol 83, 110-130.

Garcia-Marin, V., Blazquez-Llorca, L., Rodriguez, J.R., Boluda, S., Muntane, G., Ferrer, I., and Defelipe, J. (2009). Diminished perisomatic GABAergic terminals on cortical neurons adjacent to amyloid plaques. Front Neuroanat 3, 28.

Gelosa, G., and Brooks, D.J. (2012). The prognostic value of amyloid imaging. Eur J Nucl Med Mol Imaging 39, 1207-1219.

German, D.C., Manaye, K.F., White, C.L., 3rd, Woodward, D.J., McIntire, D.D., Smith, W.K., Kalaria, R.N., and Mann, D.M. (1992). Disease-specific patterns of locus coeruleus cell loss. Ann Neurol 32, 667-676.

German, D.C., Nelson, O., Liang, F., Liang, C.L., and Games, D. (2005). The PDAPP mouse model of Alzheimer's disease: locus coeruleus neuronal shrinkage. J Comp Neurol 492, 469-476.

Giannakopoulos, P., Kovari, E., Gold, G., von Gunten, A., Hof, P.R., and Bouras, C. (2009). Pathological substrates of cognitive decline in Alzheimer's disease. Front Neurol Neurosci 24, 20-29.

Gibaldi, M.P., B. (1982). Pharmakokinetics, 2 edn (New York: Marcel Dekker

).

Gilbert, C.D. (1983). Microcircuitry of the visual cortex. Annu Rev Neurosci 6, 217-247.

Gilbert, C.D., and Wiesel, T.N. (1983). Functional organization of the visual cortex. Prog Brain Res 58, 209-218.

Glebov, K., Wunderlich, P., Karaca, I., and Walter, J. (2016). Functional involvement of gamma-secretase in signaling of the triggering receptor expressed on myeloid cells-2 (TREM2). J Neuroinflammation 13, 17.

Glenner, G.G., Wong, C.W., Quaranta, V., and Eanes, E.D. (1984). The amyloid deposits in Alzheimer's disease: their nature and pathogenesis. Appl Pathol 2, 357-369.

Goate, A., Chartier-Harlin, M.C., Mullan, M., Brown, J., Crawford, F., Fidani, L., Giuffra, L., Haynes, A., Irving, N., James, L., and et al. (1991). Segregation of a missense mutation in the amyloid precursor protein gene with familial Alzheimer's disease. Nature 349, 704-706.

Goltstein, P.M., Montijn, J.S., and Pennartz, C.M. (2015). Effects of isoflurane anesthesia on ensemble patterns of Ca2+ activity in mouse v1: reduced direction selectivity independent of increased correlations in cellular activity. PLoS One 10, e0118277.

Grafstein, B. (1971). Transneuronal transfer of radioactivity in the central nervous system. Science 172, 177-179.

Gray, E.G. (1959). Electron microscopy of synaptic contacts on dendrite spines of the cerebral cortex. Nature 183, 1592-1593.

Greenberg, D.S., Houweling, A.R., and Kerr, J.N. (2008). Population imaging of ongoing neuronal activity in the visual cortex of awake rats. Nat Neurosci 11, 749-751.

Grienberger, C., Rochefort, N.L., Adelsberger, H., Henning, H.A., Hill, D.N., Reichwald, J., Staufenbiel, M., and Konnerth, A. (2012). Staged decline of neuronal function in vivo in an animal model of Alzheimer's disease. Nat Commun 3, 774.

Griesbeck, O. (2004). Fluorescent proteins as sensors for cellular functions. Curr Opin Neurobiol 14, 636-641.

Grillo, F.W., Song, S., Teles-Grilo Ruivo, L.M., Huang, L., Gao, G., Knott, G.W., Maco, B., Ferretti, V., Thompson, D., Little, G.E., and De Paola, V. (2013). Increased axonal bouton dynamics in the aging mouse cortex. Proc Natl Acad Sci U S A 110, E1514-1523.

Grutzendler, J., Helmin, K., Tsai, J., and Gan, W.B. (2007). Various dendritic abnormalities are associated with fibrillar amyloid deposits in Alzheimer's disease. Ann N Y Acad Sci 1097, 30-39.

Grutzendler, J., Kasthuri, N., and Gan, W.B. (2002). Long-term dendritic spine stability in the adult cortex. Nature 420, 812-816.

Guerreiro, R., Wojtas, A., Bras, J., Carrasquillo, M., Rogaeva, E., Majounie, E., Cruchaga, C., Sassi, C., Kauwe, J.S., Younkin, S*., et al.* (2013). TREM2 variants in Alzheimer's disease. N Engl J Med 368, 117-127.

Haapasalo, A., and Kovacs, D.M. (2011). The many substrates of presenilin/gamma-secretase. J Alzheimers Dis 25, 3-28.

Haass, C. (2004). Take five--BACE and the gamma-secretase quartet conduct Alzheimer's amyloid beta-peptide generation. EMBO J 23, 483-488.

Haass, C., and Selkoe, D.J. (2007). Soluble protein oligomers in neurodegeneration: lessons from the Alzheimer's amyloid beta-peptide. Nat Rev Mol Cell Biol 8, 101-112.

Haglund, M., Sjobeck, M., and Englund, E. (2006). Locus ceruleus degeneration is ubiquitous in Alzheimer's disease: possible implications for diagnosis and treatment. Neuropathology 26, 528-532.

Haider, B., Hausser, M., and Carandini, M. (2013). Inhibition dominates sensory responses in the awake cortex. Nature 493, 97-100.

Hanger, D.P., Seereeram, A., and Noble, W. (2009). Mediators of tau phosphorylation in the pathogenesis of Alzheimer's disease. Expert Rev Neurother 9, 1647-1666.

Hardy, J., Duff, K., Hardy, K.G., Perez-Tur, J., and Hutton, M. (1998). Genetic dissection of Alzheimer's disease and related dementias: amyloid and its relationship to tau. Nat Neurosci 1, 355-358.

Hardy, J., and Selkoe, D.J. (2002). The amyloid hypothesis of Alzheimer's disease: progress and problems on the road to therapeutics. Science 297, 353-356.

Hardy, J.A., and Higgins, G.A. (1992). Alzheimer's disease: the amyloid cascade hypothesis. Science 256, 184-185.

Harnett, M.T., Makara, J.K., Spruston, N., Kath, W.L., and Magee, J.C. (2012). Synaptic amplification by dendritic spines enhances input cooperativity. Nature 491, 599-602.

Harper, J.D., and Lansbury, P.T., Jr. (1997). Models of amyloid seeding in Alzheimer's disease and scrapie: mechanistic truths and physiological consequences of the time-dependent solubility of amyloid proteins. Annu Rev Biochem 66, 385-407.

Harris, K.D., and Mrsic-Flogel, T.D. (2013). Cortical connectivity and sensory coding. Nature 503, 51-58.

Harris, K.M., Jensen, F.E., and Tsao, B. (1992). Three-dimensional structure of dendritic spines and synapses in rat hippocampus (CA1) at postnatal day 15 and adult ages: implications for the maturation of synaptic physiology and long-term potentiation. J Neurosci 12, 2685-2705.

Harris, K.M., and Stevens, J.K. (1989). Dendritic spines of CA 1 pyramidal cells in the rat hippocampus: serial electron microscopy with reference to their biophysical characteristics. J Neurosci 9, 2982-2997.

Harvey, C.D., and Svoboda, K. (2007). Locally dynamic synaptic learning rules in pyramidal neuron dendrites. Nature 450, 1195-1200.

Hawkins, K.M., and Sergio, L.E. (2014). Visuomotor impairments in older adults at increased Alzheimer's disease risk. J Alzheimers Dis 42, 607-621.

Hefendehl, J.K., Wegenast-Braun, B.M., Liebig, C., Eicke, D., Milford, D., Calhoun, M.E., Kohsaka, S., Eichner, M., and Jucker, M. (2011). Long-term in vivo imaging of beta-amyloid plaque appearance and growth in a mouse model of cerebral beta-amyloidosis. J Neurosci 31, 624-629.

Helzner, E.P., Scarmeas, N., Cosentino, S., Tang, M.X., Schupf, N., and Stern, Y. (2008). Survival in Alzheimer disease: a multiethnic, population-based study of incident cases. Neurology 71, 1489-1495.

Hemming, M.L., Elias, J.E., Gygi, S.P., and Selkoe, D.J. (2009). Identification of beta-secretase (BACE1) substrates using quantitative proteomics. PLoS One 4, e8477.

Hendel, T., Mank, M., Schnell, B., Griesbeck, O., Borst, A., and Reiff, D.F. (2008). Fluorescence changes of genetic calcium indicators and OGB-1 correlated with neural activity and calcium in vivo and in vitro. J Neurosci 28, 7399-7411.

Higley, M.J., and Sabatini, B.L. (2008). Calcium signaling in dendrites and spines: practical and functional considerations. Neuron 59, 902-913.

Hofer, S.B., Ko, H., Pichler, B., Vogelstein, J., Ros, H., Zeng, H., Lein, E., Lesica, N.A., and Mrsic-Flogel, T.D. (2011). Differential connectivity and response dynamics of excitatory and inhibitory neurons in visual cortex. Nat Neurosci 14, 1045-1052.

Hofer, S.B., Mrsic-Flogel, T.D., Bonhoeffer, T., and Hubener, M. (2009). Experience leaves a lasting structural trace in cortical circuits. Nature 457, 313-317.

Holtmaat, A., Bonhoeffer, T., Chow, D.K., Chuckowree, J., De Paola, V., Hofer, S.B., Hubener, M., Keck, T., Knott, G., Lee, W.C*., et al.* (2009). Long-term, high-resolution imaging in the mouse neocortex through a chronic cranial window. Nat Protoc 4, 1128-1144.

Holtmaat, A., Wilbrecht, L., Knott, G.W., Welker, E., and Svoboda, K. (2006). Experience-dependent and cell-type-specific spine growth in the neocortex. Nature 441, 979-983.

Holtmaat, A.J., Trachtenberg, J.T., Wilbrecht, L., Shepherd, G.M., Zhang, X., Knott, G.W., and Svoboda, K. (2005). Transient and persistent dendritic spines in the neocortex in vivo. Neuron 45, 279-291.

Hong, S., Beja-Glasser, V.F., Nfonoyim, B.M., Frouin, A., Li, S., Ramakrishnan, S., Merry, K.M., Shi, Q., Rosenthal, A., Barres, B.A*., et al.* (2016). Complement and microglia mediate early synapse loss in Alzheimer mouse models. Science.

Hsieh, H., Boehm, J., Sato, C., Iwatsubo, T., Tomita, T., Sisodia, S., and Malinow, R. (2006). AMPAR removal underlies Abeta-induced synaptic depression and dendritic spine loss. Neuron 52, 831-843.

Huang, Y., Potter, R., Sigurdson, W., Kasten, T., Connors, R., Morris, J.C., Benzinger, T., Mintun, M., Ashwood, T., Ferm, M*., et al.* (2012). beta-amyloid dynamics in human plasma. Arch Neurol 69, 1591-1597.

Hubel, D.H., and Wiesel, T.N. (1959). Receptive fields of single neurones in the cat's striate cortex. J Physiol 148, 574-591.

Hubel, D.H., and Wiesel, T.N. (1962). Receptive fields, binocular interaction and functional architecture in the cat's visual cortex. J Physiol 160, 106-154.

Hubel, D.H., and Wiesel, T.N. (1963). Shape and arrangement of columns in cat's striate cortex. J Physiol 165, 559-568.

Hubener, M. (2003). Mouse visual cortex. Curr Opin Neurobiol 13, 413-420.

Huber, D., Gutnisky, D.A., Peron, S., O'Connor, D.H., Wiegert, J.S., Tian, L., Oertner, T.G., Looger, L.L., and Svoboda, K. (2012). Multiple dynamic representations in the motor cortex during sensorimotor learning. Nature 484, 473-478.

Hyman, B.T. (1997). The neuropathological diagnosis of Alzheimer's disease: clinical-pathological studies. Neurobiol Aging 18, S27-32.

Itagaki, S., McGeer, P.L., Akiyama, H., Zhu, S., and Selkoe, D. (1989). Relationship of microglia and astrocytes to amyloid deposits of Alzheimer disease. J Neuroimmunol 24, 173-182.

Jack, C.R., Jr., Albert, M.S., Knopman, D.S., McKhann, G.M., Sperling, R.A., Carrillo, M.C., Thies, B., and Phelps, C.H. (2011). Introduction to the recommendations from the National Institute on Aging-Alzheimer's Association workgroups on diagnostic guidelines for Alzheimer's disease. Alzheimers Dement 7, 257-262.

Jarrett, J.T., Berger, E.P., and Lansbury, P.T., Jr. (1993). The carboxy terminus of the beta amyloid protein is critical for the seeding of amyloid formation: implications for the pathogenesis of Alzheimer's disease. Biochemistry 32, 4693-4697.

Joachim, C.L., Morris, J.H., and Selkoe, D.J. (1988). Clinically diagnosed Alzheimer's disease: autopsy results in 150 cases. Ann Neurol 24, 50-56.

Johnston, H., Boutin, H., and Allan, S.M. (2011). Assessing the contribution of inflammation in models of Alzheimer's disease. Biochem Soc Trans 39, 886-890.

Jonsson, T., Atwal, J.K., Steinberg, S., Snaedal, J., Jonsson, P.V., Bjornsson, S., Stefansson, H., Sulem, P., Gudbjartsson, D., Maloney, J*., et al.* (2012). A mutation in APP protects against Alzheimer's disease and age-related cognitive decline. Nature 488, 96-99.

Jonsson, T., Stefansson, H., Steinberg, S., Jonsdottir, I., Jonsson, P.V., Snaedal, J., Bjornsson, S., Huttenlocher, J., Levey, A.I., Lah, J.J*., et al.* (2013). Variant of TREM2 associated with the risk of Alzheimer's disease. N Engl J Med 368, 107-116.

Jung, C.K., Fuhrmann, M., Honarnejad, K., Van Leuven, F., and Herms, J. (2011). Role of presenilin1 in structural plasticity of cortical dendritic spines in vivo. J Neurochem 119, 1064-1073.

Kamenetz, F., Tomita, T., Hsieh, H., Seabrook, G., Borchelt, D., Iwatsubo, T., Sisodia, S., and Malinow, R. (2003). APP processing and synaptic function. Neuron 37, 925-937.

Kang, J.E., Lim, M.M., Bateman, R.J., Lee, J.J., Smyth, L.P., Cirrito, J.R., Fujiki, N., Nishino, S., and Holtzman, D.M. (2009). Amyloid-beta dynamics are regulated by orexin and the sleep-wake cycle. Science 326, 1005-1007.

Karran, E., Mercken, M., and De Strooper, B. (2011). The amyloid cascade hypothesis for Alzheimer's disease: an appraisal for the development of therapeutics. Nat Rev Drug Discov 10, 698-712.

Kasai, H., Fukuda, M., Watanabe, S., Hayashi-Takagi, A., and Noguchi, J. (2010). Structural dynamics of dendritic spines in memory and cognition. Trends Neurosci 33, 121-129.

Kasai, H., Matsuzaki, M., Noguchi, J., Yasumatsu, N., and Nakahara, H. (2003). Structure-stability-function relationships of dendritic spines. Trends Neurosci 26, 360-368.

Keck, T., Mrsic-Flogel, T.D., Vaz Afonso, M., Eysel, U.T., Bonhoeffer, T., and Hubener, M. (2008). Massive restructuring of neuronal circuits during functional reorganization of adult visual cortex. Nat Neurosci 11, 1162-1167.

Keith, D., and El-Husseini, A. (2008). Excitation Control: Balancing PSD-95 Function at the Synapse. Front Mol Neurosci 1, 4.

Keller, G.B., Bonhoeffer, T., and Hubener, M. (2012). Sensorimotor mismatch signals in primary visual cortex of the behaving mouse. Neuron 74, 809-815.

Kerlin, A.M., Andermann, M.L., Berezovskii, V.K., and Reid, R.C. (2010). Broadly tuned response properties of diverse inhibitory neuron subtypes in mouse visual cortex. Neuron 67, 858-871.

Kettenmann, H., Kirchhoff, F., and Verkhratsky, A. (2013). Microglia: new roles for the synaptic stripper. Neuron 77, 10-18.

Kim, J.H., Anwyl, R., Suh, Y.H., Djamgoz, M.B., and Rowan, M.J. (2001). Use-dependent effects of amyloidogenic fragments of (beta)-amyloid precursor protein on synaptic plasticity in rat hippocampus in vivo. J Neurosci 21, 1327-1333.

Kim, T., Vidal, G.S., Djurisic, M., William, C.M., Birnbaum, M.E., Garcia, K.C., Hyman, B.T., and Shatz, C.J. (2013). Human LilrB2 is a beta-amyloid receptor and its murine homolog PirB regulates synaptic plasticity in an Alzheimer's model. Science 341, 1399-1404.

Kimberly, W.T., LaVoie, M.J., Ostaszewski, B.L., Ye, W., Wolfe, M.S., and Selkoe, D.J. (2003). Gamma-secretase is a membrane protein complex comprised of presenilin, nicastrin, Aph-1, and Pen-2. Proc Natl Acad Sci U S A 100, 6382-6387.

Kimura, M., Schroger, E., and Czigler, I. (2011). Visual mismatch negativity and its importance in visual cognitive sciences. Neuroreport 22, 669-673.

Kleinberger, G., Yamanishi, Y., Suarez-Calvet, M., Czirr, E., Lohmann, E., Cuyvers, E., Struyfs, H., Pettkus, N., Wenninger-Weinzierl, A., Mazaheri, F.*, et al.* (2014). TREM2 mutations implicated in neurodegeneration impair cell surface transport and phagocytosis. Sci Transl Med 6, 243ra286.

Klunk, W.E., Bacskai, B.J., Mathis, C.A., Kajdasz, S.T., McLellan, M.E., Frosch, M.P., Debnath, M.L., Holt, D.P., Wang, Y., and Hyman, B.T. (2002). Imaging Abeta plaques in living transgenic mice with multiphoton microscopy and methoxy-X04, a systemically administered Congo red derivative. J Neuropathol Exp Neurol 61, 797-805.

Knopfel, T. (2012). Genetically encoded optical indicators for the analysis of neuronal circuits. Nat Rev Neurosci 13, 687-700.

Knopfel, T., Diez-Garcia, J., and Akemann, W. (2006). Optical probing of neuronal circuit dynamics: genetically encoded versus classical fluorescent sensors. Trends Neurosci 29, 160-166.

Knott, G.W., Holtmaat, A., Wilbrecht, L., Welker, E., and Svoboda, K. (2006). Spine growth precedes synapse formation in the adult neocortex in vivo. Nat Neurosci 9, 1117-1124.

Knowles, R.B., Wyart, C., Buldyrev, S.V., Cruz, L., Urbanc, B., Hasselmo, M.E., Stanley, H.E., and Hyman, B.T. (1999). Plaque-induced neurite abnormalities: implications for disruption of neural networks in Alzheimer's disease. Proc Natl Acad Sci U S A 96, 5274-5279.

Ko, H., Hofer, S.B., Pichler, B., Buchanan, K.A., Sjostrom, P.J., and Mrsic-Flogel, T.D. (2011). Functional specificity of local synaptic connections in neocortical networks. Nature 473, 87-91.

Koenigsknecht-Talboo, J., Meyer-Luehmann, M., Parsadanian, M., Garcia-Alloza, M., Finn, M.B., Hyman, B.T., Bacskai, B.J., and Holtzman, D.M. (2008). Rapid microglial response around amyloid pathology after systemic anti-Abeta antibody administration in PDAPP mice. J Neurosci 28, 14156-14164.

Koffie, R.M., Hyman, B.T., and Spires-Jones, T.L. (2011). Alzheimer's disease: synapses gone cold. Mol Neurodegener 6, 63.

Koffie, R.M., Meyer-Luehmann, M., Hashimoto, T., Adams, K.W., Mielke, M.L., Garcia-Alloza, M., Micheva, K.D., Smith, S.J., Kim, M.L., Lee, V.M.*, et al.* (2009). Oligomeric amyloid beta associates with postsynaptic densities and correlates with excitatory synapse loss near senile plaques. Proc Natl Acad Sci U S A 106, 4012-4017.

Koistinaho, M., Kettunen, M.I., Goldsteins, G., Keinanen, R., Salminen, A., Ort, M., Bures, J., Liu, D., Kauppinen, R.A., Higgins, L.S., and Koistinaho, J. (2002). Beta-amyloid precursor protein transgenic mice that harbor diffuse A beta deposits but do not form plaques show increased ischemic vulnerability: role of inflammation. Proc Natl Acad Sci U S A 99, 1610-1615.

Kuchibhotla, K.V., Goldman, S.T., Lattarulo, C.R., Wu, H.Y., Hyman, B.T., and Bacskai, B.J. (2008). Abeta plaques lead to aberrant regulation of calcium homeostasis in vivo resulting in structural and functional disruption of neuronal networks. Neuron 59, 214-225.

Kuhn, P.H., Koroniak, K., Hogl, S., Colombo, A., Zeitschel, U., Willem, M., Volbracht, C., Schepers, U., Imhof, A., Hoffmeister, A*., et al.* (2012). Secretome protein enrichment identifies physiological BACE1 protease substrates in neurons. EMBO J 31, 3157-3168.

Kuwajima, M., Spacek, J., and Harris, K.M. (2012). Beyond counts and shapes: Studying pathology of dendritic spines in the context of the surrounding neuropil through serial section electron microscopy. Neuroscience.

Lacor, P.N., Buniel, M.C., Furlow, P.W., Clemente, A.S., Velasco, P.T., Wood, M., Viola, K.L., and Klein, W.L. (2007). Abeta oligomer-induced aberrations in synapse composition, shape, and density provide a molecular basis for loss of connectivity in Alzheimer's disease. J Neurosci 27, 796-807.

LaFerla, F.M., Green, K.N., and Oddo, S. (2007). Intracellular amyloid-beta in Alzheimer's disease. Nat Rev Neurosci 8, 499-509.

Lambert, J.C., Ibrahim-Verbaas, C.A., Harold, D., Naj, A.C., Sims, R., Bellenguez, C., DeStafano, A.L., Bis, J.C., Beecham, G.W., Grenier-Boley, B*., et al.* (2013). Meta-analysis of 74,046 individuals identifies 11 new susceptibility loci for Alzheimer's disease. Nat Genet 45, 1452-1458.

Larson, E.B., Shadlen, M.F., Wang, L., McCormick, W.C., Bowen, J.D., Teri, L., and Kukull, W.A. (2004). Survival after initial diagnosis of Alzheimer disease. Ann Intern Med 140, 501-509.

Lauren, J., Gimbel, D.A., Nygaard, H.B., Gilbert, J.W., and Strittmatter, S.M. (2009). Cellular prion protein mediates impairment of synaptic plasticity by amyloid-beta oligomers. Nature 457, 1128-1132.

Lee, A.M., Hoy, J.L., Bonci, A., Wilbrecht, L., Stryker, M.P., and Niell, C.M. (2014). Identification of a brainstem circuit regulating visual cortical state in parallel with locomotion. Neuron 83, 455-466.

Leinweber, M., Zmarz, P., Buchmann, P., Argast, P., Hubener, M., Bonhoeffer, T., and Keller, G.B. (2014). Two-photon calcium imaging in mice navigating a virtual reality environment. J Vis Exp, e50885.

Levelt, C.N., and Hubener, M. (2012). Critical-period plasticity in the visual cortex. Annu Rev Neurosci 35, 309-330.

Li, S., Hong, S., Shepardson, N.E., Walsh, D.M., Shankar, G.M., and Selkoe, D. (2009). Soluble oligomers of amyloid Beta protein facilitate hippocampal long-term depression by disrupting neuronal glutamate uptake. Neuron 62, 788-801.

Li, S., Jin, M., Koeglsperger, T., Shepardson, N.E., Shankar, G.M., and Selkoe, D.J. (2011a). Soluble Abeta oligomers inhibit long-term potentiation through a mechanism involving excessive activation of extrasynaptic NR2B-containing NMDA receptors. J Neurosci 31, 6627-6638.

Li, S.F., Wu, M.N., Wang, X.H., Yuan, L., Yang, D., and Qi, J.S. (2011b). Requirement of alpha7 nicotinic acetylcholine receptors for amyloid beta protein-induced depression of hippocampal long-term potentiation in CA1 region of rats in vivo. Synapse 65, 1136-1143.

Li, Y., Van Hooser, S.D., Mazurek, M., White, L.E., and Fitzpatrick, D. (2008). Experience with moving visual stimuli drives the early development of cortical direction selectivity. Nature 456, 952-956.

Lian, H., Yang, L., Cole, A., Sun, L., Chiang, A.C., Fowler, S.W., Shim, D.J., Rodriguez-Rivera, J., Taglialatela, G., Jankowsky, J.L*., et al.* (2015). NFkappaB-activated astroglial release of complement C3 compromises neuronal morphology and function associated with Alzheimer's disease. Neuron 85, 101-115.

Lichtenthaler, S.F. (2011). Alpha-secretase in Alzheimer's disease: molecular identity, regulation and therapeutic potential. J Neurochem 116, 10-21.

Lichtenthaler, S.F. (2012). Alpha-secretase cleavage of the amyloid precursor protein: proteolysis regulated by signaling pathways and protein trafficking. Curr Alzheimer Res 9, 165-177.

Lichtenthaler, S.F., Haass, C., and Steiner, H. (2011). Regulated intramembrane proteolysis--lessons from amyloid precursor protein processing. J Neurochem 117, 779-796.

Liebscher, S., Keller, G.B., Goltstein, P.M., Bonhoeffer, T., and Hubener, M. (2016). Selective Persistence of Sensorimotor Mismatch Signals in Visual Cortex of Behaving Alzheimer's Disease Mice. Curr Biol 26, 956-964.

Liebscher, S., and Meyer-Luehmann, M. (2012). A Peephole into the Brain: Neuropathological Features of Alzheimer's Disease Revealed by in vivo Two-Photon Imaging. Front Psychiatry 3, 26.

Liebscher, S., Page, R.M., Kafer, K., Winkler, E., Quinn, K., Goldbach, E., Brigham, E.F., Quincy, D., Basi, G.S., Schenk, D.B.*, et al.* (2014). Chronic gamma-secretase inhibition reduces amyloid plaque-associated instability of pre- and postsynaptic structures. Mol Psychiatry 19, 937-946.

Limon, A., Reyes-Ruiz, J.M., and Miledi, R. (2012). Loss of functional GABA(A) receptors in the Alzheimer diseased brain. Proc Natl Acad Sci U S A 109, 10071-10076.

Liu, Y., Yu, C., Zhang, X., Liu, J., Duan, Y., Alexander-Bloch, A.F., Liu, B., Jiang, T., and Bullmore, E. (2014). Impaired long distance functional connectivity and weighted network architecture in Alzheimer's disease. Cereb Cortex 24, 1422-1435.

Liu, Z., Condello, C., Schain, A., Harb, R., and Grutzendler, J. (2010). CX3CR1 in microglia regulates brain amyloid deposition through selective protofibrillar amyloid-beta phagocytosis. J Neurosci 30, 17091-17101.

Loewenstein, Y., Kuras, A., and Rumpel, S. (2011). Multiplicative dynamics underlie the emergence of the log-normal distribution of spine sizes in the neocortex in vivo. J Neurosci 31, 9481-9488.

Looger, L.L., and Griesbeck, O. (2012). Genetically encoded neural activity indicators. Curr Opin Neurobiol 22, 18-23.

Mahley, R.W., and Huang, Y. (1999). Apolipoprotein E: from atherosclerosis to Alzheimer's disease and beyond. Curr Opin Lipidol 10, 207-217.

Maletic-Savatic, M., Malinow, R., and Svoboda, K. (1999). Rapid dendritic morphogenesis in CA1 hippocampal dendrites induced by synaptic activity. Science 283, 1923-1927.

Maloney, J.A., Bainbridge, T., Gustafson, A., Zhang, S., Kyauk, R., Steiner, P., van der Brug, M., Liu, Y., Ernst, J.A., Watts, R.J., and Atwal, J.K. (2014). Molecular mechanisms of Alzheimer disease protection by the A673T allele of amyloid precursor protein. J Biol Chem 289, 30990-31000.

Mank, M., Santos, A.F., Direnberger, S., Mrsic-Flogel, T.D., Hofer, S.B., Stein, V., Hendel, T., Reiff, D.F., Levelt, C., Borst, A.*, et al.* (2008). A genetically encoded calcium indicator for chronic in vivo two-photon imaging. Nat Methods 5, 805-811.

Mann, D.M. (1985). The neuropathology of Alzheimer's disease: a review with pathogenetic, aetiological and therapeutic considerations. Mech Ageing Dev 31, 213-255.

Martone, R.L., Zhou, H., Atchison, K., Comery, T., Xu, J.Z., Huang, X., Gong, X., Jin, M., Kreft, A., Harrison, B.*, et al.* (2009). Begacestat (GSI-953): a novel, selective thiophene sulfonamide inhibitor of amyloid precursor protein gamma-secretase for the treatment of Alzheimer's disease. J Pharmacol Exp Ther 331, 598-608.

Masliah, E., Terry, R.D., Alford, M., DeTeresa, R., and Hansen, L.A. (1991). Cortical and subcortical patterns of synaptophysinlike immunoreactivity in Alzheimer's disease. Am J Pathol 138, 235-246.

Masters, C.L., Simms, G., Weinman, N.A., Multhaup, G., McDonald, B.L., and Beyreuther, K. (1985). Amyloid plaque core protein in Alzheimer disease and Down syndrome. Proc Natl Acad Sci U S A 82, 4245-4249.

Matthews, K.L., Chen, C.P., Esiri, M.M., Keene, J., Minger, S.L., and Francis, P.T. (2002). Noradrenergic changes, aggressive behavior, and cognition in patients with dementia. Biol Psychiatry 51, 407-416.

McCarter, J.F., Liebscher, S., Bachhuber, T., Abou-Ajram, C., Hubener, M., Hyman, B.T., Haass, C., and Meyer-Luehmann, M. (2013). Clustering of plaques contributes to plaque growth in a mouse model of Alzheimer's disease. Acta Neuropathol 126, 179-188.

McKhann, G.M., Knopman, D.S., Chertkow, H., Hyman, B.T., Jack, C.R., Jr., Kawas, C.H., Klunk, W.E., Koroshetz, W.J., Manly, J.J., Mayeux, R.*, et al.* (2011). The diagnosis of dementia due to Alzheimer's disease: recommendations from the National Institute on Aging-Alzheimer's Association workgroups on diagnostic guidelines for Alzheimer's disease. Alzheimers Dement 7, 263-269.

Meyer-Luehmann, M., Spires-Jones, T.L., Prada, C., Garcia-Alloza, M., de Calignon, A., Rozkalne, A., Koenigsknecht-Talboo, J., Holtzman, D.M., Bacskai, B.J., and Hyman, B.T. (2008). Rapid appearance and local toxicity of amyloid-beta plaques in a mouse model of Alzheimer's disease. Nature 451, 720-724.

Moehlmann, T., Winkler, E., Xia, X., Edbauer, D., Murrell, J., Capell, A., Kaether, C., Zheng, H., Ghetti, B., Haass, C., and Steiner, H. (2002). Presenilin-1 mutations of leucine 166 equally affect the generation of the Notch and APP intracellular domains independent of their effect on Abeta 42 production. Proc Natl Acad Sci U S A 99, 8025-8030.

Morgan, D., Gordon, M.N., Tan, J., Wilcock, D., and Rojiani, A.M. (2005). Dynamic complexity of the microglial activation response in transgenic models of amyloid deposition: implications for Alzheimer therapeutics. J Neuropathol Exp Neurol 64, 743-753.

Morley, J.E., Farr, S.A., Banks, W.A., Johnson, S.N., Yamada, K.A., and Xu, L. (2010). A physiological role for amyloid-beta protein:enhancement of learning and memory. J Alzheimers Dis 19, 441-449.

Mostany, R., Anstey, J.E., Crump, K.L., Maco, B., Knott, G., and Portera-Cailliau, C. (2013). Altered synaptic dynamics during normal brain aging. J Neurosci 33, 4094-4104.

Mucke, L., and Selkoe, D.J. (2012). Neurotoxicity of Amyloid beta-Protein: Synaptic and Network Dysfunction. Cold Spring Harb Perspect Med 2, a006338.

Murmu, R.P., Li, W., Holtmaat, A., and Li, J.Y. (2013). Dendritic spine instability leads to progressive neocortical spine loss in a mouse model of Huntington's disease. J Neurosci 33, 12997-13009.

Murrell, J., Farlow, M., Ghetti, B., and Benson, M.D. (1991). A mutation in the amyloid precursor protein associated with hereditary Alzheimer's disease. Science 254, 97-99.

Murrell, J.R., Hake, A.M., Quaid, K.A., Farlow, M.R., and Ghetti, B. (2000). Early-onset Alzheimer disease caused by a new mutation (V717L) in the amyloid precursor protein gene. Arch Neurol 57, 885-887.

Musiek, E.S., and Holtzman, D.M. (2015). Three dimensions of the amyloid hypothesis: time, space and 'wingmen'. Nat Neurosci 18, 800-806.

Musiek, E.S., Xiong, D.D., and Holtzman, D.M. (2015). Sleep, circadian rhythms, and the pathogenesis of Alzheimer disease. Exp Mol Med 47, e148.

Naatanen, R., Paavilainen, P., Rinne, T., and Alho, K. (2007). The mismatch negativity (MMN) in basic research of central auditory processing: a review. Clin Neurophysiol 118, 2544-2590.

Nagele, R.G., Wegiel, J., Venkataraman, V., Imaki, H., and Wang, K.C. (2004). Contribution of glial cells to the development of amyloid plaques in Alzheimer's disease. Neurobiol Aging 25, 663-674.

Nakai, J., Ohkura, M., and Imoto, K. (2001). A high signal-to-noise Ca(2+) probe composed of a single green fluorescent protein. Nat Biotechnol 19, 137-141.

Nelken, I. (2014). Stimulus-specific adaptation and deviance detection in the auditory system: experiments and models. Biol Cybern 108, 655-663.

Nelson, P.T., Alafuzoff, I., Bigio, E.H., Bouras, C., Braak, H., Cairns, N.J., Castellani, R.J., Crain, B.J., Davies, P., Del Tredici, K.*, et al.* (2012). Correlation of Alzheimer disease neuropathologic changes with cognitive status: a review of the literature. J Neuropathol Exp Neurol 71, 362-381.

Niell, C.M., and Stryker, M.P. (2008). Highly selective receptive fields in mouse visual cortex. J Neurosci 28, 7520-7536.

Niell, C.M., and Stryker, M.P. (2010). Modulation of visual responses by behavioral state in mouse visual cortex. Neuron 65, 472-479.

Nir, T.M., Jahanshad, N., Villalon-Reina, J.E., Toga, A.W., Jack, C.R., Weiner, M.W., Thompson, P.M., and Alzheimer's Disease Neuroimaging, I. (2013). Effectiveness of regional DTI measures in distinguishing Alzheimer's disease, MCI, and normal aging. Neuroimage Clin 3, 180-195.

O'Neil, J.N., Mouton, P.R., Tizabi, Y., Ottinger, M.A., Lei, D.L., Ingram, D.K., and Manaye, K.F. (2007). Catecholaminergic neuronal loss in locus coeruleus of aged female dtg APP/PS1 mice. J Chem Neuroanat 34, 102-107.

Ohki, K., Chung, S., Ch'ng, Y.H., Kara, P., and Reid, R.C. (2005). Functional imaging with cellular resolution reveals precise micro-architecture in visual cortex. Nature 433, 597-603.

Ohkura, M., Sasaki, T., Kobayashi, C., Ikegaya, Y., and Nakai, J. (2012). An improved genetically encoded red fluorescent Ca2+ indicator for detecting optically evoked action potentials. PLoS One 7, e39933.

Page, R.M., Gutsmiedl, A., Fukumori, A., Winkler, E., Haass, C., and Steiner, H. (2010). Beta-amyloid precursor protein mutants respond to gamma-secretase modulators. J Biol Chem 285, 17798-17810.

Palop, J.J., Chin, J., Roberson, E.D., Wang, J., Thwin, M.T., Bien-Ly, N., Yoo, J., Ho, K.O., Yu, G.Q., Kreitzer, A.*, et al.* (2007). Aberrant excitatory neuronal activity and compensatory remodeling of inhibitory hippocampal circuits in mouse models of Alzheimer's disease. Neuron 55, 697-711.

Palop, J.J., and Mucke, L. (2010). Amyloid-beta-induced neuronal dysfunction in Alzheimer's disease: from synapses toward neural networks. Nat Neurosci 13, 812-818.

Pan, F., Aldridge, G.M., Greenough, W.T., and Gan, W.B. (2010). Dendritic spine instability and insensitivity to modulation by sensory experience in a mouse model of fragile X syndrome. Proc Natl Acad Sci U S A 107, 17768-17773.

Parihar, M.S., and Brewer, G.J. (2010). Amyloid-beta as a modulator of synaptic plasticity. J Alzheimers Dis 22, 741-763.

Pearson, H.A., and Peers, C. (2006). Physiological roles for amyloid beta peptides. J Physiol 575, 5-10.

Perl, D.P. (2010). Neuropathology of Alzheimer's disease. Mt Sinai J Med 77, 32-42.

Peters, A., and Kaiserman-Abramof, I.R. (1970). The small pyramidal neuron of the rat cerebral cortex. The perikaryon, dendrites and spines. Am J Anat 127, 321-355.

Petro, L.S., Vizioli, L., and Muckli, L. (2014). Contributions of cortical feedback to sensory processing in primary visual cortex. Front Psychol 5, 1223.

Pfeffer, C.K., Xue, M., He, M., Huang, Z.J., and Scanziani, M. (2013). Inhibition of inhibition in visual cortex: the logic of connections between molecularly distinct interneurons. Nat Neurosci 16, 1068-1076.

Pihlaja, R., Koistinaho, J., Malm, T., Sikkila, H., Vainio, S., and Koistinaho, M. (2008). Transplanted astrocytes internalize deposited beta-amyloid peptides in a transgenic mouse model of Alzheimer's disease. Glia 56, 154-163.

Pimplikar, S.W. (2009). Reassessing the amyloid cascade hypothesis of Alzheimer's disease. Int J Biochem Cell Biol 41, 1261-1268.

Polack, P.O., Friedman, J., and Golshani, P. (2013). Cellular mechanisms of brain state-dependent gain modulation in visual cortex. Nat Neurosci 16, 1331-1339.

Popov, V.I., and Stewart, M.G. (2009). Complexity of contacts between synaptic boutons and dendritic spines in adult rat hippocampus: three-dimensional reconstructions from serial ultrathin sections in vivo. Synapse 63, 369-377.

Postina, R. (2012). Activation of alpha-secretase cleavage. J Neurochem 120 Suppl 1, 46-54.

Prada, C.M., Garcia-Alloza, M., Betensky, R.A., Zhang-Nunes, S.X., Greenberg, S.M., Bacskai, B.J., and Frosch, M.P. (2007). Antibody-mediated clearance of amyloid-beta peptide from cerebral amyloid angiopathy revealed by quantitative in vivo imaging. J Neurosci 27, 1973-1980.

Prettyman, R., Bitsios, P., and Szabadi, E. (1997). Altered pupillary size and darkness and light reflexes in Alzheimer's disease. J Neurol Neurosurg Psychiatry 62, 665-668.

Qin, Y.Y., Li, M.W., Zhang, S., Zhang, Y., Zhao, L.Y., Lei, H., Oishi, K., and Zhu, W.Z. (2013). In vivo quantitative whole-brain diffusion tensor imaging analysis of APP/PS1 transgenic mice using voxel-based and atlas-based methods. Neuroradiology 55, 1027-1038.

Radde, R., Bolmont, T., Kaeser, S.A., Coomaraswamy, J., Lindau, D., Stoltze, L., Calhoun, M.E., Jaggi, F., Wolburg, H., Gengler, S*., et al.* (2006). Abeta42-driven cerebral amyloidosis in transgenic mice reveals early and robust pathology. EMBO Rep 7, 940-946.

Reiman, E.M., Quiroz, Y.T., Fleisher, A.S., Chen, K., Velez-Pardo, C., Jimenez-Del-Rio, M., Fagan, A.M., Shah, A.R., Alvarez, S., Arbelaez, A*., et al.* (2012). Brain imaging and fluid biomarker analysis in young adults at genetic risk for autosomal dominant Alzheimer's disease in the presenilin 1 E280A kindred: a case-control study. Lancet Neurol 11, 1048-1056.

Reimer, J., Froudarakis, E., Cadwell, C.R., Yatsenko, D., Denfield, G.H., and Tolias, A.S. (2014). Pupil fluctuations track fast switching of cortical states during quiet wakefulness. Neuron 84, 355-362.

Reitz, C., Cheng, R., Rogaeva, E., Lee, J.H., Tokuhiro, S., Zou, F., Bettens, K., Sleegers, K., Tan, E.K., Kimura, R*., et al.* (2011). Meta-analysis of the association between variants in SORL1 and Alzheimer disease. Arch Neurol 68, 99-106.

Rogaeva, E., Meng, Y., Lee, J.H., Gu, Y., Kawarai, T., Zou, F., Katayama, T., Baldwin, C.T., Cheng, R., Hasegawa, H*., et al.* (2007). The neuronal sortilin-related receptor SORL1 is genetically associated with Alzheimer disease. Nat Genet 39, 168-177.

Sakatani, T., and Isa, T. (2007). Quantitative analysis of spontaneous saccade-like rapid eye movements in C57BL/6 mice. Neurosci Res 58, 324-331.

Saleem, A.B., Ayaz, A., Jeffery, K.J., Harris, K.D., and Carandini, M. (2013). Integration of visual motion and locomotion in mouse visual cortex. Nat Neurosci 16, 1864-1869.

Samuels, E.R., and Szabadi, E. (2008a). Functional neuroanatomy of the noradrenergic locus coeruleus: its roles in the regulation of arousal and autonomic function part I: principles of functional organisation. Curr Neuropharmacol 6, 235-253.

Samuels, E.R., and Szabadi, E. (2008b). Functional neuroanatomy of the noradrenergic locus coeruleus: its roles in the regulation of arousal and autonomic function part II: physiological and pharmacological manipulations and pathological alterations of locus coeruleus activity in humans. Curr Neuropharmacol 6, 254-285.

Sawinski, J., Wallace, D.J., Greenberg, D.S., Grossmann, S., Denk, W., and Kerr, J.N. (2009). Visually evoked activity in cortical cells imaged in freely moving animals. Proc Natl Acad Sci U S A 106, 19557-19562.

Schafer, D.P., Lehrman, E.K., Kautzman, A.G., Koyama, R., Mardinly, A.R., Yamasaki, R., Ransohoff, R.M., Greenberg, M.E., Barres, B.A., and Stevens, B. (2012). Microglia sculpt postnatal neural circuits in an activity and complement-dependent manner. Neuron 74, 691-705.

Scheff, S.W., and Price, D.A. (2006). Alzheimer's disease-related alterations in synaptic density: neocortex and hippocampus. J Alzheimers Dis 9, 101-115.

Schellenberg, G.D., and Montine, T.J. (2012). The genetics and neuropathology of Alzheimer's disease. Acta Neuropathol 124, 305-323.

Segal, M. (2005). Dendritic spines and long-term plasticity. Nat Rev Neurosci 6, 277-284.

Segal, M., Vlachos, A., and Korkotian, E. (2010). The spine apparatus, synaptopodin, and dendritic spine plasticity. Neuroscientist 16, 125-131.

Selkoe, D.J. (1991). The molecular pathology of Alzheimer's disease. Neuron 6, 487-498.

Selkoe, D.J. (2002). Alzheimer's disease is a synaptic failure. Science 298, 789-791.

Serrano-Pozo, A., Frosch, M.P., Masliah, E., and Hyman, B.T. (2011). Neuropathological alterations in Alzheimer disease. Cold Spring Harb Perspect Med 1, a006189.

Shankar, G.M., Bloodgood, B.L., Townsend, M., Walsh, D.M., Selkoe, D.J., and Sabatini, B.L. (2007). Natural oligomers of the Alzheimer amyloid-beta protein induce reversible synapse loss by modulating an NMDA-type glutamate receptor-dependent signaling pathway. J Neurosci 27, 2866-2875.

Shankar, G.M., Li, S., Mehta, T.H., Garcia-Munoz, A., Shepardson, N.E., Smith, I., Brett, F.M., Farrell, M.A., Rowan, M.J., Lemere, C.A*., et al.* (2008). Amyloid-beta protein dimers isolated directly from Alzheimer's brains impair synaptic plasticity and memory. Nat Med 14, 837-842.

Sheng, M., and Kim, E. (2011). The postsynaptic organization of synapses. Cold Spring Harb Perspect Biol 3.

Shepherd, G.M., and Harris, K.M. (1998). Three-dimensional structure and composition of CA3-->CA1 axons in rat hippocampal slices: implications for presynaptic connectivity and compartmentalization. J Neurosci 18, 8300-8310.

Shi, Q., Colodner, K.J., Matousek, S.B., Merry, K., Hong, S., Kenison, J.E., Frost, J.L., Le, K.X., Li, S., Dodart, J.C*., et al.* (2015). Complement C3-Deficient Mice Fail to Display Age-Related Hippocampal Decline. J Neurosci 35, 13029-13042.

Shu, X., Qin, Y.Y., Zhang, S., Jiang, J.J., Zhang, Y., Zhao, L.Y., Shan, D., and Zhu, W.Z. (2013). Voxel-based diffusion tensor imaging of an APP/PS1 mouse model of Alzheimer's disease. Mol Neurobiol 48, 78-83.

Siemers, E.R., Dean, R.A., Friedrich, S., Ferguson-Sells, L., Gonzales, C., Farlow, M.R., and May, P.C. (2007). Safety, tolerability, and effects on plasma and cerebrospinal fluid amyloid-beta after inhibition of gamma-secretase. Clin Neuropharmacol 30, 317-325.

Skottun, B.C., De Valois, R.L., Grosof, D.H., Movshon, J.A., Albrecht, D.G., and Bonds, A.B. (1991). Classifying simple and complex cells on the basis of response modulation. Vision Res 31, 1079-1086.

Snyder, E.M., Nong, Y., Almeida, C.G., Paul, S., Moran, T., Choi, E.Y., Nairn, A.C., Salter, M.W., Lombroso, P.J., Gouras, G.K., and Greengard, P. (2005). Regulation of NMDA receptor trafficking by amyloid-beta. Nat Neurosci 8, 1051-1058.

Sokolowski, J.D., and Mandell, J.W. (2011). Phagocytic clearance in neurodegeneration. Am J Pathol 178, 1416-1428.

Sorra, K.E., and Harris, K.M. (1993). Occurrence and three-dimensional structure of multiple synapses between individual radiatum axons and their target pyramidal cells in hippocampal area CA1. J Neurosci 13, 3736-3748.

Sperling, R.A., Aisen, P.S., Beckett, L.A., Bennett, D.A., Craft, S., Fagan, A.M., Iwatsubo, T., Jack, C.R., Jr., Kaye, J., Montine, T.J*., et al.* (2011). Toward defining the preclinical stages of Alzheimer's disease: recommendations from the National Institute on Aging-Alzheimer's Association workgroups on diagnostic guidelines for Alzheimer's disease. Alzheimers Dement 7, 280-292.

Spires-Jones, T.L., de Calignon, A., Matsui, T., Zehr, C., Pitstick, R., Wu, H.Y., Osetek, J.D., Jones, P.B., Bacskai, B.J., Feany, M.B*., et al.* (2008). In vivo imaging reveals dissociation between caspase activation and acute neuronal death in tangle-bearing neurons. J Neurosci 28, 862-867.

Spires-Jones, T.L., Meyer-Luehmann, M., Osetek, J.D., Jones, P.B., Stern, E.A., Bacskai, B.J., and Hyman, B.T. (2007). Impaired spine stability underlies plaque-related spine loss in an Alzheimer's disease mouse model. Am J Pathol 171, 1304-1311.

Spires, T.L., Meyer-Luehmann, M., Stern, E.A., McLean, P.J., Skoch, J., Nguyen, P.T., Bacskai, B.J., and Hyman, B.T. (2005). Dendritic spine abnormalities in amyloid precursor protein transgenic mice demonstrated by gene transfer and intravital multiphoton microscopy. J Neurosci 25, 7278-7287.

Stefanics, G., Astikainen, P., and Czigler, I. (2014). Visual mismatch negativity (vMMN): a prediction error signal in the visual modality. Front Hum Neurosci 8, 1074.

Stefanics, G., Kremlacek, J., and Czigler, I. (2016). Mismatch negativity and neural adaptation: Two sides of the same coin. Response: Commentary: Visual mismatch negativity: a predictive coding view. Front Hum Neurosci 10, 13.

Steiner, H. (2008). The catalytic core of gamma-secretase: presenilin revisited. Curr Alzheimer Res 5, 147-157.

Steiner, H., Fluhrer, R., and Haass, C. (2008). Intramembrane proteolysis by gamma-secretase. J Biol Chem 283, 29627-29631.

Steiner, H., Kostka, M., Romig, H., Basset, G., Pesold, B., Hardy, J., Capell, A., Meyn, L., Grim, M.L., Baumeister, R.*, et al.* (2000). Glycine 384 is required for presenilin-1 function and is conserved in bacterial polytopic aspartyl proteases. Nat Cell Biol 2, 848-851.

Stevens, B., Allen, N.J., Vazquez, L.E., Howell, G.R., Christopherson, K.S., Nouri, N., Micheva, K.D., Mehalow, A.K., Huberman, A.D., Stafford, B.*, et al.* (2007). The classical complement cascade mediates CNS synapse elimination. Cell 131, 1164-1178.

Steward, O., and Schuman, E.M. (2001). Protein synthesis at synaptic sites on dendrites. Annu Rev Neurosci 24, 299-325.

Strassnig, M., and Ganguli, M. (2005). About a peculiar disease of the cerebral cortex: Alzheimer's original case revisited. Psychiatry (Edgmont) 2, 30-33.

Strittmatter, W.J., Saunders, A.M., Schmechel, D., Pericak-Vance, M., Enghild, J., Salvesen, G.S., and Roses, A.D. (1993). Apolipoprotein E: high-avidity binding to beta-amyloid and increased frequency of type 4 allele in late-onset familial Alzheimer disease. Proc Natl Acad Sci U S A 90, 1977-1981.

Svoboda, K., and Yasuda, R. (2006). Principles of two-photon excitation microscopy and its applications to neuroscience. Neuron 50, 823-839.

Tackenberg, C., Ghori, A., and Brandt, R. (2009). Thin, stubby or mushroom: spine pathology in Alzheimer's disease. Curr Alzheimer Res 6, 261-268.

Tashiro, A., and Yuste, R. (2003). Structure and molecular organization of dendritic spines. Histol Histopathol 18, 617-634.

Terry, R.D., Masliah, E., Salmon, D.P., Butters, N., DeTeresa, R., Hill, R., Hansen, L.A., and Katzman, R. (1991). Physical basis of cognitive alterations in Alzheimer's disease: synapse loss is the major correlate of cognitive impairment. Ann Neurol 30, 572-580.

Texido, L., Martin-Satue, M., Alberdi, E., Solsona, C., and Matute, C. (2011). Amyloid beta peptide oligomers directly activate NMDA receptors. Cell Calcium 49, 184-190.

Tian, L., Akerboom, J., Schreiter, E.R., and Looger, L.L. (2012a). Neural activity imaging with genetically encoded calcium indicators. Prog Brain Res 196, 79-94.

Tian, L., Hires, S.A., and Looger, L.L. (2012b). Imaging neuronal activity with genetically encoded calcium indicators. Cold Spring Harb Protoc 2012, 647-656.

Tian, L., Hires, S.A., Mao, T., Huber, D., Chiappe, M.E., Chalasani, S.H., Petreanu, L., Akerboom, J., McKinney, S.A., Schreiter, E.R.*, et al.* (2009). Imaging neural activity in worms, flies and mice with improved GCaMP calcium indicators. Nat Methods 6, 875-881.

Tippett, W.J., and Sergio, L.E. (2006). Visuomotor integration is impaired in early stage Alzheimer's disease. Brain Res 1102, 92-102.

Toni, N., Buchs, P.A., Nikonenko, I., Bron, C.R., and Muller, D. (1999). LTP promotes formation of multiple spine synapses between a single axon terminal and a dendrite. Nature 402, 421-425.

Trachtenberg, J.T., Chen, B.E., Knott, G.W., Feng, G., Sanes, J.R., Welker, E., and Svoboda, K. (2002). Long-term in vivo imaging of experience-dependent synaptic plasticity in adult cortex. Nature 420, 788-794.

Tremblay, M.E., Lowery, R.L., and Majewska, A.K. (2010). Microglial interactions with synapses are modulated by visual experience. PLoS Biol 8, e1000527.

Truong, A.P., Aubele, D.L., Probst, G.D., Neitzel, M.L., Semko, C.M., Bowers, S., Dressen, D., Hom, R.K., Konradi, A.W., Sham, H.L*., et al.* (2009). Design, synthesis, and structure-activity relationship of novel orally efficacious pyrazole/sulfonamide based dihydroquinoline gamma-secretase inhibitors. Bioorg Med Chem Lett 19, 4920-4923.

Tsai, J., Grutzendler, J., Duff, K., and Gan, W.B. (2004). Fibrillar amyloid deposition leads to local synaptic abnormalities and breakage of neuronal branches. Nat Neurosci 7, 1181-1183.

Um, J.W., Kaufman, A.C., Kostylev, M., Heiss, J.K., Stagi, M., Takahashi, H., Kerrisk, M.E., Vortmeyer, A., Wisniewski, T., Koleske, A.J*., et al.* (2013). Metabotropic glutamate receptor 5 is a coreceptor for Alzheimer abeta oligomer bound to cellular prion protein. Neuron 79, 887-902.

Um, J.W., Nygaard, H.B., Heiss, J.K., Kostylev, M.A., Stagi, M., Vortmeyer, A., Wisniewski, T., Gunther, E.C., and Strittmatter, S.M. (2012). Alzheimer amyloid-beta oligomer bound to postsynaptic prion protein activates Fyn to impair neurons. Nat Neurosci 15, 1227-1235.

Velasques, B., Machado, S., Paes, F., Cunha, M., Sanfim, A., Budde, H., Cagy, M., Anghinah, R., Basile, L.F., Piedade, R., and Ribeiro, P. (2011). Sensorimotor integration and psychopathology: motor control abnormalities related to psychiatric disorders. World J Biol Psychiatry 12, 560-573.

Verret, L., Mann, E.O., Hang, G.B., Barth, A.M., Cobos, I., Ho, K., Devidze, N., Masliah, E., Kreitzer, A.C., Mody, I*., et al.* (2012). Inhibitory interneuron deficit links altered network activity and cognitive dysfunction in Alzheimer model. Cell 149, 708-721.

Vinters, H.V. (1992). Cerebral amyloid angiopathy and Alzheimer's disease: two entities or one? J Neurol Sci 112, 1-3.

Vogelstein, J.T., Packer, A.M., Machado, T.A., Sippy, T., Babadi, B., Yuste, R., and Paninski, L. (2010). Fast nonnegative deconvolution for spike train inference from population calcium imaging. J Neurophysiol 104, 3691-3704.

Wacongne, C., Changeux, J.P., and Dehaene, S. (2012). A neuronal model of predictive coding accounting for the mismatch negativity. J Neurosci 32, 3665-3678.

Wakabayashi, T., and De Strooper, B. (2008). Presenilins: members of the gamma-secretase quartets, but part-time soloists too. Physiology (Bethesda) 23, 194-204.

Wall, N.R., De La Parra, M., Sorokin, J.M., Taniguchi, H., Huang, Z.J., and Callaway, E.M. (2016). Brain-Wide Maps of Synaptic Input to Cortical Interneurons. J Neurosci 36, 4000-4009.

Walsh, D.M., Klyubin, I., Fadeeva, J.V., Cullen, W.K., Anwyl, R., Wolfe, M.S., Rowan, M.J., and Selkoe, D.J. (2002). Naturally secreted oligomers of amyloid beta protein potently inhibit hippocampal long-term potentiation in vivo. Nature 416, 535-539.

Wang, H.Y., Lee, D.H., D'Andrea, M.R., Peterson, P.A., Shank, R.P., and Reitz, A.B. (2000). beta-Amyloid(1-42) binds to alpha7 nicotinic acetylcholine receptor with high affinity. Implications for Alzheimer's disease pathology. J Biol Chem 275, 5626-5632.

Wassle, H. (2004). Parallel processing in the mammalian retina. Nat Rev Neurosci 5, 747-757.

Wilquet, V., and De Strooper, B. (2004). Amyloid-beta precursor protein processing in neurodegeneration. Curr Opin Neurobiol 14, 582-588.

Winkler, E., Hobson, S., Fukumori, A., Dumpelfeld, B., Luebbers, T., Baumann, K., Haass, C., Hopf, C., and Steiner, H. (2009). Purification, pharmacological modulation, and biochemical characterization of interactors of endogenous human gamma-secretase. Biochemistry 48, 1183-1197.

Xu, T., Yu, X., Perlik, A.J., Tobin, W.F., Zweig, J.A., Tennant, K., Jones, T., and Zuo, Y. (2009). Rapid formation and selective stabilization of synapses for enduring motor memories. Nature 462, 915-919.

Yan, P., Bero, A.W., Cirrito, J.R., Xiao, Q., Hu, X., Wang, Y., Gonzales, E., Holtzman, D.M., and Lee, J.M. (2009). Characterizing the appearance and growth of amyloid plaques in APP/PS1 mice. J Neurosci 29, 10706-10714.

Yan, Y., and Wang, C. (2006). Abeta42 is more rigid than Abeta40 at the C terminus: implications for Abeta aggregation and toxicity. J Mol Biol 364, 853-862.

Yang, G., Pan, F., and Gan, W.B. (2009). Stably maintained dendritic spines are associated with lifelong memories. Nature 462, 920-924.

Yang, G., Pan, F., Parkhurst, C.N., Grutzendler, J., and Gan, W.B. (2010). Thinned-skull cranial window technique for long-term imaging of the cortex in live mice. Nat Protoc 5, 201-208.

Yuste, R. (2011). Dendritic spines and distributed circuits. Neuron 71, 772-781.

Yuste, R., and Bonhoeffer, T. (2001). Morphological changes in dendritic spines associated with long-term synaptic plasticity. Annu Rev Neurosci 24, 1071-1089.

Yuste, R., and Bonhoeffer, T. (2004). Genesis of dendritic spines: insights from ultrastructural and imaging studies. Nat Rev Neurosci 5, 24-34.

Zariwala, H.A., Borghuis, B.G., Hoogland, T.M., Madisen, L., Tian, L., De Zeeuw, C.I., Zeng, H., Looger, L.L., Svoboda, K., and Chen, T.W. (2012). A Cre-dependent GCaMP3 reporter mouse for neuronal imaging in vivo. J Neurosci 32, 3131-3141.

Zhan, L., Zhou, J., Wang, Y., Jin, Y., Jahanshad, N., Prasad, G., Nir, T.M., Leonardo, C.D., Ye, J., Thompson, P.M., and For The Alzheimer's Disease Neuroimaging, I. (2015). Comparison of nine tractography algorithms for detecting abnormal structural brain networks in Alzheimer's disease. Front Aging Neurosci 7, 48.

Zhang, Y., Kim, I.J., Sanes, J.R., and Meister, M. (2012). The most numerous ganglion cell type of the mouse retina is a selective feature detector. Proc Natl Acad Sci U S A 109, E2391-2398.

Eidesstattliche Versicherung (Affidavit)

Hiermit versichere ich an Eides statt, dass ich die vorliegende Dissertation „Structural and functional alterations of cortical neurons in Alzheimer's disease transgenic mice assessed by two-photon *in vivo* imaging" selbstständig angefertigt habe, mich ausser der angegebenen keiner weiteren Hilfsmittel bedient und alle Erkenntnisse, die aus dem Schrifttum ganz oder annähernd übernommen sind, als solche kenntlich gemacht und nach ihrer Herkunft unter Bezeichnung der Fundstelle einzeln nachgewiesen habe.

I hereby confirm that the dissertation „Structural and functional alterations of cortical neurons in Alzheimer's disease transgenic mice assessed by two-photon *in vivo* imaging" is the result of my own work and that I have only used sources or materials listed and specified in the dissertation.

München, den 12.11.2016

Munich, 12th of November 2016

_____

Sabine Liebscher

List of publications

Liebscher, S., Keller, G.B., Goltstein, P.M., Bonhoeffer, T., and Hubener, M. (2016). Selective Persistence of Sensorimotor Mismatch Signals in Visual Cortex of Behaving Alzheimer's Disease Mice. ***Current Biology*** 26, 956-964.

Liebscher, S., Page, R.M., Kafer, K., Winkler, E., Quinn, K., Goldbach, E., Brigham, E.F., Quincy, D., Basi, G.S., Schenk, D.B., H. Steiner, T. Bonhoeffer, C. Haass, M. Meyer-Luehmann and M. Hübener. (2014). Chronic gamma-secretase inhibition reduces amyloid plaque-associated instability of pre- and postsynaptic structures. ***Molecular Psychiatry*** 19, 937-946.

McCarter, J.F., Liebscher, S., Bachhuber, T., Abou-Ajram, C., Hubener, M., Hyman, B.T., Haass, C., and Meyer-Luehmann, M. (2013). Clustering of plaques contributes to plaque growth in a mouse model of Alzheimer's disease. ***Acta Neuropathologica*** 126, 179-188.

Liebscher, S., and Meyer-Luehmann, M. (2012). A Peephole into the Brain: Neuropathological Features of Alzheimer's Disease Revealed by in vivo Two-Photon Imaging. ***Frontiers in Psychiatry*** 3, 26.

Capell, A., Liebscher, S., Fellerer, K., Brouwers, N., Willem, M., Lammich, S., Gijselinck, I., Bittner, T., Carlson, A.M., Sasse, F., *et al.* (2011). Rescue of progranulin deficiency associated with frontotemporal lobar degeneration by alkalizing reagents and inhibition of vacuolar ATPase. ***The Journal of Neuroscience*** 31, 1885-1894.

Rebholz, H., Nishi, A., Liebscher, S., Nairn, A.C., Flajolet, M., and Greengard, P. (2009). CK2 negatively regulates Galphas signaling. ***Proceedings of the National Academy of Sciences of the United States of America*** 106, 14096-14101.

Gunther, L., Liebscher, S., Jahkel, M., and Oehler, J. (2008). Effects of chronic citalopram treatment on 5-HT1A and 5-HT2A receptors in group- and isolation-housed mice. ***European Journal of Pharmacology*** 593, 49-61.

Declaration of author contributions

Paper 1:

"Chronic gamma-secretase inhibition reduces amyloid plaque-associated instability of pre- and postsynaptic structures". S. Liebscher, R.M. Page, K. Käfer, E. Winkler, K. Quinn, E. Goldbach, E.F. Brigham, D. Quincy, G.S. Basi, D.B. Schenk, H. Steiner, T. Bonhoeffer, C. Haass, M. Meyer-Luehmann and M. Hübener.

SL performed and analysed all in vivo imaging experiments; RMP, HS and EW conducted the in vitro characterization of the GSI ELN594 in a cell free assay and performed Western blot and ELISA analysis of ELN594 treated mice; KK assisted in the image analysis of presynapses; EG, EFB, DQ, GSB and DBS as employees of ELAN pharmaceuticals developed and characterized the selective GSI ELN594; TB, CH, MM-L and MH conceived and supervised the study; SL and MH wrote the manuscript with help of all authors.

Paper 2:

"Selective persistence of sensorimotor mismatch signals in visual cortex of behaving Alzheimer's disease mice". S. Liebscher, G.B. Keller, P.M. Goltstein, T. Bonhoeffer and M. Hübener

SL performed and analysed all experiments; GBK built the two-photon microscope and designed and programmed the visual flow feedback paradigm, PMG provided analysis software for visually driven responses, TB and MH supervised the project, SL and MH wrote the paper with help of all authors.

Munich, 15st of November 2016

_____ _____

Sabine Liebscher Prof. Dr. Mark Hübener (1st supervisor)